Cascade Laser Infrared Spectroscopy

Andrea Teuber
Institute of Analytical and Bioanalytical Chemistry, Ulm University, Ulm, Germany

Boris Mizaikoff
Institute of Analytical and Bioanalytical Chemistry, Ulm University, Ulm, Germany; Hahn-Schickard Institute for Microanalysis Systems, Ulm, Germany

Mid-infrared spectroscopy (MIR) has been applied for decades in a wide range of applications, since it is a nondestructive and versatile analytical technique allowing for the analysis of chemically and biologically relevant compounds with high sensitivity and selectivity. Laser spectroscopy provides the most advanced technological approach in IR spectroscopy with several benefits compared to conventional infrared light sources. This article highlights the fundamentals of the latest generation of IR lasers, i.e. so-called cascade lasers. Among their advantages are their high output power, the narrow linewidth, operation in continuous or tailorable pulse mode, reliability during long-term usage, on-chip dimensions, and tunability. Quantum Cascade and Interband Cascade Lasers (QCLs, ICLs) are nowadays available across almost the entire infrared range extending into the terahertz (THz) regime and may either be tuned over several hundreds of wavenumbers or designed to emit a specific wavelength. The most important classes of cascade lasers to date – ICLs and QCLs – will be discussed in their theoretical and technical fundamentals and working principles. Complementarily, selected applications will be highlighted illustrating the utility of these most advanced IR laser light sources available for modern infrared spectroscopy and sensing.

1 INTRODUCTION

MIR is known as a well-established nondestructive technique for highly sensitive and selective determination and identification of chemical compounds.(1) One of the more important advantages of this technique, in comparison, e.g., with far and near-infrared spectroscopies, is the possibility to study the fingerprint region, whereby each vibration can be specifically assigned and it is unique for every molecule. MIR region is in a wavenumber range between 4000 and 400 cm^{-1}, corresponding to 2.5 and 25 μm.(2) Fourier transform infrared (FTIR) spectroscopy is used for routine applications among standard laboratory techniques.(1) This technique is based on the black body radiation, conventionally provided via silicon carbide (SiC), and the light beam is modulated via the Michelson interferometer using the Fourier transformation, allowing extensive qualitative analysis over a wide spectral bandwidth. However, the energy density per wavelength is limited.(3,4) Other light sources in the infrared region are lasers. Lasers can be divided into gas, chemical, dye, metal-vapor, solid-state, and semiconductor lasers.(5) For instance, diode lasers can operate at NIR and visible range and have been used since the 1980s. However, they exhibit a low tuneability (less than 2 cm^{-1}) with an operating temperature in the range of the cryogenic temperature.(3,6) In comparison, modern cascade-based lasers, such as interband and QCLs, exhibit several advantages, such as the possibility to be tuned and to operate in the MIR range at room temperature. It is worth mentioning that lead salt diode and QCLs have an emission range between 3 and 25 μm, while ICLs between 2 μm and 10.(2)

The aim of this article is to introduce the reader to the working principles of ICL and QCL. A short general explanation about laser spectroscopy and the benefits of the cascade lasers will be presented (Section 2), as well as a brief description of some of the most common applications of ICLs and QCLs will be provided (Sections 3 and 4).

Encyclopedia of Analytical Chemistry, Online © 2006–2021 John Wiley & Sons, Ltd.

This article was published in the *Encyclopedia of Analytical Chemistry* in 2021 by John Wiley & Sons, Ltd.
DOI: 10.1002/9780470027318.a9751

2 LASER SPECTROSCOPY

Laser is the abbreviation for light amplification by stimulated emission of radiation.[7] Lasers produce or amplify a narrow, low-divergence light beam with a well-defined wavelength within the optical region of the electromagnetic spectrum, encompassing the near-infrared spectroscopy (NIR), MIR, and far-infrared spectroscopy (FIR) ranges. Lasers have been invented not for a specific reason, or to solve directly some practical problems; however, their potential in IR spectroscopy has been discovered very fast.[5] Lasers in general consist in an amplifying or gain medium, which can be solid, liquid, or gaseous, which is used to increase the power of a light wave during the propagation. To perform the beam amplification, a mirror system is assembled around the gain medium, to form the so-called optical cavity or optical resonator, which allows multiple reflections of the light and the production of stationary waves (or modes) with unique resonance frequencies. The stimulated emission consists of the first excitation, by an incident photon, of an electron from the lower to the upper level, whereby two photons are released. Since spontaneous emission reduces the electron amount in the upper level, a population inversion is necessary, whereby more electrons populate higher energy levels of the atoms than lower energy levels. In a three-level laser, the electrons are excited at the upper part, fall then to the middle one, where the radiation occurs and, finally, relax back to the ground state. In this system, the spatial structure does not change in the optical cavity since the light propagates in the cavity itself. This stationary wave has a Gaussian shape in the plane perpendicular to the axis of the propagation, so the resulting beam must be a Gaussian beam, which can have either longitudinal or transverse modes. The longitudinal mode is a stationary wave, which is reinforced by constructive interferences after the reflectance in the optical cavity, with the consequent suppression of other wavelengths. The nodes are located axially along the length of the cavity, while, in contrast, the transverse mode has nodes perpendicular to the long axis of the cavity. Transverse modes are classified into three different types: when there is no electric field in the direction of propagation, transverse electric mode (TE) is operating; while if there is no magnetic field, the transverse magnetic modes (TM) takes place and the transverse-electro mode (TEm) exhibits neither the electric nor the magnetic field in the propagation direction. Transverse modes determine the pattern of intensity distribution over the entire beamwidth. Single transverse modes are favorable since they provide a single output peak.[7,8]

The lasing threshold is defined as the lowest excitation level at which the beam output is not dominated by the spontaneous emission, but by the stimulated emission. Above the lasing threshold, the laser starts to 'lase', i.e. the laser is emitted,[7,8] as shown in Figure 7(a).

The characteristic monochromaticity of the light depends on several factors, such as (i) the electronic transition, which is responsible for the light emission, (ii) the nature of the transitions, which dominates the bandwidth, and (iii) the intrinsic properties of the resonance cavity. For instance, due to Heisenberg's uncertainty principle, long pulses have a narrow bandwidth and high spectral resolution but a low time resolution, while short pulses exhibit broad bandwidth with low spectral resolution and a high time resolution. Coherence length can be divided into temporal and special coherence. Temporal coherence, also called longitudinal coherence, is related with the spectrum bandwidth of the laser beam which has a narrow output linewidth. Spatial coherence defines a fixed-phase relationship transverse to the direction of the beam propagation.[7]

The abovementioned condition of an inverted population acts itself as a beam amplifier, since, as a light beam propagating through the optical amplifier, the number of photons stimulated will be greater than the absorbed photons, thus amplification of the beam will be produced, i.e. a net increase in the number of photons emitted will take place. To obtain the laser oscillation, the medium must have a certain length concerning the propagated wavelength with an inlet and outlet surface. The reflecting mirrors at the end of the cavity can have different or same reflection values, whereby they induce an optical phase shift. It is worth mentioning that, in the beam amplification process, while the electrons travel between the mirrors, the gain in the amplification medium must overcome the different losses in the optical cavity. When electrons are introduced into the system, the pumping rate is proportional to the inversion density as long as the system stays below the oscillation threshold. The systems then start to oscillate and the amplified photon flux into the cavity increases, whereupon the saturation density increases, and the gain is reduced as long as the cavity losses are equal to the gain in the medium. Once the threshold current is reached, the photon density increases linearly with optical pumping.[7,8] The threshold condition is obtained when the optical field can reproduce itself after one round through the cavity,[11] as shown in Figure 7(a). The output flux of the emitted light depends on the output mirror, so the lower the value of the transmittance of the mirror, the lower the threshold current required. If, for instance, the transmittance is zero, no light can penetrate through the mirror. If the modes start oscillating inside the optical cavity, the maximum laser modes are given by the gain bandwidth and the spacing between modes. In a homogeneous broadening, the lineshape is monolithic and the shape exhibits a Lorentzian

Encyclopedia of Analytical Chemistry, Online © 2006–2021 John Wiley & Sons, Ltd.
This article is © 2021 John Wiley & Sons, Ltd.
This article was published in the *Encyclopedia of Analytical Chemistry* in 2021 by John Wiley & Sons, Ltd.
DOI: 10.1002/9780470027318.a9751

function, leading to a single-mode laser operation. In a nonhomogeneous gain spectrum, the whole system is divided into several subsystems with a set of modes, so all modes are individually amplified, and the laser is multimode, as shown in Figure 7(b). To control the laser pulse time, three different mechanisms can be used. In the damped oscillation, an additional mirror is implemented, whereby photons are accumulated from a fully reflective cavity after the photon energy. Another approach is the Q-switching, whereby the dumping of the laser cavity is achieved by modulating the intercavity losses. Q-switching is obtained, if the quality factor (Q-factor) of the cavity is modulated, by introducing temporarily large losses (the mirrors are temporarily not available) and reducing the reflectivity of the exit mirror. In a first stage, a population inversion occurs, but in the first cycle it is very large, so that laser emission cannot take place, and the energy is then stored inside the optical cavity. As the laser radiation accumulates, the losses are drastically reduced. Once the accumulated energy level reaches the saturation level of the gain medium, the Q-switch devices rapidly switch to a high-Q-factor, whereby the stored energy in the occupied states in the cavity is then released and the optical amplification occurs. The third possible mechanism is the mode-locking, as shown in Figure 7(c), which is a dynamic response in inhomogeneous laser media and allows the generation of pulses in the range of pico and femtoseconds of duration. In this mechanism, the oscillation inside the cavity is not blocked, but the storage of photons in the optical cavity is avoided, contrary to the Q-switching mechanism. Thus, light propagation is carried out by releasing photon packets in a steady-state equilibrium, i.e. the gain curve remains constant over a time interval. Therefore, the laser has a train of pulses with the same intensity. The wider spectrum of the laser gain, the higher the number of supported modes and, therefore, the shorter the pulse. By now introducing a fast response electro-optic shutter in the optical cavity, light transmission is only possible for a short time and the overall wave train propagating inside the cavity is that from the electro-optic shutter.(7,8)

2.1 Principles of Cascade Lasers

Almost one-quarter century ago and approximately 35 years after the first mention of how such lasers should operate in 1960,(12) two different types of cascade lasers have been almost simultaneously presented and developed. In 1994, the QCL was mentioned first in an article by Faist et al.(13), and Yang(14) published one year later the first study introducing the ICL.

Before the development of cascade lasers, conventional diode lasers have been used. In these devices, electrons and holes are injected from the opposite side of a *p*–*n* heterojunction, whereby ideally all of the multiple quantum wells are equally populated.(15) In general, the electrons and holes are injected into the active region of a semiconductor and when they combine, they emit photons with wavelength depending on the bandgap of the semiconductor.(6) In quantum wells, electrons can move freely in this plane, which is perpendicular to the growth direction z. In a one-dimension quantum well, potential barriers and wells are defined depending on the distance to the center.(8)

Diode lasers have a short semiconductor cavity, are sensitive to temperature changes and injection current, and they have broad linewidth with poor tuneability.(16) Lead salt diode lasers, which are the only diode lasers available in the MIR range, have also a limited power of several milliwatts in continuous-wave operation.(17) The quantum wells are positioned as neighbors and are separated by barrier layers, as shown in Figure 1(a). A disadvantage is that if the electrons and holes fail to populate uniformly in the opposite direction of the quantum wells, the gain degrades in the injected current density.(22) The optical gain saturation is achieved, if the population between levels provides an amplification, when both absorption and stimulated emission are dominant.(8) The total threshold current is a product of the threshold current density per quantum wells and the number of quantum wells, while the parasitic voltage drop consists of the total threshold current multiplied by the series resistance area product. However, the voltage drop produced is more significant than the 'useful' voltage, since the currents are often higher and the photon energy is smaller than at shorter wavelengths. One of the advantages of these devices is their versatility in fabrication, as the wavelength of the emitted beam can be controlled by the semiconductive material from which they are made. However, although they can cover a huge range of wavelengths, the narrow bandgaps of these semiconductive materials are not effective in the MIR range as they have a weak bonding between their constituent atoms. It is therefore impossible to reach the MIR range with this class of arsenides and phosphides-based material systems.(19,20,23) The diode laser is working primarily in visible and NIR regions, and those which operate in MIR, as the lead salt diode lasers, have several inconvenient (further are in Section 2.1.3) such as a critical operating temperature, which is why they have to work at cryogenic temperatures, a limited output power, limited tuneability, thermal conductivity, and mechanical stability.(24) Another inconvenience of the diode lasers is the nonradiative loss mechanism due, e.g., to the Auger recombination, the inadequate electrical confinement, poor efficiency in the use of the bias voltage, a nonuniform distribution of the injected carriers, and the increased free-carrier absorption loss.(19) Auger recombination is

This article was published in the *Encyclopedia of Analytical Chemistry* in 2021 by John Wiley & Sons, Ltd.
DOI: 10.1002/9780470027318.a9751

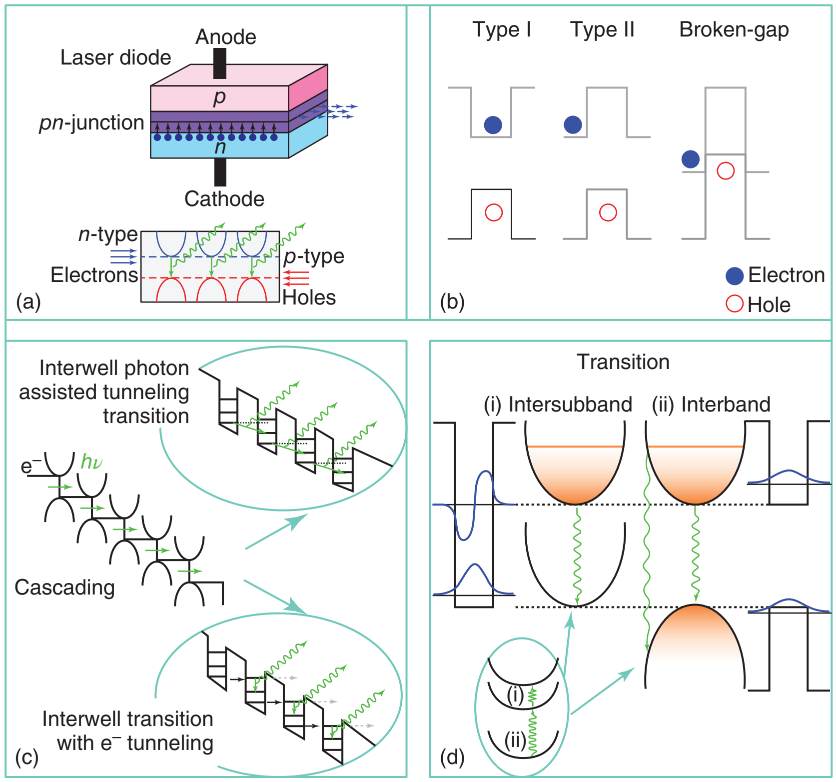

Figure 1 (a) Schematic of diode laser with *p–n* heterojunction. (Adapted from Vurgaftman et al.[18]) (b) Type I, Type II, and Type II broken bandgap quantum well heterostructures. (Adapted from Yang.[19]) (c) Intersubband photon emission in a cascading structure by *interwell* and *intrawell* optical transition. (Adapted from Yang.[14,20]) (d) Schematic of intersubband transitions; the transition takes place between states of the same band and exhibits the same dispersion curve. Schematic of interband transitions; the transition between different states generates a change in the curvature of the dispersion curve. (Adapted from Faist.[21])

resulting from electron–electron interaction, whereby electrons can recombine with another electron or hole and the resulting energy gain is transferred in form of kinetic energy.[8] To achieve the emission of beams with wavelengths in the MIR range, cascade lasers have been developed. Here, the multiple quantum wells are connected in series and the obtained cascading structure mitigates the inefficiency of diode lasers. In a cascading structure, the same current flows through every state, and each injected carrier (electrons and holes) travels through all the stages. The energy staircase is formed under forwarding bias, and undergoing these staircases, one electron emits several photons. A high quantum efficiency (larger than one) is achieved, as the electrons are cascading through these cascades, connected in series. The required recycling of the carriers from the valence to the conductions band, in each stage, does not generate significant additional voltage or current. The electrons are therefore recycled from period to period down the structure. The carrier concentration required for the threshold current is lower than in the conventional diode lasers, which leads to a decrease in the optical and Auger losses, as well as in a lower threshold current density. The parasitic voltage drop is smaller due to the electrical resistance and the 'useful' voltage increases. Parasitic voltage can be reduced across the series resistance with the application of a higher voltage. Furthermore, as in MIR and FIR region, the photon energy is low, the ohmic loss in these devices is negligible. MIR optical losses are reduced due to a lower free hole absorption, which occurs in every stage of a heavily doped tunnel injection.[19,20,22,23,25–27] Originally, the idea of cascading structures was used earlier with tunnel junction in 1982.[28] The cascading is also producing some advantages as the size of the region in which the gain occurs will be increased, the population density which is required for each active region period will be decreased. Therefore, the threshold current density will be reduced and the slope can be increased, as a single electron can emit several photons.[25]

While the electrons are traveling through the cascade structure (Figure 1(c)), intersubband photon emissions are obtained. There are two possible mechanisms of the intersubband photon emission, either the *intrawell* or the

This article was published in the *Encyclopedia of Analytical Chemistry* in 2021 by John Wiley & Sons, Ltd.
DOI: 10.1002/9780470027318.a9751

interwell optical transition. *Intrawell* optical transitions take place from the lowest energy state of a quantum well to the second-lowest energy state of the neighbor quantum well, whereby during this transition a photon is released. In *interwell* transitions, the transition takes place from the lowest energy state to the neighbor quantum well in the highest state, whereby the electrons are relaxing into the lowest state and emit photons. In *intrawell* optical, the transitions are much larger, but the population inversion is difficult to achieve, as the nonradiative relation between the two states in the same well is faster. However, the threshold current is lower compared to the *interwell* transitions. Since the electron transport in the quantum wells is based on the intraband tunneling, two distinct physical requirements must be fulfilled for (i) the realization of an efficient population inversion, (ii) good confinement of the electrons at the upper energy level, and (iii) a fast electron tunneling rate at the lower level. To obtain an adequate population inversion for the lasing action, a high injected current is needed, whereby a considerable amount of heat is generated. It is demonstrated that the nonradiative relaxation of optical photons is three times faster than the optical phonon relaxation, so the nonradiative decay has to be suppressed to achieve the intersubband lasing.[14] Phonons are vibrational waves, which are involving the atoms in the lattice, too. Optical phonons are characterized by the opposite motion of two types of atoms and have therefore a high frequency.[8] The interband transitions are taking place between electrons and holes. Both are separated by true bandgaps and the transitions occur when the exhibited states of the electrons or holes have an opposite dispersion curve, as shown in Figure 1(d). The radiation process is mostly like recombination process. On the other hand, intersubband transitions take place between electrons or holes confined states, whereby here there is a difference between the confined states of the electronic states. This electronic state will go to zero when the well width will be increased. As the electronic states are belonging to the same state, they have the same plane dispersion, and the states are not separated by energy gaps, as shown in Figure 1(d). Any elastic or inelastic transitions allow scattering from higher to lower states. The lifetime of the electrons is determined by nonradiative processes and therefore limits the upper state lifetime to a very short time. The gain and absorptions lines are mostly broadened by scattering and exhibit essentially symmetric lines centered on the transition energy.[21] In other words, intersubband is a transition between the same band, but electrons are moving from one to another subband, in interband transition, the electron from the valence band is excited to the conduction band and intrasubband are promoted from different states within the same subband.[8] The idea to use such intersubband transitions for optical gain are originally from Kasarinov and Suris in the early 1970s, as shown in Figure 3(a). An optical response is obtained by applying a strong elastic field to the superlattice, whereby the ground state of the well will be going up just below the second excited state of the quantum well downstream.[29]

Depending on the alignment of the energy bands where the cascading takes place, the semiconductor interfaces can be classified into three different heterostructures: Type I heterostructures which consist of a straddling gap, type II-staggered gap, and type II-broken gaps (also known as Type III).[31] Heterojunctions are obtained, when one semiconductor is grown on top of another.[8] Type-II heterostructures are characterized by the fact that valence and conduction band offsets have opposite signs, and the electron and hole transfer take place easily. The main difference between type II-staggered and type II-broken gap is that, in the first one bandgaps overlap, while in the second one the bandgaps do not overlap and the carrier transfer is more significant, as shown in Figure 1(b). In Type-I heterostructures electrons and holes are separated in space, so their recombination is only possible when they tunnel through the hetero barrier.[32] However, the Type-I alignment has in the same material the minimum in the conduction band and the maximum in the valence band. Their transition energy can be written as a sum of the energy gap of the well material and the confinement energies of electrons and holes. As a result, the transition energy is limited toward lower values by the gap of the quantum well material. The gain spectrum is broadened by the electron and hole distribution within the bands.[21] That is, in Type-II structures, the interfaces of two semiconductors align so that only the valence or conduction band of one semiconductor fits to the bandgap of the other band. Therefore there is in the same spatial region, a quantum well in one band and an energy barrier in the other band, whereby in Type-I the quantum wells for carriers are in the same band.[33] Type-II heterostructures laser devices have the advantages that they can operate in short and mid-infrared wavelengths, and, by doping the heterostructure, it is possible to transform between both structures (Type-I and Type-II) and modify the behaviors of the wave functions associated with the charge carriers.[34] Doping is obtained, when chemical impurities are introduced at low level to the semiconductor, whereby either they can be donors, the so-called *n*-type semiconductors, an additional electron is inserted, or they can be acceptors, the so-called *p*-type semiconductors, whereby a hole is inserted.[8] The Auger recombination processes in Type-II semiconductor heterostructures are different from the bulk processes. In the heterostructures, the Auger recombination rate is a power function

This article was published in the *Encyclopedia of Analytical Chemistry* in 2021 by John Wiley & Sons, Ltd.
DOI: 10.1002/9780470027318.a9751

of temperature. There are two possible mechanisms that either the electron tunnels through the heterobarrier and recombines with an electron in the quantum well of a hole tunnels through the heterobarrier and recombines with an electron in the quantum well.[32]

2.1.1 *Interband Cascade Laser*

2.1.1.1 Working Principle of Interband Cascade Lasers IC lasers are assembled from the near lattice structure InAs/GaSb/AlSb III–V material, generating a semimetal-like heterostructure.[26] This structure is a specific feature of Type-II broken-gap heterostructures, quantum wells, and superlattices. Even though IC lasers can be made up of both heterojunction types (I and II), the broken-gap alignment makes the interband more efficient, which is needed for recycling the injected electrons in the cascade.[14,20,26,35] In contrast to conventional diodes and QC laser, ICLs are generating holes and electrons at the interface of the bandgap.[18]

By applying an electric field, the semimetallic overlap between the conduction subband of the InAs electron quantum well (acceptor) and valence subband of adjacent Ga(In)Sb hole quantum well (donor) can be tuned.[23] InAs layers are the active regions and are separated by *n*-type multilayers of InAs/Al(In)Sb, which are the injection regions of electrons. Coupled GaSb/AlSb operates as the hole injector and is separated by AlSb barriers on both sides. Therefore, the active core of the IC lasers consists of the active quantum wells, which can be either Type-I or Type-II band alignments, the hole, and the electron injectors, as shown in Figure 2(a).[22] One of the advantages of these semimetal heterostructures is that the quantum confinement needed to overcome the energy gap is small, as the conduction band minimum of the InAs bulk is approximately 0.2 eV at room temperature, which is below the valence band maximum of GaSb,[23] building

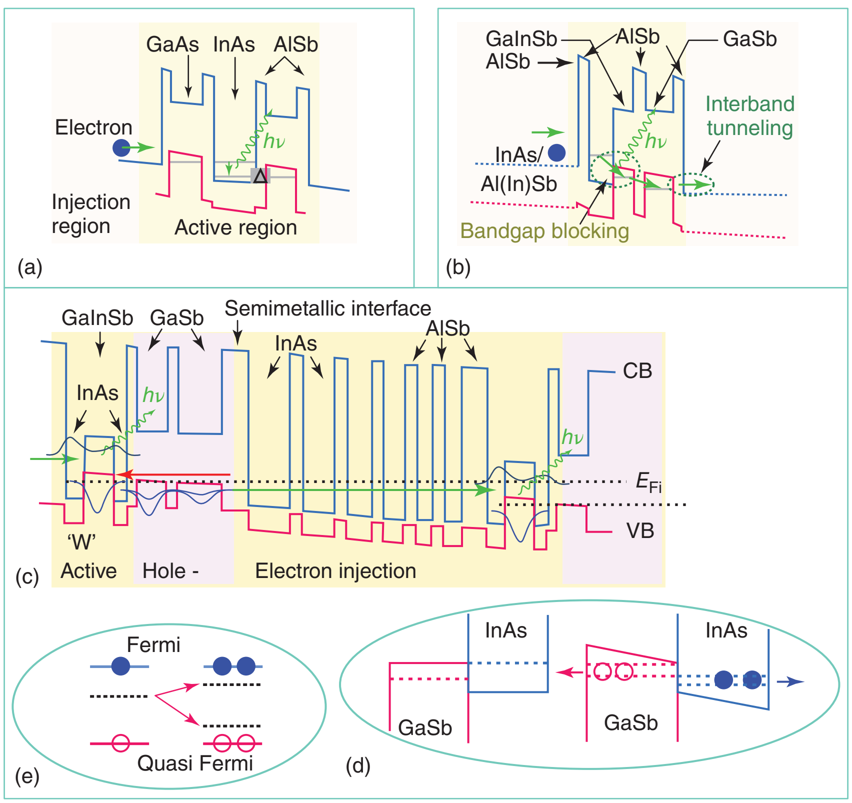

Figure 2 (a) Schematic of energy diagram of active quantum wells, with tunneling window Δ and the photon emission is taking place between two states in the conduction band. (Adapted from Yang[14]; Yang and Xu.[35]) (b) Further development of the active region, whereby the Type III quantum well is used, whereby the photon emission is taking place from the conduction to the valence band with followed interband tunneling. (Adapted from Yang.[20]) (c) One period of the band diagram of an IC laser, which can be repeated several times. Black and blue lines define the probability densities of electrons and holes, respectively. (Adapted from Meyer et al.[22]; Vurgaftman et al.[23]) (d) Type II quantum wells in absence of an applied electric field (right) and with an applied electric field and an overlap-induced electron and hole populations (left). (Adapted from Vurgaftman et al.[26]) (e) Electronic system in thermal equilibrium (right) and far from a thermodynamic equilibrium (left). (Adapted from Rosencher and Vinter.[8])

Encyclopedia of Analytical Chemistry, Online © 2006–2021 John Wiley & Sons, Ltd.

This article was published in the *Encyclopedia of Analytical Chemistry* in 2021 by John Wiley & Sons, Ltd.
DOI: 10.1002/9780470027318.a9751

up Ga(In)Sb Type-II quantum wells. The basic unit of a quantum well laser has therefore at least two coupled quantum, with valence and conduction band structure, which have a strong interband coupling between them.[36] By applying an external electrical field, the lowest conduction subband (InAs LUMO) can be lowered concerning the highest valence subband (GaSb HOMO), whereby a semimetallic interface is created, separating the hole injector from the electron injector. Electrons populate the InAs quantum well and holes migrate to the Ga(In)Sb quantum well, creating a quasi-thermal equilibrium,[23] as shown in Figure 2(e). As both carriers flow away from the interface, to maintain the quasi-thermal equilibrium population, electrons and holes must be replaced by the application of a voltage.[22] The resulting voltage-dependent overlap is typically an operating voltage of 100 meV.[23]

The carrier density through the active core is a field-dependent overlap between the states in the hole injector and active hole quantum wells, as shown in Figure 2(d). As a quasi-Fermi level is reached on both sides of the semimetallic interface (i.e. between the conduction subband of InAs electron quantum well and valence subband of adjacent Ga(In)Sb hole quantum well), the carrier transport via direct, phonon-assisted, or other tunneling mechanisms can be achieved reasonably fast. As there is a relatively long carrier lifetime in the active quantum wells, it is necessary to ensure that the quasi-Fermi level must be discontinuous across the active region of each stage: for this purpose, the applied bias in an ideal design should separate the quasi-Fermi levels in successive stages, equal to the single-stage voltage drop.[22,26] Fermi energy is the energy of the last occupied state and the Fermi level is the chemical potential of the particles in structure and describes the amount of energy, which is needed to remove the particle into the vacuum. The Fermi level in a semiconductor is depending either it is located in forbidden or allowed energy bands. Quasi-Fermi levels are build up at thermodynamic equilibrium when the bands are populated by, e.g., electrically injected carriers, whereby the electron and hole population are described by their own Fermi levels,[8] as shown in Figure 2(e). Therefore, the separation of the quasi-Fermi level should simultaneously produce an optical gain, which compensates for the phonon loss in the cavity.[18] To obtain a good separation, a sufficient optical gain must be produced, which can compensate the photon loss in the cavity, as well as the internal generation of a quasi-equilibrium carrier density, which is consistent with the voltage drop according to extrinsic doping. The sufficient optical gain is a property of the active quantum well, whereby the design and the doping of the electron and holes quantum wells of the semimetallic interface are responsible for the generation of the quasi-equilibrium carrier density.[23,26] The carrier densities are exceeded by doping density. N-doping can be shifted toward the active region to maximize the electron transfer.[18] N-doping leads to a large reduction and p-doping to a minor reduction of optical gain.[37] If the thickness of the electron injector in the quantum well, e.g., exceeds the optimal thickness, there will be an excess of carriers and an unnecessary free-carrier absorption would be induced. Moreover, if the injector quantum well would be too thin, the threshold voltage would exceed, which is needed to induce the ideal quasi-Fermi level separation. In this case, only a small amount of the carriers would contribute to the optical gain, since there would be more injectors than active quantum wells on both sides of the semimetallic interface.[22,23,26]

The carriers can be created either internally at the semimetallic interface or introduced by extrinsic doping. Therefore, the electron and hole injectors must be designed to (i) maximize the fraction of the injected carriers that populate the active states and (ii) maintain a sufficient carrier transport through the complete stage in the single quasi-Fermi level.[22] The energy subbands in the two-hole injector should lie substantially below the upper active hole subband, while the states of the thicker electron injector should stay in the vicinity of the semimetallic interface and energetically lower than the active electron quantum well state. Most of the electron population is located in the injector states, whereas nearly all of the holes reside in the active quantum well. If there is no extrinsic doping introduced to supplement the carriers generated at the semimetallic interface, the active hole density will be higher than the active electron density at the lasing threshold.[22,23] If the Auger process is not dominating the carrier lifetime, the large hole/electron density ratio will tend to reduce the gain per unit of the current density and increase the internal loss unless the cross-section for free hole absorption is negligible.[26] The Auger lifetime is the inverse square of the carrier density.[38] Therefore, the InAs well is designed to have the ground electron state positioned within the bandgap of the GaInSb.[26]

To promote the inverted tunneling, the valence band edge of GaSb must be higher than the conductions band edge of InAs, to favor a strong optical coupling between both layers. Hence, a tunneling 'window' (Δ) in the injection AlSb layer is obtained,[36] allowing the resonant interband tunneling between the ground state of InAs layer to the hole energy in GaSb, as shown in Figure 2(b). Meanwhile, the lifetime of the lowest energy state in InAs is reduced. A similar effect of the energy state of InAs is obtained, by lifting the InAs layer into the forbidden gap of GaSb, which can be achieved by varying the well width and changing, therefore, the barrier height. There are different possible ways to collect electrons in the upper

Encyclopedia of Analytical Chemistry, Online © 2006–2021 John Wiley & Sons, Ltd.

This article was published in the *Encyclopedia of Analytical Chemistry* in 2021 by John Wiley & Sons, Ltd.
DOI: 10.1002/9780470027318.a9751

energy state: by applying a forward bias, for instance, electrons can be injected into the first well of an emitter region, e.g. n^+-InGaAs, whereby electrons will fall in the upper energy state of InAs. Another possible way is via the resonant tunneling into the upper state of InAs. On the right side of InAs, there is the so-called forbidden gap, where the electrons are blocked from directly tunneling out into the collector region. The blocking layer is made up of GaInSb, AlSb, and GaSb layers, which are responsible for suppressing the current leakage from the upper energy state to the next stage injector. Therefore, the only way for electrons to reach the collector region is by a relaxation via the radiative transition to the lower energy state of InAs. Accordingly, electrons move out of this well by tunneling into the next junction region that is the interband transition to the valence state of GaInSb, which is above the conduction band edge of InAs, then moving to the valence band of GaSb, and finally reaching the collector, which is the conduction band of the injection region in the next cascading stage. Here, electrons can be promoted again to the upper state for an additional photon emission, which is an electron transport recycling process. This Type-II band alignment between InAs and GaSb is important for the interband tunneling from one to another stage and is employed as a semimetal source to inject electrons and holes.[14,20,22,26,35] Figure 2(c) shows one period of the mechanism taking place in the ICL, as described above.

2.1.1.2 Design of an Interband Cascade Laser By manipulating the thickness of the InAs and GaInSb quantum well layer, the energy separation of the conduction and valence bands can be changed from a few meV up to 700 meV.[23] As mentioned above, two GaSb quantum wells in the hole injector state are used to suppress the electron tunneling leakage from the electron injector. However, it is not helpful to add more quantum wells in the hole injector state, as the two-holes quantum wells, aligned at the threshold field of the upper subband, are strongly coupled to themselves. Consequently, as an empirical rule, the thickness of the GaSb quantum well should be chosen to place the two subbands approximately 80–100 meV[23] below the maximum in the active hole quantum well. Here, it is ensured that there is a very low occupation in the hole injector states in quasi-equilibrium. The thickness of the AlSb barriers, which separate the active and hole injector quantum wells, are typically between 10 and 12 Å,[23] to assure an unencumbered hole transport. Using thicker barriers, the ICL performance is gradually degraded. The thickness of the electron injector layer should be that thick, to produce the required threshold carrier density; this is obtained with a thickness between 40 and 50 Å[23] in the first electron injector quantum well. The electric field in the active core is then ≈70–90 kV cm^{-1} at the lasing threshold. To ensure the coupling of adjacent quantum wells, the thickness of each subsequent well is reduced. This characteristic is also known as chirping, a process, whereby the laser pulse is shaped in frequency, e.g. the bandwidth can be narrowed for large laser pulse amplitudes.[39] The lower energy subbands closer to the semimetallic interface are more heavily doped than the higher energy subbands adjacent to the active region of the next stage. This configuration reduces the density of the states at lower energy, but there is still a sufficient electron transport from the semimetallic interface to the active electron quantum wells. AlSb barriers in the electron injector state are between 10 and 14 Å[23] thin. However, there are two berries in each state, which must be between 250 and 30 Å[23] thick. These two barriers either separate the electrons and hole injectors at the semimetallic interface (to minimize the parasitic interband absorption across the interface) or separate the electron injector from the first active electron quantum well (isolating the active electron subband from the injector states and preventing significant hybridization while there are still sufficient electrons to tunnel).[22,23,26] As the InAs/AlSb superlattice has a low thermal conductivity, thick layers can cause accumulation of heat and therefore limiting the output power.[40]

The wavelength can be controlled by adjusting the thickness of the quantum wells, which allows a wide range of spectral coverage between 3 and 12 μm. One possible drawback is the reduced wave function overlap between the two interband transition states in Type-II quantum wells, leading to a smaller gain compared to Type-I quantum well lasers. In the Type-I lasers, the electrons and holes wave functions are localized in the same layer. Due to the broken-gap alignment, and the small electron effective mass of InAs, the penetration of the electron wave functions into the GaInSb layer, is sufficient to get the laser working. To promote the overlap of the wave function, a so-called 'W' shape in the Type-II quantum wells can be employed.[14,20,22,35] Effective masses are resulting from the interaction of electrons with the periodic potential of the crystal.[8] The 'W' active region consists of one GaInSb hole well and on both sides the two InAs electron wells. The typical composition of the GaInSb alloy is $Ga_{1-x}In_xSb$ with,[23] which is the maximum value that can be adjusted to maintain a homogeneous layer growth. The 'W' configuration in the active quantum wells enhances the electron–hole wave function overlap in comparison to the InAs/GaInSb quantum well with a single Type-II interface (see Figure 2(c)).[22,23,26]

The waveguide design of ICL is needed to minimize the active region material and the waveguide's internal loss, whereby the electron injector thickness decreases and the thickness of the hole injector increases. InAs/AlSb

Encyclopedia of Analytical Chemistry, Online © 2006–2021 John Wiley & Sons, Ltd.

This article was published in the *Encyclopedia of Analytical Chemistry* in 2021 by John Wiley & Sons, Ltd.
DOI: 10.1002/9780470027318.a9751

has a lower refractive index compared to the GaSb/AlSb layer of the hole injector region. Ten stages are needed for a good waveguide that the light is guided through the structure unless one high-index structure is incorporated. The cladding (InAs/AlSb) must be thick enough to prevent mode interaction to upper or lower GaSb substrate.(26) The electrical mode is here operating in a TE mode.(23) The lasing mode for a five-stage ICL structure is shown in Figure 6(j), as well as the refractive index profile.

2.1.2 *Quantum Cascade Laser*

2.1.2.1 *Working Principle of Quantum Cascade Lasers*

The unipolar semiconductor QC laser is an intersubband laser, with a high laser power, narrow bandwidth, wide tuneability, and low beam divergence.(43) Single-pulse and narrow bandwidth can be specially obtained in continuous wave (CW) operation, as in pulsed operation, the frequency can be chirped due to thermal heating in the laser structure during the pulses. QCLs are defined as unipolar devices, whereby electrons are the only carriers traveling through the structures,(44) in contrast to diode lasers, where both electrons and holes are used as charge carriers.(17)

QCLs consist out of two regions, the gain and the injection/relaxation region, which are repeated several times, working as the active region. One period of the whole QCL structure is shown in Figure 3(c). Two characteristics must be taken into account when building it: (i) the structure should be electrically stable and (ii) the population inversion must take place. The QC laser was the first configuration, which could fulfill all the requirements for the intersubband lasing.(13,25) The simple superlattice structure, which alternates layers of two bulk semiconductors(38) proposed by Kazarinov and Suris,(29) assumes that the superlattice has, under an applied electric field, the ground state of the upper well energetically above the first excited state of the downstream well, as shown in Figure 3(a). This structure was later modified and consists of several unit cells, with each of them with a complex heterostructure potential of wells and barriers, as shown in Figure 3(b).(25,29) The gain region creates the population inversion between the two levels of the laser transition, which can be designed with different shapes, structures, etc., which will be explained in the next section. The active region consists of a ladder with at least three states, whereby two adjacent active regions are connected directly. Electrons are injected in the third state, from the injector stage aligned to the upper one. The population inversion occurs between states two and three, where the lasing part takes place if the electrons will be injected into the third state. The lifetime of state two is shorter than the scattering time from stage three to stage two and the electron–phonon scattering between state three and two is nonresonant. At each of the steps in the active region, electrons are emitted. However, from state three, electrons can also escape into the continuum. The injection/relaxation region is then followed. Here, the electrons should be raised compared to the band edge and enable the injection by resonant tunneling in the next period. It is assumed that it consists of only one level with a constant amount of population, which is aligned to the upper level of the next period. The injector region can build up a mini band, which blocks electrons to escape to the continuum. It serves also as regions to recycle the electrons and inject them again into the system. By alternating the quantum wells and barriers with a changing duty cycle, an effective ‘graded gap’ is created, which compensates the applied electric field.(6,17,25,30) The typical amount of active-region/injector amount is between 20 and 50 stages for lasers operating between 4 and 8 μm.(6) Doping is necessary to provide the electron charge needed for the transport and to prevent the formation of space charge carriers; therefore, the active region needs to be doped, since electrical neutrality must be present in each period. To minimize the scattering induced by the presence of ionized impurities, they should be as far as possible inserted from the active region. Doping impurities leading to a broadening effect of the laser beam, but by removing the dopants from the active area, there is no direct relationship between the injector doping density and linewidth observes, which is in agreement with the linewidth dominated by the interface roughness effect. The main loss mechanism in the waveguides is the free carrier absorption, so the waveguide losses correspond to the doping of the active region. The lifetimes are not limited by electron–electron scattering and are independent of electron density. The operating and threshold currents increase linearly with doping.(6,25,30) The average doping level for MIR QCL is 10^{16} cm^{-3} and a background impurity of 10^{15} cm^{-3}.(45) It is also an ‘electron reservoir’ to insert electrons into the next period. As there is just a small effective applied electric field, due to the bandgap grading, a cooling of the electron distribution toward the lattice temperature will be promoted. Therefore, the injection/relaxation region (i) prevents the formation of electrical domains, (ii) reduces the applied electrical field by lengthening the period, and (iii) the electrons are blocked for the upper state of the laser transition if it is rightly engineered.(25)

The main advantage of the intersubband laser is the cascading of the active regions. The number of periods appears in the threshold current density and the slope efficiency, while the number of carriers injected into the active regions is not dependent on the amount of the series configuration. Therefore, more periods do not affect the population inversion in every single state but increase the applied voltage. In contrast, in the

This article was published in the *Encyclopedia of Analytical Chemistry* in 2021 by John Wiley & Sons, Ltd.
DOI: 10.1002/9780470027318.a9751

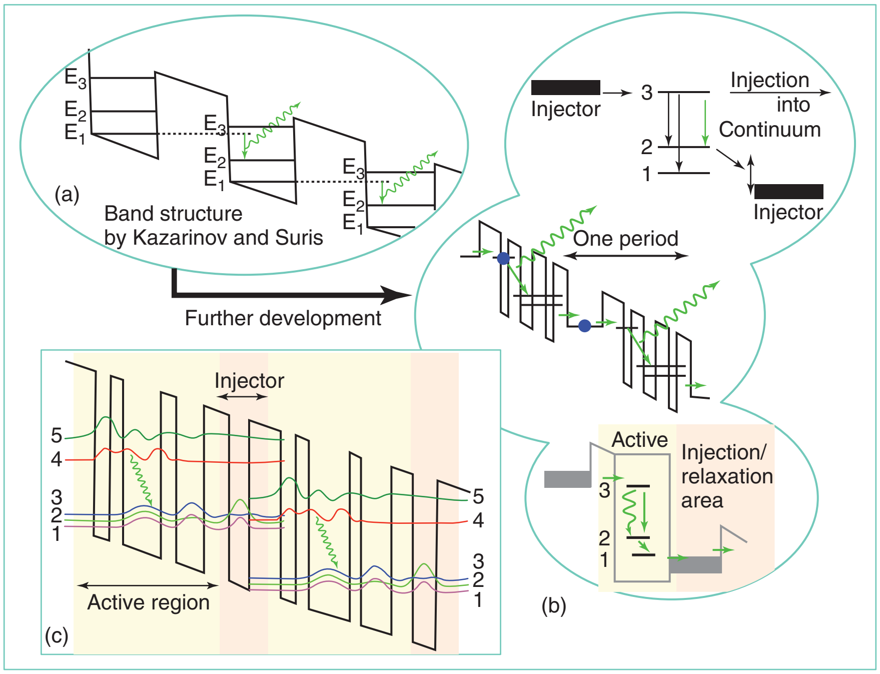

Figure 3 (a) Schematic of the original superlattice structure developed by Kazarinov and Suris. (Adapted from Kazarinov and Suris.[29]) (b) Schematic of the band diagram of the QCL with inversion population between state two and three in a QCL device. (Adapted from Faist.[25]) (c) One period of the whole QCL structure, which can be repeated several times. (Adapted from Bai et al.[30])

conventional diode laser, the increment of the number of quantum wells in the active region increases the threshold current due to the larger active region volume which must reach the transparency.[25] The transparency condition in the general QCL three-level system can be obtained by the population inversion beyond a certain pump photon flux threshold.[8] On the other hand, the slope efficiency is proportional to the number of stages. The threshold current density has a weak dependency on the temperature, as (i) the joint density of the intersubband transition is atomic-like and the temperature dependence of the broadening of the gain curve originates only from the dependence of the in-plane scattering, and (ii) the main intersubband scattering mechanism is the optical phonon scattering as the upper-state lifetime decreases very slowly (factor of two between cryogenic temperature and 400 K). The backfilling is the thermal population of the lower states, which is produced by the carriers thermally excited to the lower state from the injection region, and at the same time, the population must be compensated from this state to achieve transparency and should be minimized. To reach the threshold, a power density of 20–50 kW cm^{-2} is required, otherwise, the device would be self-heated. The active region cannot be assumed to be the same as the submount, especially when operating in continuous mode. The maximum operating temperature in such CWs is (i) the high value of the T_0 and the low intrinsic threshold power, leading to the design of the active region and low-loss waveguides, and (ii) a high thermal conductance power, leading to the thermals engineering of the active region.[25]

The wavelength of the QCL is not dependent on the used semiconductor bandgap, as it is based on the intersubband transition of the semiconductor heterostructure, which consists of several layers of two semiconductor materials and the electron state inside the crystal and wavelength of emitted laser radiation is dependent on the thickness of the layer. These layers and the height of the energy barriers, which are separating the layers, are determining the energy difference in the levels. Applying a bias voltage, electrons tunnel between the levels, whereby the energy difference in the quantum wells corresponds to the lasing energy.[24]

The wall-plug efficiency is defined as the electrical-to-optical power conversion efficiency of a laser system.[46] The optical power of a laser can be improved by increasing the gain medium, however, more electrical power is necessary to drive the laser. As the waveguide losses are dominated by the doping of the active region, the number of periods, the doping level, and the mirror losses have to be taken into account in order to achieve the optimal efficiency. The gain cross-section and the free carrier absorption are proportional to the inverse effective mass.[25] For this reason, the wall-plug efficiency can

Encyclopedia of Analytical Chemistry, Online © 2006–2021 John Wiley & Sons, Ltd.
This article is © 2021 John Wiley & Sons, Ltd.
This article was published in the *Encyclopedia of Analytical Chemistry* in 2021 by John Wiley & Sons, Ltd.
DOI: 10.1002/9780470027318.a9751

be adjusted by optimizing the band structure design and on-device fabrication.[46] It is worth mentioning that high wall-plug efficiencies reduce the waste heat produced within the laser. For instance, ICLs employing with a 'W'-configuration have a wall-plug efficiency better than 20% when they operate at temperatures around 90 K.[47] QLCs, e.g., have wall-plug efficiencies of more than 20% operating at room temperature, whereby it is higher in pulse mode than in CW mode.[48]

2.1.2.2 Design of the 'Intersubband Toolbox' As the main goal is to achieve low threshold and high-efficiency lasers, several parameters should be taken into account: (i) there will be a large ratio of the upper to the lower state in the active region, (ii) a low waveguide loss, (iii) a narrow transition linewidth and (iv) long upper lifetime. As these requirements are in conflict with each other, the 'intersubband toolbox' is generated to engineer the lifetimes and dipoles and then combined to create the active region architecture via changing the tunneling, the optical phonon scattering, the phase space, the escape time with Bragg reflection and the upper-level confinement, as well as the injection efficiency.[25] The performance of the intersubband laser can be also described by the internal quantum efficiency and the threshold current density, which is depending on the nonradiative intersubband transition rate.[11]

Intersubband scattering occurs when the electrons in the excited subband recombine to the lower subband via different paths, such as (i) spontaneous emission, which has low radiative efficiency, (ii) inelastic scattering by a phonon, (iii) elastic scattering through impurity or interface defects and (iv) electron–electron scattering, as seen in Figure 4(a). The radiative emission, which is dominant in the interband scattering, is also prevalent in the intersubband scattering, not even in a perfectly pure material. If two subbands are spaced with the energy bigger than the optical phonon energy, the optical phonon emission is the dominant scattering. The other scattering mechanisms compete with them but can be avoided by a correct design of the structure. For short-wavelength lasers, elastic scattering by interface roughness is important. Elastic scattering between subbands occurs, due to collision with ionized impurity or through scattering at an interface step. The interface roughness is responsible for the broadening of the intersubband transitions in the MIR range, whereas the linewidth broadening is mainly due to the intrasubband scattering. The difference between intersubband and intrasubband is that the intersubband scattering rate is used to compute the population dynamics of the states. The electrons move from one subband to another. In intrasubband scattering, the electrons remain in the subband, but they change their wavevector. The linewidth of an intersubband transition in a GaAs quantum well as a function of temperature shows that at higher temperatures, the binding energy increases, as does the electron mobility.[25,49]

The scattering rate increases with the transition energy. Molecular beam epitaxy (MBE) can be used to change the interface roughness and therefore the elastic scattering. If the energy between the subbands is below the optical phonon energy, elastic scattering of interface roughness is forbidden depending on the temperature and the electron density, so the lifetime is controlled by a competition between optical phonons and the other scattering processes. At temperatures higher than 60 K, the dominant mechanism is the optical phonon scattering, while electron–electron scattering or interface scattering are the stronger mechanisms at a lower temperature, depending on the structure and electron density. Acoustic phonon scatterings are relevant for extremely low densities and very pure systems. Both, optical and acoustic phonon scattering, are phonon scattering mechanisms. Phonons are lattice vibrations and disturb the periodicity of the semiconductor crystal by inducing inter-level transitions and allowing energy to let flow the lattice and the electron system. The polar optical phonons scattering is the most efficient phonon scattering in the III–V structures. Acoustic phonon emission lifetime is a function of the quantum well thickness since it increases with the thickness of the quantum well[11,49] (Figure 4(c)). Besides the elastic scattering produced by interface roughness, there are other elastic scatterings, such as (i) the impurity scattering, which is the strongest scattering mechanism, that limits the low-temperature mobility in pure, not alloyed, semiconductors and that is found at relatively large doping levels (ii) the alloy scattering, which is the dominant scattering mechanism, that limits the mobility of high-pure alloyed semiconductors at low temperatures and that weakly increases with temperature, characteristic which is relevant for short-wavelength QCLs, and (iii) electron–electron scattering, whereby two electrons exchange the energy and momentum so that the total energy and momentum are conserved.[11,49,50] Therefore, this process thermalizes a carrier population and does not cool it down. In these circumstances, six different processes can occur, (Figure 4(b)). The processes 1212 and 2121 do not influence the population of the subband and process 2211 or 2221 decreasing the upper-state population. In consequence, the processes 1212 and 2121 tend to balance the temperature of the two subbands and for large transition energies, the upper start population will heat up as the lower one heats up due to the electron energy loss. Processes 2211 or 2221 transfer electrons from the upper to the lower subband, which is important for low transitions energies. Finally, processes 2222 and 1111 exhibit scattering within a single subband, which helps to establish a thermal equilibrium in the single subband. This

Encyclopedia of Analytical Chemistry, Online © 2006–2021 John Wiley & Sons, Ltd.
This article is © 2021 John Wiley & Sons, Ltd.
This article was published in the *Encyclopedia of Analytical Chemistry* in 2021 by John Wiley & Sons, Ltd.
DOI: 10.1002/9780470027318.a9751

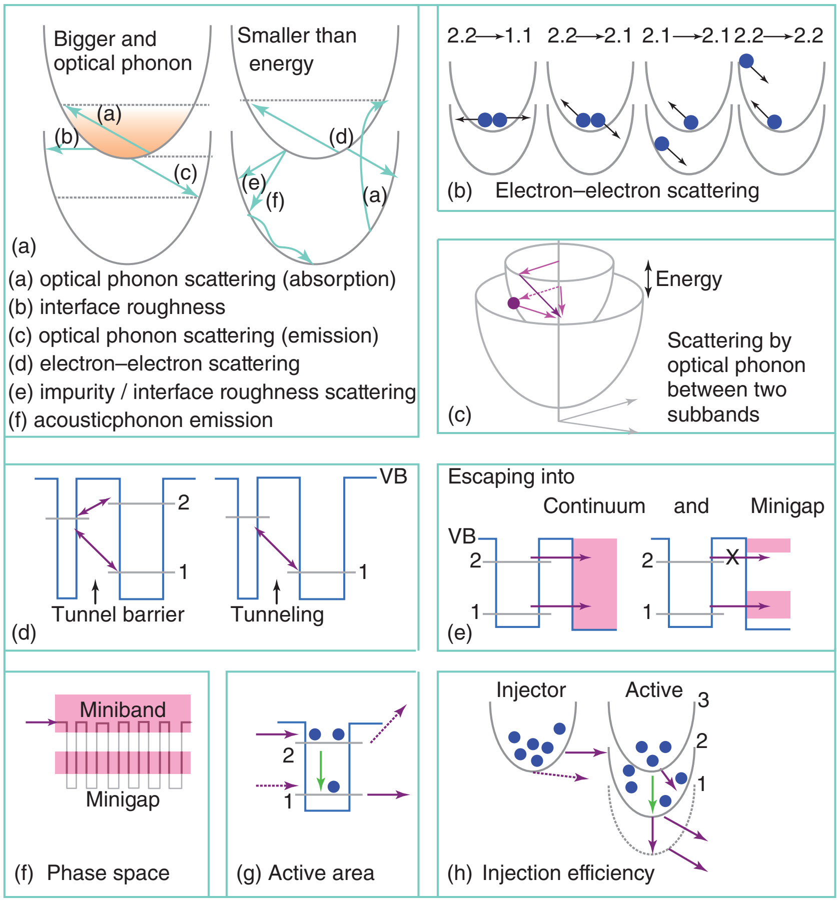

Figure 4 (a) Scattering mechanism if the band gap is smaller or bigger than the optical phonon energy. (b) Mechanism of electron–electron scattering. (c) Optical phonon scattering between two subbands, (d) The lifetime of the upper state is dependent on the thickness of the coupling barrier, and the tunneling occurs between state two and state one. (e) Electrons cannot tunnel into minigaps and minigaps face the excited state of the laser transition, (f) The population inversion is build up at the edges of the minigap. The phase space is larger for scattering out from the upper-state to the lower miniband than the phase space in the same state. (g) Schematic of the active area. (h) The injection efficiency and the relevant levels take place in the lasing part. (Adapted from Faist.[25,49])

process determines whether the electron distribution is a set of phonon or thermal replicas in lasers with large transitions energies (200 meV), where electrons must emit a large number of optical phonons before reaching the bottom of the band.[11,49]

The first parameter in the 'intersubband toolbox' is tunneling, as shown in Figure 4(d). If the first and the last state of the laser transmission are placed in different quantum wells and they are coupled by tunnel barriers, the scattering rate decreases with the increase of the tunnel barrier thickness and independently to the scattering mechanism. The states, behaving like destructive quantum interferences, are induced by impurities far away from the wells. Other scattering mechanisms, such as optical phonons or interface defects scattering have, in comparison, a shorter range and take place in another phase in the state. As mentioned above, the intersubband scattering rate and the oscillator strength are dependent on the barrier thickness, so the gain cross-section, which is proportional to the ratio of the oscillator strength and the intersubband scattering rate, does not change with the barrier thickness. Optical phonon scattering decreases with the barrier width, which is faster than the oscillator strength that increases with the barrier thickness. This is, by applying a fixed transition energy, the transition increases diagonally through the tunnel barrier width between the quantum wells. Another advantage of tunneling is that it is not dependent on the exact nature of the scattering mechanism.[25]

Another parameter, which can be adjusted, is the optical phonons. The lifetimes of MIR-QCLs are limited by optical phonon transmission. With an optimized

This article was published in the *Encyclopedia of Analytical Chemistry* in 2021 by John Wiley & Sons, Ltd.
DOI: 10.1002/9780470027318.a9751

design, other parasitic processes, e.g. tunnel escape, can be neglected. The reduction of the intersubband lifetime by approaching the transition energy to the optical phonon emission energy leads to a separation of the two states. The intersubband transition between state two and three is less common, as the emission of photons with energy larger than the optical phonon is nonresonant process.[25] Price[51] showed the easiest way to improve optical phonon scattering in polar III–IV semiconductors, as (i) the phonon scattering is dominated by the interaction between the electron and piezoelectric potential in the local lattice deformation and (ii) the optical phonons can be assumed as monoenergetic as they have just a small dispersion. By increasing the intersubband lifetime the population inversion is promoted, and the electrons exhibit large kinetic energy after their first optical phonon emission. The increment of the temperature leads to a decrease in a lifetime when the transition energies are larger than the optical phonon energy. Therefore, the scattering time is almost not dependent on temperature. Optical phonon is turned off when the subband spacing is below the phonon energy and the electrons in the excited state have enough energy to compensate this difference.[11,49,51]

Intersubband lifetime is also adjusted by the control of the phase space, as shown in Figure 4(f). A superlattice is periodically formed by alternating wells and barriers and creates minibands and minigaps, which can be adjusted by modifying the well and barrier thickness. Population inversion and optical gain are achieved at the edges of the minigap when the carriers are injected in the lower state of the upper miniband. The lifetime of a superlattice with a minigap has almost the same time as the intersubband lifetime if both have the same size. Therefore, the scattering rate between the different levels of the minigap edges will also decrease with the total number of wells in the superlattice. The lifetime of the lower state must be very low, as electrons from an upper state of the lower miniband can scatter at any point of the lower state out very efficiently. Superlattice active areas have the advantage that the optical transition occurs between the excited states, whereby the oscillator strength is larger than in that of a single quantum well with the same transition energy. With the increment of the number of periods, the upper lifetime increases, whereby the total upper state lifetime between the edges of the minibands decreases along with the three-level system. However, active regions with more than eight periods do not work. The reason is (i) with the increment of the number of periods, the adjacent levels decrease until the states are closer than their intrinsic broadening and therefore the injection efficiency decreases, since the population of the upper miniband spreads over many states and (ii) the electrical injection at the edge of the superlattice cannot be infinite over a coherence length. The advantages of using an intersubband laser with a superlattice active region are, among others, the high output power, the possibility to operate at high temperature and that the phase space does not depend on the exact nature of the scattering mechanism.[25]

The fourth parameter to be modeled is the escape time, see Figure 4(e). Under an applied electric field, the electronic states are resonant in their lifetime, due to the finite probability of tunneling by autoionization. Autoionization translates electrons from the upper state into the continuum, (escape time). This process takes place especially in the upper state lifetimes of stages with large confinement energy, and occurs directly or through coupling with the intermediate state in the lower epilayer stack, reducing the total upper state lifetime. To avoid carriers to escape from the quantum wells, confined states in the active region must be transferred into real-bound states by artificially bounding the structures with high barriers. This condition reduces the upper state lifetime below the limit set by optical phonon scattering. Therefore, by using a minigap facing the upper state of the laser transition in the injection/relaxation region the problem can be solved. The attenuation of the wavefunction in this region is proportional to the width of the gap, which should be designed concerning the wavefunction and be centered on the first exciting step of the laser transition. The increment if the thickness of the escape barrier is not sufficient to decrease the escape time, since the escape rate of the lower states would also be automatically reduced. Therefore, to design the gap in the continuum, the Bragg reflection condition with application of a Bragg reflector injector instead of a graded gap injector should be taken into account. Under these conditions, the optical power is increased and the electron escape time is reduced. The increased temperature leads to a reduction of the electron coherence length and electrons can be thermally activated above the minigap, which again increases the electron escape rate.[25,52]

The last parameter, which can be modeled, is the injection efficiency, explained in Figure 4(h). The injection-extraction of the electrons is a nonideal process, since electrons are not effectively injected into the upper state and are not immediately extracted to the lowest state. If a fraction of the current is injected into the upper state and another fraction into the lower state, the nonresonant injection occurs due to elastic or inelastic scattering between the injector state and the lower states of the active region, as shown in Figure 4(g). The designed structure must exhibit a maximum difference in the lower state of the upper miniband and the upper state of the lowers miniband in order to obtain an optimal injection efficiency and lifetime ratio.[25]

Encyclopedia of Analytical Chemistry, Online © 2006–2021 John Wiley & Sons, Ltd.
This article is © 2021 John Wiley & Sons, Ltd.
This article was published in the *Encyclopedia of Analytical Chemistry* in 2021 by John Wiley & Sons, Ltd.
DOI: 10.1002/9780470027318.a9751

2.1.2.3 Designing the Laser Structure via the Intersubband Toolbox By combining the 'intersubband toolbox' the three-quantum-well active region, the two-phonon extraction, and the bound-to-continuum extraction can be obtained. Figure 5(a) shows different mechanisms for the laser transition.

The three-quantum-well active region is used in the first-mentioned QC laser.[13] The diagonal transition allows a good ratio between the upper and lower state lifetime and is combined with the optical phonon resonance. The active area is build-up so that the ground state of the thinner well comes into resonance with the ground state of the thicker well. The tunnel barrier of the energy splitting has to coincide with the optical phonon resonance. For that, a third quantum well is needed upstream as the excited states gain energy faster with thicker quantum wells and the excited states are no longer in resonance. When introducing the third quantum well, two different mechanisms can be produced, since it can be either resonant or anticrossed to the well below. If the transition is diagonal, the lifetime is twice that of the vertical transition, whereas, if the new state is above the third state, the transition has a lifetime equal to that of the vertical. The extension of the wave function into the injection barrier thus improves the injection efficiency,[25] as shown in Figure 5(b) and (c).

A drawback of the three-quantum wells connected via diagonal transition is the long taking time (2 ps; compared to fast scattering between state two and one in the active region), which enables electrons to scatter back into the second state via multiple scattering events between these states. The population inversion is not easy to achieve and degrades the high temperature and high power performance of the devices,[25] as the two-phonon extraction is more favorable to use.

The two-phonon extraction bypasses the complication of diagonal transitions, as the extraction is obtained by separating the states with an optical phonon at each step. By adding new levels, the population of the lower states decreases; in this new condition, the lower wavefunction of the upper state (wavefunction 4 in Figure 5(d)) and the upper wavefunction of the lower state (wavefunction 3 in Figure 5(d)) become the lasing states. As shown in Figure 5(d) the four-quantum wells in the active region have three coupled lower states (and each of the three coupled lower states are separated by phonon energy. A short intersubband electron scattering time is obtained thus via double-phonon.[25,53] Double phonon conformation has the advantage that the QCLs exhibit a lower threshold and higher power. In the active region, the three energy levels in the four-quantum wells are equally separated by the energy of the phonons.[17] There, the extraction of the electrons into the injector region has a better efficiency. The upper lasing state has a longer intersubband electron scattering time with emission and absorption and a vertical lasing transition. The first thin well reduces the overlap of the injector ground state and the lower lasing state with the wavefunctions 1, 2, 3 (Figure 5(d)). The injection efficiency is similar to that of the three-quantum-well design, so that the two-phonon-extraction combines the advantage of the high injection efficiency of the three-quantum-well and the short lifetime of the lower lasing state of the superlattice design.[25] Two phonon-resonance designs have a larger population inversion, as the electrons are efficiently removed from the lower state of the laser transition and the thermal backfilling is reduced.[17]

The bound-to-continuum approach (Figure 5(e)) is another method to achieve high population and low threshold current density even at high temperatures and it is based on the active regions of the superlattices.[25] The bound-to-continuum design is based on a continuum of the states on the low-energy end of the optical transition.[54] The superlattice has a large oscillator strength and a favorable minigap edge lifetime ratio. As the active regions of the QCL operate under a strong applied electric field, the periodicity of the superlattice breaks down as the miniband splits into a set of localized states and loses all its benefits in the extended states. Therefore, the superlattice must be doped homogeneously inside the active region to screen the field. However, this approach introduces additional broadening and losses due to the ionized dopants.[25] To overcome these limitations, Tredicucci et al.[55] proposed to 'chirp' the superlattice and thus compensate the applied electric field. Additionally, below the threshold, electrons relax their excess energy by electron–phonon and electron scattering processes in the active region of the superlattice. If a large current is injected, the electrons are excited with more power than needed for the energy relaxation time, and a set of nonequilibrium electrons with an average energy higher than the thermal reservoir are created. The miniband edges are kept constant in the superlattice by changing both the barrier and well-width in presence of the applied electric field. Throughout the entire period, the active region is extended and consists of chirped superlattices. The lower miniband should be kept tilted, to obtain the maximum width in the center and thus a decrease to both sides close to the injection barriers. The upper state is created in the first minigap by a small well adjacent to the injection barrier. Their wavefunction has its maximum close to the injection area and decreases in the active area. In the first minigap, the upper-state is separated from the higher-lying states of the superlattice. This structure has not to be separated into an active and injection/relaxation region. The large energy separation (60 meV) does not reduce the electron injection into higher energy states

Encyclopedia of Analytical Chemistry, Online © 2006–2021 John Wiley & Sons, Ltd.
This article is © 2021 John Wiley & Sons, Ltd.
This article was published in the *Encyclopedia of Analytical Chemistry* in 2021 by John Wiley & Sons, Ltd.
DOI: 10.1002/9780470027318.a9751

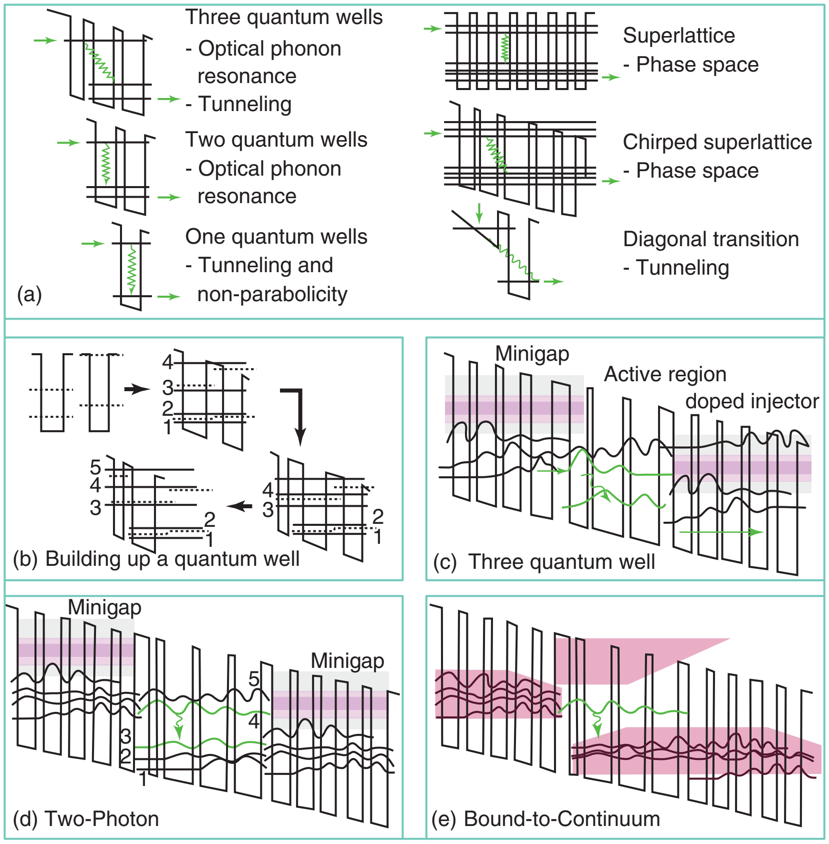

Figure 5 (a) Different possibilities for the laser structure. (b) Building up a quantum well step-by-step. (c) Three-quantum well structure. (d) Two-phonon quantum wells. (e) Bound-to-continuum active region. (Adapted from Faist.[25])

of the superlattice[25,56,57] and the injection efficiency is comparable to the one in the three-quantum well design. The miniband selection rules are a bit relaxed as a result of the localization of the upper-state and the oscillator strength is extended between the upper-state and several lower states. The advantages of the bound-to-continuum approach are, among others, (i) low-temperature dependence in the threshold current, (ii) a working range in long-wavelength regimes, and (iii) high broadband gain. The latter advantage is due to the fact that the single upper state shares several lower states, whereby a gain over a broad wavelength range is obtained.[25]

2.1.2.4 Waveguide Design for Quantum Cascade Lasers

Optical waveguides should be designed to minimize the internal loss and to maximize the gain required to reach transparency.[23] Figure 6(a) shows different configuration of waveguides. Due to the interaction between the electronic system and the optical mode, optical absorption and gain are obtained, as light is propagating through the waveguide. Optical fields are strong enough to introduce new transitions, but weak enough not to change the states themselves, and the interaction of light with matter can introduce a level of perturbation. Considering a one-band model, only the z-component of the electric field is coupled with the intersubband transition.[41] The wave can propagate within a waveguide if the optical confinement is satisfied. If the refractive index of the core, which is sandwiched of two layers above and below, is higher, total internal reflection occurs. If the polarization of the wave is from TE mode nature, the polarization of the electric field is parallel to the layer planes, and the wave is reflected with a phase shift relative to the incident wave. Every reflection at the interface will dephase the wave causing it to interfere with itself destructively, as long as the reflected wave will remain in phase with the other waves, which are produced by the preceding reflections. Optical confinement is at a maximum when the TE and TM modes are in zeroth order.[8] The scattering rate within the waveguides is following Fermi's golden rule, which gives the probability of how the transition rate changes from one initial state to another due to some disturbance. The absorption of the electromagnetic wave is responsible for the decay of the

Encyclopedia of Analytical Chemistry, Online © 2006–2021 John Wiley & Sons, Ltd.
This article is © 2021 John Wiley & Sons, Ltd.
This article was published in the *Encyclopedia of Analytical Chemistry* in 2021 by John Wiley & Sons, Ltd.
DOI: 10.1002/9780470027318.a9751

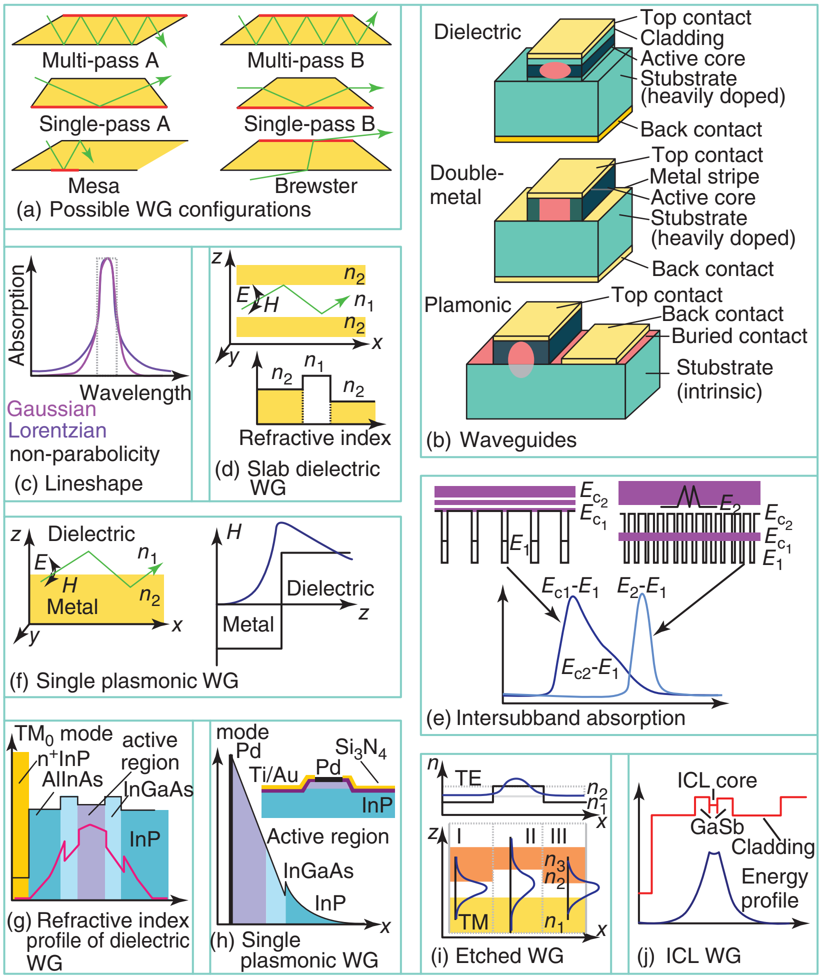

Figure 6 (a) Schematics of waveguide designs. (b) Building up a dielectric, metal, or plasmatic waveguides. (Adapted from Yu and Capasso.[6]) (c) Homogeneous broadening leads to Lorentzian line-shapes. (Adapted from Faist.[41]) (d) Slab dielectric waveguides. (Adapted from Faist.[42]) (e) The sum rule shows, the intersubband transition is getting narrower, when there are more quantum wells. (Adapted from Faist.[41]) (f) Single plasmonic waveguide. (Adapted from Faist.[42]) (g) Refractive index profile of dielectric waveguide. (Adapted from Faist.[42]) (h) Single plasmonic waveguide response. (Adapted from Faist.[42]) (i) Etched waveguide. (Adapted from Faist.[42]) (j) In comparison: an ICL waveguide structure with resulting refractive index profile (red) and the energy profile (blue) of a typical five-stage ICL. (Adapted from Vurgaftman et al.[26])

quantum system. The lines are broadened due to the scattering of electrons with lattice vibrations and collision with the interface roughness. Stimulated absorption can occur at the same rate as absorption if the upper state is populated and the lower state is empty, whereby the optical power is generated instead of absorbed. Using a waveguide, a good signal-to-noise ratio can be achieved, as the absorption strength is in prism-like waveguides enhanced. These waveguides induce a large electric field component in the growth direction. Brewster-angle geometry, see Figure 6(a), is not favorable for materials with a high refractive index, as the internal angle is getting small and a small component of the field in the growth direction. The atomic-like nature of the joint density and the tailorable potentials can be used to create multiquantum wells with engineered levels to provide resonant nonlinearities and the electronic states are coupled by strong dipole matrix elements. If the upper state is located in the continuum, the absorption is distributed along the continuum. In this case, the potentials should be trapped in an artificial box and considered as bound states, as the wavefunctions, which should be treated together, are then getting quite complicated.[41] The sum rule is using the envelope approximation, obtaining the oscillator strength, which is relevant to the optical absorption and only a small amount of superlattice bands are contributing to the sum,[58] see Figure 6(e). The envelope function is used to envelop an oscillating signal

This article was published in the *Encyclopedia of Analytical Chemistry* in 2021 by John Wiley & Sons, Ltd.
DOI: 10.1002/9780470027318.a9751

with smooth curves.[59] In the approach of Kane, the effective mass is obtained from the interaction between the conduction and valence band and it's proportional to the bandgap. Narrowband semiconductor exhibits for this reason much larger intersubband transition strength compared to wide bandgap materials. The analysis of two systems, with almost the same electron density and experimental condition, evidence that the intersubband absorption is emitted further between several transitions within a simple square well in a two or three quantum well system. As the 'downward' transition has a negative sign, and the sum rule has to be constant, the upward transition has an oscillator strength. Electron–electron interaction is expected to add a correction in the transition energy as the electron density is in order of 10^{17}–10^{18} cm^{-3}. As the Hartree potential, which is the electrostatic potential from the electron charge density, is mostly influencing or potentials with dipole charge, the depolarization shift can be seen as a screening of the interaction of one electron by the rest of the others as the absorption will have a higher peak at a higher frequency than in bare transition. This effect is especially strong for high electron densities and low frequencies. The depolarization shift causes a single transition a blueshift. If a large collection of oscillators with different transition energies are interacting via the depolarization field is investigated, the transitions will be getting narrower and blueshifted as the oscillator strength of the transitions of lower energies is transferred to them to the higher transition energy. The broadening arises then either from the nonparabolicity or from the inhomogeneous broadening. The stark tuning of intersubband absorption shifts the levels due to an addition of a static electric field to the potential of the heterostructure.[41] The stark effect is, when the energy levels are increasingly separated, whereby the resonant optical transition connection of these two levels is blueshifted in energy. This effect is getting important when the electron wavefunction cannot go outside the quantum well and the electrons in the ground state can tunnel through the barrier and leading to an electric filed ionization of the quantum well.[8]

For modeling the beam light shape, the lineshape function will be used, whereby for a given design, the material, injection, and oscillator strength will be fixed. The gain is inverse proportional to the linewidth as the lineshape function is normalized to unity. The linewidth can be either broadened homogenous, which is lifetime broadening due to collision and radiative transition, or inhomogeneous, which occurs due to velocity distribution caused by the thermal motion of the atoms. Homogeneous broadening leads to a Lorentzian lineshape, see Figure 6(c). The scattering time is not only given by the lifetime of the upper state. The scattering process takes electrons from one state to another in the same subband, as in quantum-wells the upper and lower states are subbands, whereby the population of both states is not changed, but a loss in the phase is occurring. This process is called dephasing and broadens the lifetime.[41] The homogeneous broadening occurs due to inelastic oscillation and a finite lifetime population of each level within the quantum well. Elastic collision leading to temporal coherence.[8] In quantum wells, the inhomogeneous broadening arises from long-range quantum well interface fluctuations and the nonparabolicity.[41] Nonparabolic band structures can be obtained by using the superlattice approximation, whereby the fundamental optical absorption can be calculated of perfectly periodic systems in bulk materials. This approximation uses the superlattice wave vector $K=0$ and the modified bulk Kane model.[60,61] The heavy-hole mass results from the inclusion of an antibounded band and the effective mass can be calculated using the sum rule.[62] In multiquantum wells, the inhomogeneous broadening arises from fluctuation within the well width and the homogeneous broadening mechanism is the interface roughness.[41] Inhomogeneous broadening, are, e.g., the Doppler Effect, whereby the overall lineshape is an average of individual lineshapes. Inhomogeneous broadening is resulting from fluctuations in the growth parameters of the sample.[8] The limiting cases for the lineshapes are (i) the nonparabolicity leads to a step-like density of the two subbands with different masses, as the high electron densities and narrow bandgap material have a square lineshape at low temperature, (ii) the disorder leads to Gaussian lineshape, as for narrow wells, the heavy mass is leading to disorder and (iii) Lorentzian lineshape is observed in clean systems with a short lifetime. Considering the 1–3 transition in asymmetric quantum wells at low temperatures, the lineshape is a Lorentzian shape and the 2–3 transition is a Gaussian lineshape in the low-density carrier regime. Disorders are achieved by monolayer fluctuations of quantum well interfaces. Linewidths are limited by interface roughness scattering, found Lorentzian lineshape with decreasing the width with increasing the quantum well width, with little or no effect on alloy scattering. The linewidth broadening is increasing with the increasing of the well width.[41]

The light is confined vertically by the epitaxial layers and horizontally by the ridge structures. As the epitaxial growth allows tight control of the layer thickness, which is why the optical confinement is stronger than the vertical one. The one-dimensional dielectric slab model predicts the propagation within the waveguide. The optical gain is only achieved at the cost of large power dissipation in the material, due to the very short upper state lifetime. The power dissipation is in a factor of 10–100 higher compared to IC lasers (current density of 3 kA cm^{-2} at an applied electric field of 100 kV cm^{-1} with a power dissipation of

Encyclopedia of Analytical Chemistry, Online © 2006–2021 John Wiley & Sons, Ltd.

This article was published in the *Encyclopedia of Analytical Chemistry* in 2021 by John Wiley & Sons, Ltd.
DOI: 10.1002/9780470027318.a9751

300 MW cm^{-3}). Therefore, the electrical dissipation has to be kept at a minimum.[42]

Waveguiding can be achieved using metallic, dielectric confinement, or both, see Figure 6(b). Dielectric confinement is loss-free and metals with the light confinement can get in a region smaller than the wavelength. Using different refracting indices, the same semiconductor materials can be used to achieve quantum confinements because of the different bandgaps. A longer wavelength in the MIR range limits the thickness of cladding layers before getting growth problems. The light is confined vertically due to the sequence of the epitaxial layers and horizontal due to the ridge structure, which also confines the current. As the epitaxial growths allow the tighter control of the layer thickness compared to the lateral ridge width, the optical confinement is stronger in a vertical direction. The simple one-dimensional dielectric slab model provides a correct propagation and overlap factor in the waveguide. The easiest dielectric waveguide is a slab of dielectric materials in the core with a refractive index bigger than the two semi-infinite lower index cladding layers around. The thickness of the guiding layer is in the order of the wavelength.[42] If the refractive index is constant across each layer, plane waves will propagate in the z–y plane in each layer, whereby the phase factor in the y-direction is assumed to be common in all layers. There are two polarization directions possible, the transverse electric (TE) or TM polarization of the wave orientated along the y-axis,[41,42] see Figure 6(d).

Symmetric waveguides have a pair of plane waves to propagate constant in the x-direction and depending on the polarization direction of either TE or TM, the boundary conditions are applied at the interface. It enables a change at the interface (see Figure 6(f)) if one material behaves optically as metal, whereby the slope of the local components of the magnetic field changes at the interface and a confined mode decay in both materials. The optical loss is therefore compensated by the gain of the active region. The InGaAs/AlInAs/InP is favorable for dielectric waveguides, as the reference index of InP is $n=3.1$, AlInAs has a refractive index of $n=3.2$ and GaInAs has $n=3.5$. The upper cladding is AlInAs grown by MBE and has a lower refractive index with the active region than the InP substrate. The active region is separated from the heavily doped InP substrate by the heavily doped InP by a low doped AlInAs lower cladding layer,[42] as shown in Figure 6(g).

Interface plasmon mode is important in the TM polarization direction.[42] With plasmonic structures, the emitted wavefront can be engineered, whereby a one-dimensional grating is added to the laser facet. As the grating is integrated into the laser, no additional alignment of mirrors, compared to other resonators, is needed and the plasmonic collimator design can be scaled and designed to fit on lasers with a wide range of emitting light.[63] The electrical contracting is done by surface metallization and an interface plasmon is present in the confined mode. For wavelengths longer than 15 μm, the single plasmons have losses and confinement factors comparable to the dielectric waveguide. In the MIR range, the interface plasmon is lossier than the dielectric mode. In dielectric waveguides, the cladding thickness is linear to the wavelength. The wavelength increases with the needed doping to enable electrical transport and creates therefore a growing loss. Therefore, for lasers operating with wavelength longer than 10 μm, the single plasmon waveguide is preferred. The waveguide loss is decreasing with increasing of wavelength. Single waveguide exhibits a stronger confinement compared to a dielectric waveguide and a reduced total thickness of the grown layer.[42] Using a large refractive index drop within the waveguide prevents the mode penetration in other regions. The doping of the GaInAs layer is important to suppress the coupling between the fundamental mode of the waveguide and the high-loss plasmon mode propagating along with the metal-semiconductor interface. The doping has to be that high that the plasma frequency approaches but does not exceed the waveguide mode,[63] see Figure 6(h).

Free carriers inactive region and in cladding layers, can be controlled using the Drude-like approximation, whereby the motion of the classical free electrons of the effective mass and their belonging damping force are used. Depending on the doping of the GaInAs, the refractive index and absorption are depended on the plasma frequency. For frequencies higher than the plasma frequency, the refractive index is not changed and the free carrier introduces an absorption proportional to the square of the wavelength and electron density. Losses obtained from cladding layers should be small compared to the cavity losses of the QCL and therefore the doping should be in the range of 2×10^{16} cm^{-3} close to the active region, where the overlap is large. Higher doping closer to the contact region can be used, to limit the additional series resistance, and closer to the contact region, the optical field is small. Decreasing the light frequency until it approaches the plasma frequency, the refractive index of the semiconductor is depressed, whereby low-index confining layers can be created. Decreasing the frequency, even more, the semiconductor behaves optically as a metallic layer with a low electron concentration. This effect can create plasmon waveguides for the THz region. Changing the doping and the frequency to obtain a low index region, leading to a push of the mode into the core of the waveguide. If the layers are doped too much, the plasma resonance does not reach the photon energy, whereby the absorption coefficient is increasing. If the refractive index is larger than the active region, the

This article was published in the *Encyclopedia of Analytical Chemistry* in 2021 by John Wiley & Sons, Ltd.
DOI: 10.1002/9780470027318.a9751

antiguiding layer is created. The growing of those thick low-index cladding layers is problematic because of poor electrical and thermal conductivity,[42,64,65] as shown in Figure 6(g).

Ridges are creating lateral waveguides, which are broader than vertical waveguides, as the resolution is defined from the fabrication technique (the ridge is in the order of 1 μm). As the optical power scales with the width, broad ridges are favorable for high power devices. The lateral waveguides from conventional ridge-etched structures are achieved by etching through the active region and the sidewalls coated with Si_3N_4 or SiO_2 leading to trapping the mode completely inside the ridge structure and the electric field is varnished. Using a layer of InP after the ridge etching, providing optical and electrical confinement,[42] as shown in Figure 6(i).

Ridge and buried heterostructured waveguides have, due to their large refractive index step between core and side, more than one transverse mode. The multimode character of the spatial and spectral is characteristic of the lasers. The mode selection that in ridge processes higher optical losses occur from the high-order lateral mode, due to the intensity of the optical field is larger than the lossy metal sidewall, is used in Fabry–Perot and distributed feedback (DFB) lasers. In contrast, in buried heterostructure waveguides, there is a change in the overlap factor between the lateral modes. In comparison, in interband devices, where the lateral mode is achieved by weak lateral confinement, due to a shallow lateral etch of the active region, the difference between the effective index in the center and the side of the active region is small enough and supports the lateral waveguide only in one guided mode. Implementing this process to QCL, the shallow etching of the cladding included weak lateral confinement. The active region in QCL is in comparison to ICL strongly anisotropic, with a higher lateral than vertical direction and the threshold current is therefore higher. As the optical power in pulsed operation is limited by the gain saturation of the medium, the mode cross-sectional area is increased to scale up the power, whereby the laser stripes are widened up. Power up to several hundred watts can be obtained with the drawback of asymmetry in the divergence angle of the beam with a high multimode character of the lateral mode profile. Therefore, it is dangerous to increase the mode size in the growth direction.[42,66]

As the active area of the QCL dissipates a large amount of heat, and therefore the active region is increased is important to take into account when the laser is used in high duty cycle operation. The temperature change is nevertheless demanded, when the tuning of the single-mode DFB lasers, as the refractive index is here tuned with temperature. In steady-state, the active region temperature is related linear to the temperature of the submount. Therefore, the optical waveguide design is a compromise between the achievement of low optical losses with the tightest possible confinement and the decrement of the thermal resistance. The heat is carried out mostly by acoustical phonons, as low doping density is used to prevent efficient heat transport by the electrons. The III–V semiconductors have similar phonon densities of states, but the phonon means the free path is reduced by the alloy scattering. As the thermal conductance is limited by phonon-free mean path, it is anisotropic in the layered active region, as the heat flowing perpendicular to the layers is lower than that compared parallel to the layer. InP has a higher thermal conductance compared to semiconductors, therefore, it is a preferred material for waveguide claddings.[42] InP interstacks provide additional lateral heat transport.[67] Compared to normally buried heterostructure waveguide, such large optical cavity devices have an enhancement of the peak power by a factor of 10, while the single spatial mode in the vertical and transverse direction is kept. The thermal resistance is not only dependent on the waveguide but also on the mounting and soldering process. Using junction-down mounting improves the CW devices' performances. The temperature in the active region is followed by Fourier's heat transport equation and the heat generation outside the active area is neglected due to Joule heating in cladding and contact.[42]

In contrast, the ICL waveguide is build up from the active core, the n-doped optical cladding, followed by the InAs/AlSb short-period superlattice, whereby AlGaAsSb is an alternative for lattice-matched bulk alloy, followed by the lightly n-doped GaSb and various transition superlattices separates the three regions from each other and also from the GaSb substrate/buffer and the n+-InAs(Sb) top contact. The transition superlattices reduce the parasitic voltage drop with is associated with abrupt heterointerfaces between the adjacent regions with the different conduction band offsets.[23]

2.1.3 Difference Between Interband Cascade Lasers, Quantum Cascade Lasers, and Other Light Sources

IC and QC lasers reuse the electrons to generate multiple photons with high quantum efficiencies.[20] The characteristics of ICLs include (i) a population inversion, which occurs naturally through the physical property of the material and its energy gap, (ii) a minimum of current that has to be injected to reach the material transparency, and (iii) the maximum current carried by the device which is limited by either heating or catastrophic damage on the facet. The intersubband, i.e. QCLs, has the properties that (i) the population inversion has to be established

Encyclopedia of Analytical Chemistry, Online © 2006–2021 John Wiley & Sons, Ltd.

This article was published in the *Encyclopedia of Analytical Chemistry* in 2021 by John Wiley & Sons, Ltd.
DOI: 10.1002/9780470027318.a9751

by a suitable design of the active region, (ii) there is no transparency current, and (iii) the maximum current is achieved by the doping of the device and alignment of the band structures. However, the active region is different, depending on the laser. By reducing the active volume of the ICLs, the transparency current can be reduced and the electron–hole pairs can be confined in quantum wells. The transparency current in InGaAs lasers, e.g., is less than 100 A cm^{-2}. In QCLs, the minimum threshold current is obtained over a large active region of 25–50 periods without the need to increase the thickness of the active region or minimize the optical loss from the waveguide and the active region to obtain the highest performance.(25) QCLs have output powers up to 5 W at room temperature, with modest temperature sensitivity, and an efficient heat dissipation. The disadvantage is the high threshold current with fast photon-assisted depopulation of the upper lasing subband and the interface roughness scattering, leading to a bias of at least 10 V due to the 30–50 stages for the sufficient gain.(23)

The most significant difference between these lasers is, that in QCL, the intersubband transition is dominated by fast phonon scattering, and in contrast, in ICL, the photons are generated in optical transitions between the conduction and valence band, with Auger recombination. The threshold current is lower in ICL compared to QCL. The polarized output beams of both lasers are also different, as in QCL it is TM, and in ICL it is TE,(19,20) i.e. ICL operates mainly in TM polarization mode, whereas QCL is suitable with TE polarization mode.(40) ICLs generate higher gain per injected current density, compared to QCLs, even if the differential gains per unit carrier density are the same. QCLs are optimal to operate in multiwatt MIR output powers, while ICLs have a more modest output power.(27)

In comparison with conventional and NIR lasers, with implement of QCLs, the direct access of rational vibrational bands is available, while in NIR laser, the overtones of this band are available with less sensitivity. Lead salt diode lasers must work close to cryogenic conditions, with a multimode source, and are quite bulky, a condition that limits the access for in-field measurement. Optical parametric oscillator lasers, exhibit bulky and expensive frequency generation with implemented optical configurations, so they are also limited to in-field measurements. QCLs are compact devices that operate at room temperature, and have a narrow bandwidth with long operating lifetimes and low output powers as well as are tuneable over several hundred wavelengths.(24) DFB-ICLs provide several hundred milliwatts at room temperature and thermal tuning of about 10–20 cm^{-1} with slow and fast injection current tuning of 2–3 cm^{-1}.(24)

2.2 Resonators

Tuneable single mode operations can be obtained using the DFB or external cavity (EC) configuration.(68) The threshold power density is more fundamental than the threshold current, which depends on the dimensions of the cavity. The cavity could be changed by using a high-reflection coating on the output facet.(27)

The simplest optical cavity, which consists of two facing mirrors, is the Fabry–Perot cavity. This optical cavity is formed when the active region is placed in the center of the MIR waveguide building a long ridge by cleaving the long ridge at a length of 1–3 mm. Fabry–Perot modes appear below the threshold and the contrast increases with the injected current. For the common Fabry–Perot cavity length, the mode spacing is much narrower than the gain width of 100–200 cm^{-1}, so the laser operates above the threshold and the exact location of the single-mode is almost not possible to predict with sufficient accuracy.(10) The tuning is performed through temperature, which is responsible for a change in the refractive index and the band parameters. Fabry–Perot cavities are build up with a vacuum–metal–dielectric–metal–vacuum configuration(8) and have an anti-reflection at the end facets of the laser ridge. The cavity length has to be so long that several longitudinal modes must fit into the cavity.(54)

DFB is another resonator configuration which exhibits a major stability in comparison with the conventional Fabry–Perot cavity. The application of the DFB configuration inside the active regions results in a small periodic modulation of the effective waveguide index.(10) DFB CL has an integrated grating, so the laser is tunable at and above room temperature and the modulation of the absorption is determined by the Bragg reflection (first-order grating).(69) Single modes are obtained by selecting one mode out of the cavity.(68) The Bragg condition consists of in-plane wavevectors with gratings providing several numbers of wavevectors. By increasing the order of gratings, the number of scattering directions increases. First-order gratings allow only backscattering, while the second-order gratings allow frequency selection and surface emission. Bragg reflections create a gap for which propagation is not possible.(10) Bragg waveguides have a grating that acts as a Bragg reflector and has a periodic modulation in the relative permittivity. This condition is satisfied, when the wavevector of the grating is equal to the guided wave. Bragg mirrors are obtained, when the transmittance of one medium approaches that of another in an alternating layer of two media,(8) as shown in Figure 7(d, top). DFB tunings are based on lateral metallic Bragg gratings, incorporated into the laser structure, resulting in a monomode-emitting semiconductor laser with a wide accessible wavelength range between 760 nm and 3 μm. This metallic grating structures do

Encyclopedia of Analytical Chemistry, Online © 2006–2021 John Wiley & Sons, Ltd.
This article is © 2021 John Wiley & Sons, Ltd.
This article was published in the *Encyclopedia of Analytical Chemistry* in 2021 by John Wiley & Sons, Ltd.
DOI: 10.1002/9780470027318.a9751

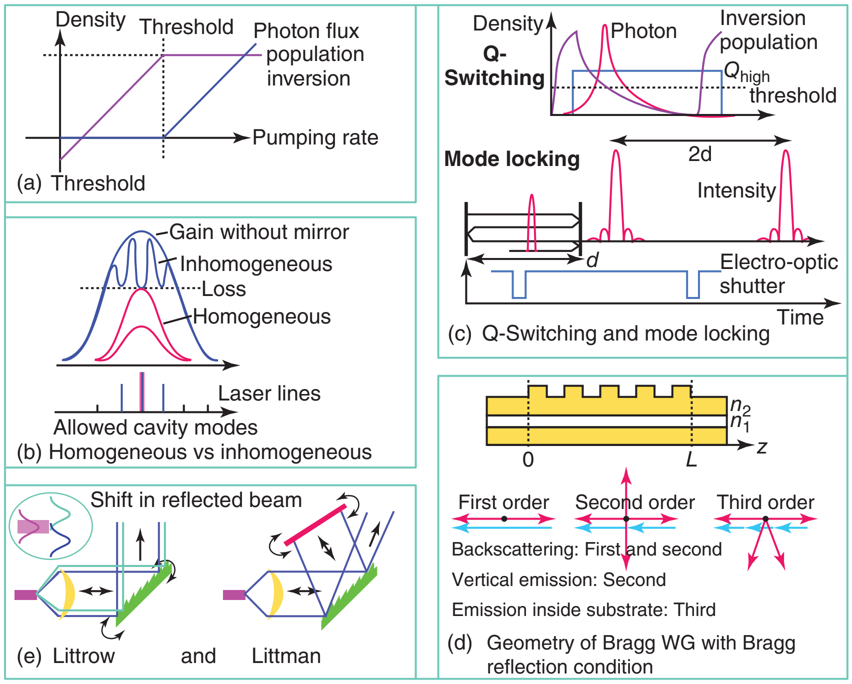

Figure 7 (a) Schematic of the threshold current. (Adapted from Rosencher et al.[9]) (b) Homogeneous and inhomogeneous broadening with the resulting laser linewidth. (Adapted from Rosencher et al.[9]) (c) Q-Switching and mode locking. (Adapted from Rosencher et al.[9]) (d) Schematics of the Bragg waveguide geometry and examples of Bragg reflections. (Adapted from Faist and Faist.[10]) (e) Littrow and Littman configurations. (Adapted from Faist and Faist.[10])

not require any overgrowth steps, making the process 'easier' and reducing the source defects. Since only the evanescent part of the mode interacts with the grating, the spatial overlap is by two orders of magnitude less than that of the overgrown grating incorporated into the waveguide. The additional losses introduced by the gratings lead, however, to a slight penalty in the threshold current and the output efficiency. The nodes of the DFB modes are in phase with the absorption grating, so only small damping of the DFB modes can be obtained,[70] as shown in Figure 7(d, down).

DFB-QCL has the advantage that they are mode hop free during tuning, they can work in pulsed or CW mode, have an higher output power of several hundred milliwatts, and can work under room temperature condition; however, they cannot be tuned over such a long wavelength region, normally of 7 cm^{-1}, so EC-QCL is used for longer tuning, and can be employed in pulsed or CW mode and tuned over 100 cm^{-1}.[24] Mode hop comes from the competition of the different optical modes, which are available in the laser, and distinctive energy gaps will be obtained even if the gains spectrum itself is homogeneous.[54] DFBs have a limited tuning range, so they are designed to work around a particular absorption feature and as the tuning takes place through temperature, the output power of the laser can decrease with increasing temperature.[24] The limiting tuning parameter in DFB-QCL is the amount by which the effective mode index can be tuned by temperature. To tune the laser, a tunable wavelength filter is used outside the laser cavity, with an antireflection coating at the active gain medium, lenses, and gratings.[10] As there is a temperature change during short pulses, a chirp of the output frequency is induced with time and the linewidth grows linear to the pulse length.[10] DFB lasers have been initially used in pulsed mode, as the active layer can be heated up and thus change the wavelength.[71] The tuning range of DFB lasers is, however, limited by the current-induced tuning range, a limitation from several nanometers. One approach to obtain broader tuneability is to use multiple individual DFB lasers at a selected wavelength, which is expensive and is constrained by increasing complexity.[72]

The application of binary superimposed gratings (BSGs) increases the coupling strength in a monolithic solution with high tuning speeds. Conventional DFB gratings select a single wavelength due to the constant period within the grating structure, whereas BSGs have a specially designed grating that combines several grating periods into an aperiodic structure and support the Bragg wavelength simultaneously in a comb-like spectrum. With this configuration, a tuning up to 60 nm can be achieved. The great advantage of the BSG is its

This article was published in the *Encyclopedia of Analytical Chemistry* in 2021 by John Wiley & Sons, Ltd.
DOI: 10.1002/9780470027318.a9751

simplicity and versatility, as the positions of the grating reflection peaks can be easily adjusted. Devices with single BSG emit comb-like structures, combined with a Vernier tuning, and thus a single-mode emission is obtained, whereby two sequences with BSG in different spaces with constituent grating are combined in one IC laser device.[72,73]

Plasmon-enhanced waveguides, which are designed to reduce losses associated with interface plasmon mode and the free-carrier absorption,[74] are used to achieve an optimal coupling with the grating at the surface and a lower loss. The grating is etched by wet chemical etching and in the grating grooves the thickness of the heavily doped plasmon layers is reduced, so the guided mode interacts more with the metal.[69] Therefore, the interaction between the surface plasmon and the propagating mode allows a modification of the refractive index as well as the loss.[10] The cavity length should be close to unity for optimal slope efficiency and threshold current. DFB lasers exhibit less slope efficiency compared to Fabry–Perot lasers due to additional scattering losses within the waveguide.[69]

The optical gain profile of a QCL is typically broad and can be employed in the EC configuration to obtain an even broader wavelength tuning range with narrower linewidth. The antireflection coating is placed on one or both facets of the semiconductor chip end, whereby the diffraction grating, which acts as wavelength filter element, is used to feed the first order backside of the laser. Tuning is accomplished by rotating the grating, and the grating is mounted so that, as the grating is rotated, the frequency shift is fed back into the laser and matches the resonance supported by the change in the cavity length.[10]

Generally, the Littrow cavity, a first-order direct feedback configuration, is used as the first-order diffraction from the grating is directed back into the laser, as shown in Figure 7(e). A zero-order of the output beam is then obtained. The beam splitter is responsible for a decrease in the cavity mode-loss discrimination, due to the grating relative to the facet. The Littman–Metcalf, as shown in Figure 7(e), which is the first-order diffraction, directs the beam to a mirror, whereby the beam is reflected off the grating, diffracted back and the first-order beam from the second pass is fed back to the laser. The output beam resulting from the first pass is zero-order. Due to the shallow angle of the diffracted grating, which is passed two times by the beam, a narrow linewidth can be obtained. However, the output beam power is weaker compared to those of the first-order direct grating feedback configuration. To obtain a single-mode tuning with a continuous mode-hop-free tuning, a piezo-activated cavity mode is used, so in this mode tracking system, the grating is implemented on a moving platform, with an independent control of the grating angle and the chip (EC length). Mode-hop-free tuning is theoretical possible by controlling only the grating angle, so the EC length and temperature modulation should be no longer necessary. Another possible method to tune the Littrow cavity-based laser, obtaining a mode-hop-free laser, is by controlling the tuning with an algorithm.[10]

The benefit of the external cavity is the gain saturation in the active area, whereby the optical parameters can be controlled. By insertion of a dispersive element in the system, the wavelength can be controlled and by changing the reflectivity of the mirror, the mode power can be changed. Longitudinal modes are then obtained.[75] Single-mode emission, for instance, EC-QCL is achieved by changing the angle of the external diffraction grating via frequency-selective feedback.[76] In EC-QCL, the laser light is coupled back into the active laser cavity by reflective and wavelength selective optical elements, as the gratings. The laser facet and the grating compete with the laser cavity, whereby the EC dominates the laser mode if the semiconductor facet is coated with a sufficient transparent anti-reflection coating. They can be tuned in a range of 80–100 cm^{-1} around the center wavelength. The tuning range is determined by the gain curve of the QCL.[71] Tuning can happen on the EC mode near the on-chip Fabry–Perot mode. Mode-hop occurs only in the EC mode but can be suppressed by varying the cavity length with the grating angle. QCLs are more adapted to lase in multiwavelength compared to ICL, as the active regions are arranged in series, which ensures the same injection efficiency in all active wells, independently of the number of wells. Additionally, compared to ICL, the gain is always accompanied by the absorption at higher frequencies and no reabsorption occurs between the active regions of different wavelength. For this reason, the active region can be tuned to a specific transition frequency over a wide range around one frequency. EC-QCL can be tuned over a large wavelength region with narrow linewidth. They are not monolithic devices and therefore bulkier and more fragile than DFB. The wavelength stability depends on the mechanical stability of the device. The gain chip is easier to fabricate than DFB lasers, but they need a finely tuned anti-reflection coating for a reflectivity below 10^{-3}. To solve the inconvenience of the back facet phase in the DFB, this must be fold and a DFB ring laser is produced. The light then either comes out directly from the surface or through the substrate of a second-order grating. The optical-loss component is different in the two modes on either side of the stop-band and the bending losses provide a mode-selection mechanism.[10] By changing the QCL cavity length, the tuning for the gain spectrum can be controlled, making the laser emission frequency more tailorable.[76] Pulsed DFB QCLs lead to so self-heating processes within the active region, which is the key function for spectral tuning.[77]

This article was published in the *Encyclopedia of Analytical Chemistry* in 2021 by John Wiley & Sons, Ltd.
DOI: 10.1002/9780470027318.a9751

The buried grating is the etching of the grating in the InGaAs layer above the active region and afterward a regrown of InP, whereby the highest performance levels with low dissipation and CW operation, especially when it is combined to buried heterostructure waveguides.(10) Littrow and Littman–Metcalf are the most common configurations.(78) In both configurations, the laser resonator is set between the antireflection coated facet of the laser and the diffraction coating, in the case of Littrow, or the diffraction grating plus tuning mirror, in Littman–Metcalf configuration.(79)The Littman configuration exhibits a strong wavelength selection by a double pass through the grating, while the Littrow arrangement maximizes the back-coupling into the active region chip. The tuning of the EC-QCL with Littrow configuration can be obtained via the wavelength-dependent amplitude reflection coefficient of the EC.(10)

2.3 Manufacturing of Interband Cascade Lasers and Quantum Cascade Lasers

QC lasers are made out of epitaxial heterostructures. Spatial coherence of the crystal over well-defined and long-lived electronic states as well as high crystalline qualities of the materials is important to ensure the devices can work under thermal and electrical stress. To obtain such structures with almost no defects, the MBE or the metalorganic chemical vapour deposition (MOCVD) is used. MBE is a thin-film deposition, and it allows the fabrication of films of exceptional crystalline quality in ultra-high vacuum. The MBE operates under low pressure (approx. 10^{-11} mbar). In the deposition chamber, there is the Knudsen cell or simply cell, a thermal source, which carries the source material. The substrate manipulator carries the bare substrate, on which the fabricated layer will be grown. Pyrometers and thermocouples are needed for the heating up. In situ measurements of the grown layers can be obtained by using reflection high-energy electron diffraction (RHEED). Using a shutter, different materials can be introduced. The epitaxial growth is 0.5 μm^{-1} μm h^{-1} and the layer thickness between 3 and 10 μm needs accuracy of about 1 Å for quantum wells and barriers. This accuracy can be obtained with a transition time and temporal accuracy of the mechanical shutters with open time below 100 ms and the gas flux accuracy better than 1%. The other possible method for growing the laser layers is via MOCVD. The epitaxial growth is achieved by using thermal decomposition, on the single crystalline substrate, of precursors and dopants. In the case of QCLs, organometallics from group III and hydrides from group V are flown into the reactor using carrier gases as H_2 or N_2. On the susceptor, there is the substrate positioned, which is heated up by halogen lamps. The layers are grown epitaxial, by decomposition of the hydrides and organometallics on the substrate-free group III and V elements. The remaining gases are pumped out and neutralized. The layer sequence and the composition of each layer can be controlled by the gas fluxes and gas source switching. Using MOCVD, there are fewer options for in situ controlling the growth compared to MBE. The working temperature in MOCVD processes is higher than in MBE, so the QCLS have slightly smaller photon energies and interfaces. The downtime of MBE is faster than that of MOCVD and the fluxes, adjusted via mass flow controllers are not susceptible to source depletion. It is also possible to obtain a selective growth of InP on SiO_2 or Si_3N_4 masked surfaces by the usage of MBE. As the growth of phosphide materials is easier using MOCVD, a combination with MBE growth for the active areas followed by MOCVD for the top InP cladding is often used. The grown layer can be then characterized. In high-resolution X-ray diffraction (HRXRD), the X-ray spectra with broadened peaks are correlated to QCL performance, whereby the collimated beam is incident on the crystal surface, diffracted by the parallel atomic planes of the epitaxial layers and substrates and the intensity is measured by the detector. Another possible method is using transmission electron microscopy (TEM), whereby information of the image with resolution down to atomic dimensions can be obtained. With a scanning tunneling microscope (STM), a sharp tip is brought close to a surface, and tunnel current is monitored.(45)

2.3.1 Manufacturing of Interband Cascade Lasers

An advantage of using quantum wells is the option to tune the wavelength depending on the intersubband transition energy by changing the barrier thickness and height as well as the well width and depth.(35) ICLs are fabricated via MBE chamber to let the matched heterostructures of InAs, GaSb, and AlSb, whereby the emission wavelength can be between 2.5 and 12 μm. The MBE chamber is equipped with a conventional effusion cell for the Al, Ga, and In as well as the Ti and Si dopants, and with a valved cracker for the As and Sb elements, which reduce the cross incorporation into the neighboring layers and adequate flux within the layers grown at different growth rates. Oxides are reduced in the Sb-rich atmosphere to achieve a smooth surface for the subsequent layers. First, the GaSb layer is grown, followed by the low-refractive-index cladding layer of InAs/AsSb superlattices, with growing temperatures between 400 and 450 °C. Changing the anion and cation amount within the interface of InAs/AlSb superlattice, the electrical and optical properties can be changed. Using a so-called soak time, AlSb and InSb interfaces can be forced, whereby InSb interfaces have more superior properties compared to that one with AlAs. Soak times can be avoided using the

This article was published in the *Encyclopedia of Analytical Chemistry* in 2021 by John Wiley & Sons, Ltd.
DOI: 10.1002/9780470027318.a9751

more reactive As_2 dimers, whereby strain-compensated superlattice with mixed interfaces can be grown. The interface composition in the superlattice by changing the flux ratio. The InAs laser is usually doped with Si, whereby the concentration is increased toward the active core to reduce the internal loss. GaSb layers are then followed to grow as a lower cladding layer with growing temperatures between 430 and 480 °C, which produces smooth surfaces for the subsequent cascaded active region. The As flux is a critical parameter, as too much As in the background lets the InAs/GaInSb interface get too rough and decrease the oscillator strength. Afterward, a GaSb separate-confinement layer, to reduce the waveguide loss, is grown, followed by an upper InAs/AlSb superlattice cladding. To avoid parasitic voltage drop, graded transition superlattices are inserted at the boundary between the various regions in the ICL structure. The ridges of the ICLs are produced, using the reactive ion etching (RIE) based on Cl- and Ar-plasma. After the dry etches, a cleaning with phosphoric wet etch step is done, which smooths the sidewalls and removes the contaminates. The etching has taken place below the active region to avoid current spreading, as the transport in the cladding and active region is anisotropic. The threshold current and efficiency are varying strongly with etching depth, ridge width, and stage multiplicity. If the etch is shallow, no sidewall passivation is necessary, even if the threshold current density is overestimated and the slope efficiency is underestimated due to current spreading. To prevent leakage or oxidation at the sidewall of the ICL, which is etched through the active region, passivation, as Si_3N_4 and SiO_2, is used to suppress excessive short-circuiting current. Another important part is the thermal management, as the thermal conductivities of the active core and the short-period InAs/AlSb superlattice cladding regions are low and highly anisotropic. To remove the heat from the active region, and increases the maximum operating temperature and output power, gold is electroplated on top of the ICL narrow ridges. Some lanes are unplated to make sure that there is still a high facet quality after the cleavage. The insulating passivation layer is opened on top of the ridge for contacting. Mounting ICL ridges epitaxial side down, thermal dissipation is enhanced, whereby the heat is directly transferred from the ridge to the heat sink, without passing through the substrate.[23]

2.3.2 *Manufacturing of Quantum Cascade Lasers*

MBE and MOCVD are used to process the QCL. The gain medium has to be inserted into an optical resonator cavity. The optical gain is achieved at the cost of thermal dissipation of 20–100 kW cm^{-2}, which is about 10–100 times larger than for a semiconductor interband laser (and 102–103 times larger than a solid-state laser). The optical cavity is directly formed by the epitaxial layers themselves. As already mentioned, the optical confinement in growth direction is obtained by total internal reflection between the high refractive index of the gain region and the low refractive index of substrate and cladding layer. One-dimensional waveguides allow long interaction length with minimizing the total volume and are favorable for thermal extraction. The waveguides can be produced either usage of the ridging process or the buried heterostructure process. The conventional process in semiconductor lasers is to etch only a fraction of the top of the cladding, whereby the effective index of the mode is slightly reduced on the side of the ridge. It supports a single transverse mode in even relatively long stripes in the rib waveguide and the low index step also reduces the optical scattering on the sidewalls. This etch yields in high peak power devices, but these QCLs have a large operation voltage. The anisotropic conduction properties of the active region result in a large current spreading.[45,80]

Ridge and buried heterostructure processes start the same. The active region structure is grown via MBE and then the samples are transferred in the MOCVD, whereby a planar regrowth of the cladding is conducted. Plasma enhanced vapor deposition (PECVD) is used to grow a layer of SiO_2 as a hard masking layer. Afterward, the patterning of the laser wavelength is defined and the pattern is transferred on the SiO_2 layer by RIE, using Ar/CHF_3. Due to the hard mask, InP cladding is then etched based on an HCl etching solution, whereby vertical sidewalls are obtained and the undercutting is reduced. By usage of an isotropic solution, the active region is etched, whereby a smooth surface in InP, AlInAs, and InGaAs is obtained after this etching step. Due to the isotropic behavior of the solution, the etched structure has an undercut, which is larger than the vertical etching depth. After this step, it can be now decided to do the ridging process or the buried heterostructures process. The ridge process is preferred to the conventional ones, as the active region is etched completely. Using this etch, it creates depletion layers and not nonradiative recombination sites. After the etching of the active stack, the hard mask is removed via HF etching, and an insulating layer is deposited on the etched structure. This step is crucial as the overlap of the optical mode with this dielectric layer is the most important source of optical losses in the waveguide configuration. To minimize the loss, SiO_2 or Si_3N_4 is used as insulating material. Via lithography or RIE, the insulating layer is opened on the ridge head and an ohmic contact is afterward deposited via e-beam evaporation. As of the last step, electroplated gold pads are deposited and the substrate is thinned to reduce thermal resistance and a back ohmic contact is deposited on the wafer bottom side. The advantages of the ridge laser process are (i) the simple process, (ii) standard

This article was published in the *Encyclopedia of Analytical Chemistry* in 2021 by John Wiley & Sons, Ltd.
DOI: 10.1002/9780470027318.a9751

clean-room processes (iii) good electrical and mechanical stability. Using narrow ridges long-wavelength devices, a large additional waveguide loss is observed, as Si_3N_4 and SiO_2 have large absorption coefficients at high wavelengths. After the active region wet etching, the buried heterostructure process is using a SiO_2 mask, whereby an insulating InP layer, which is iron-doped, is deposited, via MOCVD selectively on the sides of the ridges. Via HF etching the masking layer is removed, and an additional Si_3N_4 insulating layer is deposited via PECVD to prevent parasitic injection through defects. This layer is used, as it has a slightly higher thermal conductance compared to SiO_2. After finishing the device, the structure is then metalized like in the ridge process.(45)

InP is highly transparent and has a lower index step with the active region. It reduces the lateral roughness to the optical loss. InP has a large thermal conductivity and enables thermal extraction through the sidewalls. As InP is not an insulator, the leakage through the lateral confining layer occurs for buried heterostructures. The current will leak from the n-doped InP inside the semi-insulating InP to the substrate and is dependent on the nature of the blocking layer and the characteristics of the junction between the latter and top and bottom cladding. Current density through multibarrier AlInAs/InP structures still allows voltage build-up, but in samples with an iron-doped InP barrier the leakage current remains smallest; Fe:InP layers block current flow.(45)

Initial mounting for QCLs was the junction-up mounting with the usage of indium solder on copper submounts. The indium soldering accommodates the large thermal expansion mismatch of InP substrate and the submount. The disadvantage is that any residual dislocation has to cross the whole substrate before the active region is reached. Episode-down on AlN submounts are using high temperature, fluxless AuSn solder in a hermetically sealed, organic-free package, and it has kind of the same thermal expansion at room temperature compared to InP. Long-term chemical reactions are minimized in the device.(45)

3 SELECTED EXAMPLES FOR CASCADE LASERS

The first QCL presented by Faist et al.(13) had a three InGaAs/InAlAs coupled quantum well with three defined. Discrete electron levels in the active region and the superlattice, which are the injectors, are bridging the active regions in the 25 cascading structure. The emission is 8.5 μm at a wavelength of 4.16 μm and a maximum operating temperature of 88 K.(1) The first working GaAs/AlGaAs based QCL was published in 1998,(81) with a peak output of 70 mW per facet and a threshold current density of 7.3 kA cm^{-2}.(81)

ICLs operate at room temperature compared to QCLs with lower threshold current density and reduced power consumption at a wide wavelength range.(40) As ICLs do not need a big power supply, conventional batteries can be employed and they can be cooled via thermoelectric coolers.(82) ICLs can be also combined with detectors made from the same material and used then as monolithic and on chip-scale dual-comb frequency devices, which can operate at room temperature with low power consumption.(83) ICLs can be operated as dual-comb between 3 and 4 μm, build up as an on-chip source, needing less than 1 W of electrical power.(84) ICL with dual-beam (3.1 and 3.7 μm) can operate at 20 °C with a threshold current density of 215 and 158 A cm^{-2} in pulsed mode. This laser has two spatially separated active regions designed for short-wavelength (3.1 μm) and long-wavelength (3.7 μm), whereby the wavelength was adjusted via the thickness of the InAs layer in the 'W'-quantum well.(79) Other ICLs, e.g., are developed to work in CW between 2.8 and 5.7 μm,(79) as e.g. using BSG structures, stable single-mode emission could be achieved, which can be tuned independently in the six distinct channels in several single-mode wavelengths around 160 nm(72) or doping the injector regions heavily, whereby threshold currents of approx. 1 kW cm^{-2} at a temperature of 25 °C could be reached and at a wavelength of 6 μm, the ICL has in CW mode power densities reaching threshold with one magnitude lower than compared to comparable QCL.(85) Using two segments of BSG structures in one device, tuning through both segments lead to a small shift in the spectra. This configuration can emit at three different wavelength channels.(73) IC lasers can be operated up to 38 °C in CW mode, whereby the ring cavity ICL is mounted epi-side down to obtain an efficient heat extraction from the device. This ICL configuration uses a metalized second-order distributed feedback grating. The optical output is more than 6 mW operating at 20 °C. It has a single optical mode using epitaxial growth Bragg mirrors above and below the gain material. The ring device is based on second-order DFB, whereby wavelength selection is achieved and the outcoupling from the ring cavity through the substrate. The epi-side up mounting with a hole in the heat sink provides ICLs working in CW mode.(86) ICLs build-up from GaSb, can operate in CW mode up to 5.6 μm, but up to 7 μm in pulsed mode at room temperature, needs thicker claddings at longer wavelength, which makes the heat dissipation more difficult and waveguides via plasmon-enhanced structures with highly doped InAs layers.(87) By using mode-locked operation, ICLs generate picosecond pulses. At small modulation power, the ICL has a linear chirped frequency comb, characterized by

This article was published in the *Encyclopedia of Analytical Chemistry* in 2021 by John Wiley & Sons, Ltd.
DOI: 10.1002/9780470027318.a9751

a strong frequency modulation. Increasing the modulation amplitude, the chirp decrease until a broad pulse is buildup.[88]

QCLs can be used in the FIR range. The photon energy is lower than the optical phonon energy, so the optical phonon emission is not that dominant in the intersubband nonradiative channel.[89] THz lasers are still quite bulky and need cryogenic cooling.[90] Frequency combs were firstly developed with NIR and visible (VIS) range, whereas the MIR range could be fulfilled after the development of QCL, and then they could attend the THz range, too. In the QCL combs, frequency waves are modulated via a linearly chirped frequency ramp.[91] Dual combs spectroscopy have a complicated system that both combs are frequency stabilized, whereby the two beams have slightly different repetition rate. The wavelength can be changed by switching and locking it from the main broadband vertical transition in the active region to a narrowband diagonal transition from the injector to the lower level. By tuning the laser via injection current and temperature, depending on the diagonal transition energy on the bias field, a blue-chirp over the bandwidth can be obtained.[46,77] Frequency combs combine broad wavelength with a high spectral resolution, so stable frequencies over a large and continuous portion of the dynamic range of the laser can be obtained.[92] Comb generation can be conducted via down-conversion of NIR, mode-locked, ultrafast lasers with nonlinear crystals, or by pumping an ultra-high Q-factor micro-resonator with a CW laser, which depends on the optical components. The straighter forward method uses electrical injection, whereby a broadband, semiconductor frequency comb generator is used. The modes of a CW, free-running, broadband QCL which is phase-locked. The periodicity of the waveform at the round-trip frequency is important and not the generation of the high-intensity pulses, as the intensity of a perfectly frequency-modulated laser is constant, the power envelope would not be perturbed by the fast gain recovery as well as the spectrum is build up by equally spaced, discrete space lines.[93] Frequency combs can have, e.g., an output power of 300 mW at 50 °C by employing plasmonic waveguides.[94] Waveguide losses are different depending on their type, e.g. double metal waveguides have lower losses compared to surface plasmonic guiding.[95]

4 SELECTED APPLICATIONS OF CASCADE LASERS

In this section, different selected applications of cascade lasers and their optical designs will be described to provide a general overview of how versatile (cascade) laser spectroscopy is. Hence, different research fields, as environment, classical research in research facilities, and medicine will be shortly mentioned. Several comparisons with classical used FTIR devices will be pointed out, whereby the lasers have the same or even better performance. For instance, since environmental analysis often has to be conducted as real-time and infield measurements, the benefits of small and compact sensor devices, whose development has been made possible by the employment of cascade lasers, are here pointed out. Analytical values will be provided in Table 1, indicating the type of laser used, the wavelength regime, and the key figures of the used laser, as well as the analyte used and its limit of detection (LOD). If provided, the LOD of the FTIR device as a comparison will be provided too. In Figures 8–11 the schematic corresponding setups will be shown.

EC-QCLs are a broadband light source, covering a spectral range of several hundred wavelengths, using the Littman–Metcalf tuning, and first or direct feedback configuration. These lasers can work in liquid, gas, and solid phase.[96] Indeed, water interferences were tested and compared with FTIR, proving that lasers can operate in an aqueous medium.[128] Another benefit, of using cascade lasers, is the less power consumption compared to commercial FTIR devices. In contrast, FTIR devices have a significant advantage that they are broadband emitters, which enables the measurement of multiple analytes. Broadband laser radiation has reduced this advantage and the emitted radiation of a QCL can be analyzed with commercial FTIR. The radiated laser beam has been implemented into the FTIR device equipped with an L_2MCT detector, which leads to the laser emission spectra in a specific wavelength or wavelength regime.[96] The advantage of this configuration is that the laser spectra emission can be recorded, as well as using the FTIR broadband source in the optical setup, the direct comparison with the broadband source in the optical setup can be obtained.

4.1 Environmental Applications

Examples of analysis in the environmental field are often first carried out in research facilities and afterward, the same setup can be brought into the real world for infield measurements. Therefore, the setups are validated in laboratories, with elaborated measurement procedures under strictly controlled conditions. For this purpose, e.g. reference gases are first employed and then different mixtures are measured. The last step is then measuring in real-world scenarios, where different factors can affect the measurements.

Trace gas detection is one example. The detection of these gases, generally, starts with preliminary analysis in the laboratory, and then the validated method can

Encyclopedia of Analytical Chemistry, Online © 2006–2021 John Wiley & Sons, Ltd.

This article was published in the *Encyclopedia of Analytical Chemistry* in 2021 by John Wiley & Sons, Ltd.
DOI: 10.1002/9780470027318.a9751

Table 1 Applications of the cascade lasers for the investigation in environmental, waveguides, and medical fields

	References	Laser	Wavelength	Laser specification	Figures	Analyte	LOD
Environment applications	(96)	EC-QCL	1219–1297 cm^{-1}	PW: 0.5 µs F:100 kHz	Figure 8(a)	CH_3CH_2Cl CH_2Cl_2 $CHCl_3$	4 ppb 7 ppb 11 ppb
	(97)	2 EC-QCL	926–1178 cm^{-1} 865–920 cm^{-1}	TR: 30 000 cm^{-1} s^{-1} $t < 10$ & 4 ms	Figure 8(b)	C_3H_6, C_4H_8, C_4H_6, CH_3OH	n.a.
	(98)	FP-QCL	3003–3028 cm^{-1}	n.a.	Figure 8(c)	C_3H_8 C_4H_{10}	1 ppm
	(99)	QCL	1598–1602 cm^{-1} 1889–1894 cm^{-1}	Dual-beam pulsed	Figure 8(d) Figure 8(e)	NO NO_2 NO_x	1.5 ppb 0.5 ppb
	(100)	QCL	2180 cm^{-1} 2180 cm^{-1} 1900 cm^{-1} 1630 cm^{-1} 1381 cm^{-1}	2f-Wavelength modulation	Figure 8(f)	CO NO NO_2 N_2O SO_2	0.32 ppb_v 0.45 ppb_v 0.43 ppb_v 2.51 ppb_v
	(101)	QCL	2182–2198 cm^{-1}		Figure 8(h)	CO N_2O H_2O	0.211.40 ppb_v 0.18 ppb 0.21 ppm
	(102)	CW DFB-ICL	3.29 µm 3.34 µm	CW CW	Figure 9(a)	CH_4 C_2H_6	5 ppb_v 8 ppb_v
	(103)	CW ICL	3.34 µm	CW	Figure 9(b)	C_2H_6	239 ppb_v
	(104)	DFB-ICL	3.37 µm	CW	Figure 9(c)	CH_4	6–28 ppm_v
	(105)	CW FP-ICL	3.60 µm	CW	Figure 9(d)	H_2CO	25 ppb
	(106)	DFB-ICL	3–3.3 µm	SR: 23 Hz	Figure 9(e)	H_2CO	n.a.
	(107)	DFB-ICL	3.6 µm		Figure 9(f)	H_2CO	3 ppb
	(108)	CW-ICL	4.6 µm	CW	Figure 9(g)	CO	0.5 nmol mol^{-1}
Waveguide-based applications	(109)	EC-QCL	1565–1729 cm^{-1}		Figure 10(a)	Polystyrene	n.a.
	(110)	DFB-QCL	10.3 µm	PR: 2.64 µs	Figure 10(b)	Acetic anhydride	n.a.
	(116)	DFB-QCL	10.3 µm	P: 50 s Frequency 50 kHz		Acetic anhydride	18 pL
	(111)	EC-QCL	885–1925 cm^{-1}	PW: 100 ns RR: 100 Hz	Figure 10(c)	Benzaldehyde	35.1 mM FTIR: 46 mM
	(112)	EC-QCL	1570–1730 cm^{-1}	RR: 100 kHz	Figure 10(d)	Acetone in D_2O	200 pL
	(113)	EC-QCL	890–2020 cm^{-1}	PW: 400 ns RR: 100 kHz	Figure 10(d)	DMF	n.a.

(*continued overleaf*)

This article was published in the *Encyclopedia of Analytical Chemistry* in 2021 by John Wiley & Sons, Ltd.
DOI: 10.1002/9780470027318.a9751

Table 1 (*continued*)

	References	Laser	Wavelength	Laser specification	Figures	Analyte	LOD
	(117)	QCL		PW: 400 ns Period: 10 μs 20 nm wavelength per width		DMF	n.a.
	(118)	QCL	890–2020 cm^{-1}	PW: 400 ns RR: 100 kHz		Glucose	0.02 mg mL^{-1}
	(115)	QCL	900–1200 cm^{-1}	5% duty cycle	Figure 10(e)	Glucose	LOQ:35/55 mg dL^{-1} FTIR: LOQ: 100 mg dL^{-1}
	(114)	QCL	1570–1735 cm^{-1}	Resolution 1 cm^{-1}	Figure 10(d)	BSA γ-globulin Myoglobin	n.a.
Medical applications	(119)	EC-QCL	1500–1700 cm^{-1}	100 Hz PW: 500 ns	Figure 11(a)	BSA Lysozyme β-Lactoglobulin	1 mg mL^{-1}
	(126)	EC-QCL	1350–1770	100 Hz PW: 5000 ns	Figure 11(a)	BSA γ-Globulin Lysozyme	0.26 mg mL^{-1}
	(127)	EC-QCL	1470–1730 cm^{-1}	100 Hz PW: 5000 ns ScS: 1200 cm^{-1} s^{-1}	Figure 11(a)	Cas β-LG α-LA	0.28 mg mL^{-1} 0.071 mg mL^{-1} 0.077 mg mL^{-1}
	(120)	EC-QCL	1470–1730 cm^{-1}	Repetition rate 1 MHz PW: 200 ns ScS: 3600 cm^{-1} s s^{-1}	Figure 11(c)	Hemoglobin γ-Globulin Concanavalin A	0.0043 mg mL^{-1}
	(121)	QCL	850–1250	Noise: 2.99×10^{-7} cm^{-1} Hz^{-1}/ resolution: 0.1 cm^{-1}	Figure 11(d)	Acetone	0.05 ppm_v
	(122)	DFB-QCL	8.2 μm	CW	Figure 11(e)	Acetone	0.51 ppm_v
	(123)	DFB-QCL	4.61 μm	CW	Figure 11(f)	CO	7 ppb_v
	(124)	DFB-ICL	4.69 μm	CW	Figure 11(g)	CO	0.6 ppb_v
	(125)	DFB-ICL	4.35 μm	CW	Figure 11(h)	CO_2	n.a.

Type of laser, wavelength used, laser specification, analyte, and LOD, when mentioned, are listed. The schematics of each setup has been referred to the figures already mentioned in this section. Abbreviation: SR, sweep rate; PW, pulse width; ScS, scan speed; TR, tuning rate; t, time; R, resolution; F, frequency.

This article was published in the *Encyclopedia of Analytical Chemistry* in 2021 by John Wiley & Sons, Ltd.
DOI: 10.1002/9780470027318.a9751

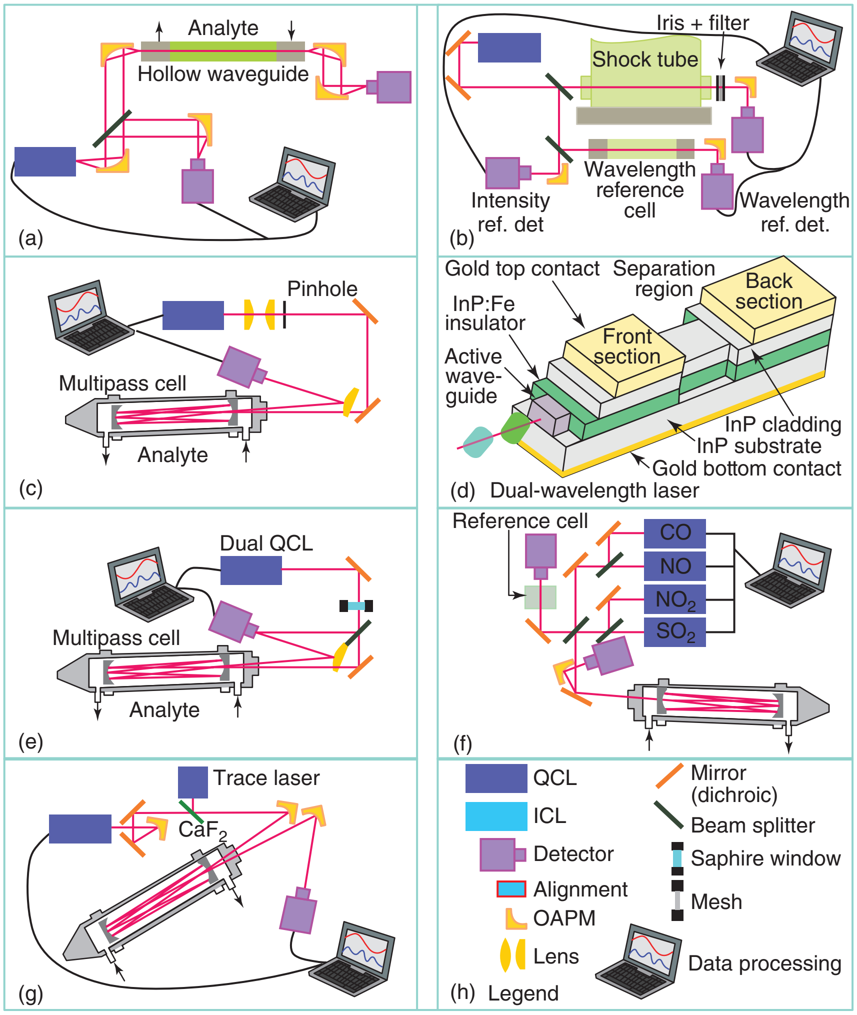

Figure 8 Setup developed for (a) CH_3CH_2Cl, CH_2Cl, and $CHCl_3$. (Adapted from Young et al.[96]) (b) C_3H_6, C_4H_8, C_4H_6, and CH_3OH. (Adapted from Strand et al.[97]) (c) (Adapted from Jágerská et al.[98]) (d) Laser setup. (Adapted from Jágerská et al.[99]) (e) C_3H_8, C_4H_{10}. (Adapted from Jágerská et al.[99]) (f) CO, NO, NO_2, N_2O, and SO_2. (Adapted from Genner et al.[100]) (g) CO, N_2O, and H_2O. (Adapted from Li et al.[101]) (h) The legend shows the schematic of the different optical parts, which are used in Section 4.

be used in the real-world scenario. Therefore, sensitive and selective trace gas detection of, e.g., ethyl chlorides, dichloromethane, and trichloromethane, is investigated. The optical setup consists of focusing the EC-QCL beam on a custom-made hollow waveguide, with an internally coated Ag/AgI layer. This serves as the transducer, waveguide, and miniaturized gas cell, and is then focused on the detector, as shown in Figure 8(a). Although lasers have their emission spectra, the absorbance of molecules affects the characteristic laser emission feature. Absorption lines of gases have narrow bandwidth and therefore demand a maximized sensitivity and selectivity for the lasers. The gas samples are exponentially diluted with different concentrations and gaseous IR spectra are measured, which is a commonly accepted method for preparing trace-level sample dilutions. The resulted IR spectra are then correlated with the laser emission. As each of the gases has its unique fingerprint, simultaneous measurement of the three analytes is feasible. Each sample was measured over more than 80 min, and the LOD was calculated from the smallest detectable analyte concentration using the exponential dilution theory. It is possible that more relevant gaseous samples can be determined in the compact gas sensing system.[96]

High temperature and high-pressure gaseous measurements are another relevant subjects of interest, as gases in high-enthalpy thermodynamic states are present in several environmental scenarios, including astrophysics, environmental science, chemical engineering, plasma physics, combustion science, as well as aerospace, chemical, and energy systems engineering. The combination of a shock tube equipment

Encyclopedia of Analytical Chemistry, Online © 2006–2021 John Wiley & Sons, Ltd.
This article is © 2021 John Wiley & Sons, Ltd.
This article was published in the *Encyclopedia of Analytical Chemistry* in 2021 by John Wiley & Sons, Ltd.
DOI: 10.1002/9780470027318.a9751

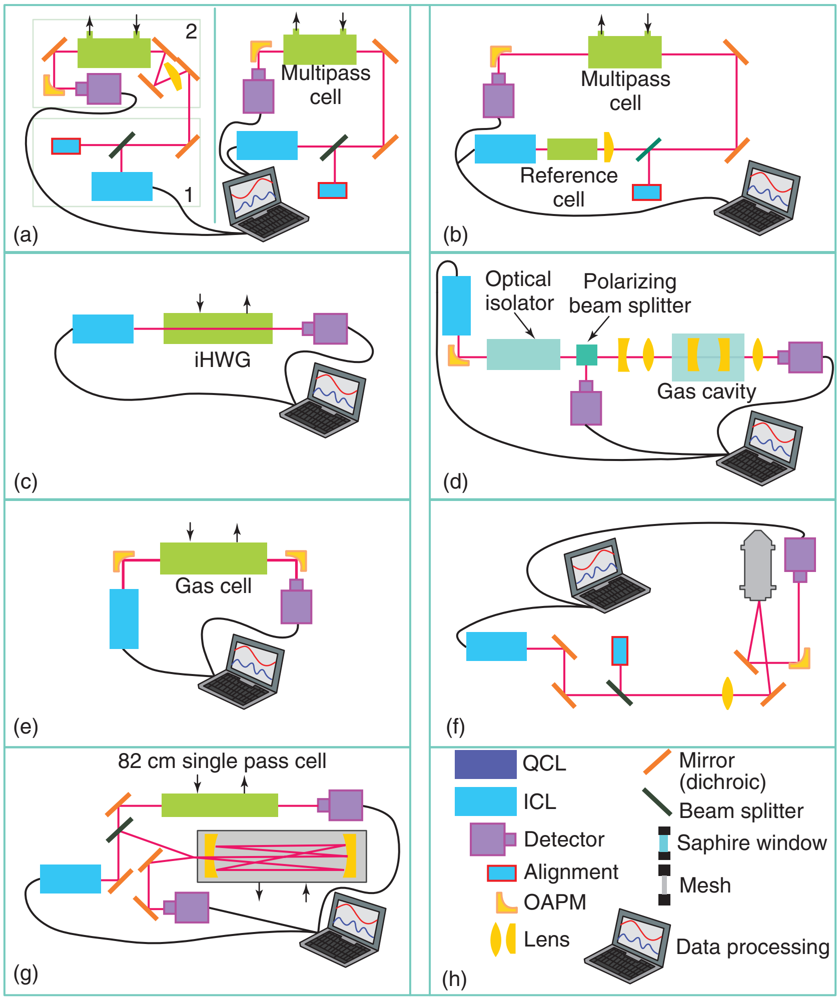

Figure 9 Setup developed for (a) CH_4 and C_2H_6. (Adapted from Dong et al.[102]) (b) C_2H_6. (Adapted from Li et al.[103]) (c) CH_4. (Adapted from Tütüncü et al.[104]) (d) H_2CO. (Adapted from Ixin et al.[105]) (e) H_2CO. (Adapted from Lundqvist et al.[106]) (f) H_2CO. (Adapted from Yao et al.[107]) (g) CO. (Adapted from Nwaboh et al.[108]) (h) The legend shows the schematic of the different optical parts, which are used in Section 4.

with a broadband QCL provides high-pressure and high-temperature absorption spectra of several gases. Different infrared databases are focused more on the near room temperature and atmospheric pressures, or there are high-temperature spectral databases for selected analytes, but no databases are available for high pressure and high temperature. Gaseous IR measurements in 'hot' environments lead to an increased number of vibrational modes in the spectra. High-temperature measurements also demand time ranges between 100 ms up to several minutes with a stable composition, temperature uniformity, and thermodynamic equilibrium. High pressure and high-temperature measurements, in contrast, are performed in a very short time range of 1–10 ms. Commercial FTIRs have, however, a too slow acquisition rate to obtain broad spectra and require a laboratory approach, which does not fit the thermodynamic accuracy and range. QCLs in contrast provide the fast measurements and data acquisition that are needed for these measurements. For example, the used EC-QCL, tuned with less than 10 ms and a tuning rate of 30 000 cm^{-1} s^{-1}. In this article, they achieved a spectral range between 8.5 and 11.7 μm with a temperature between 811 and 1622 K and a pressure range of 1–5 atm. The configuration is depicted in Figure 8(b). In this setup, two laser modules are used, concerning the rapid ultra-broad wavelength tuning laser within the test time of the shock tube. The laser was focused on the shock tube and an MCT detector was employed. With the beam splitters, the laser light was guided to both the wavelength reference and the intensity reference detectors, to correct laser intensity variation during the

Encyclopedia of Analytical Chemistry, Online © 2006–2021 John Wiley & Sons, Ltd.
This article is © 2021 John Wiley & Sons, Ltd.
This article was published in the *Encyclopedia of Analytical Chemistry* in 2021 by John Wiley & Sons, Ltd.
DOI: 10.1002/9780470027318.a9751

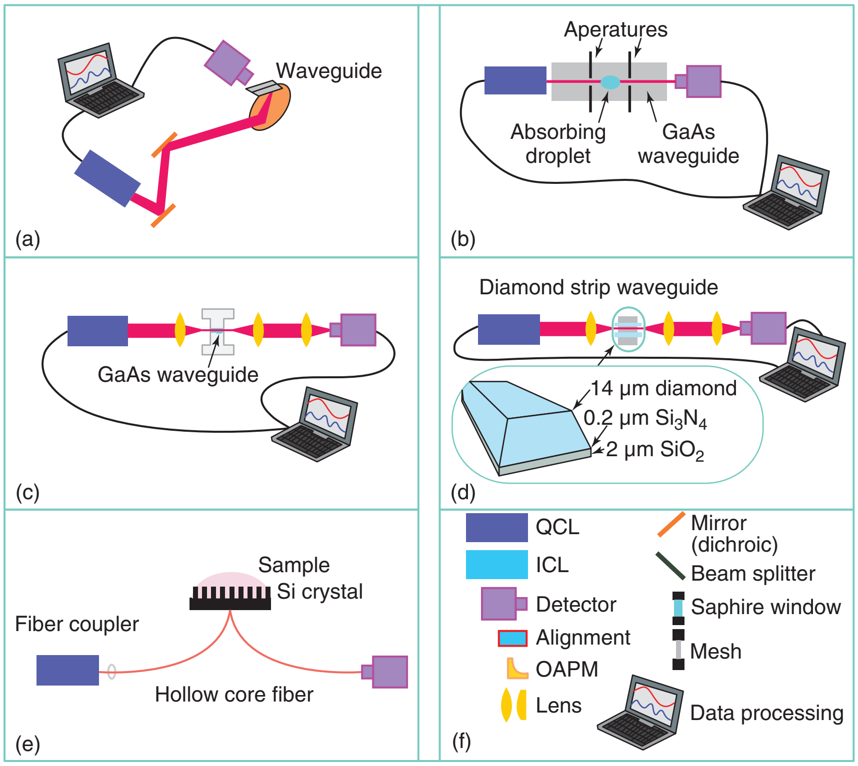

Figure 10 Setup developed for (a) Polystyrene. (Adapted from Ramer et al.[109]) (b) Acetic anhydride. (Adapted from Charlton et al.[110]) (c) Benzaldehyde. (Adapted from Sieger et al.[111]) (d) Acetone, DMF, and Protein. (Adapted from Wang et al.[112]; Haas et al.[113]; Lopez-Lorente et al.[114]) (e) Glucose. (Adapted from Jernelv et al.[115])

experiment and to see the absorption features at room temperature. For this purpose, the gas cell was filled with a mixture of components and provided an absolute wavelength reference to correct the variations in the wavelength tuning performance. Ethylene (C_2H_2) is an interesting analytical analyte for high-temperature and high-pressure measurements, due to the lack of experimental absorption spectroscopy. From the environmental point of view, ethylene is a key intermediate species in fuel pyrolysis, being a pyrolysis product in modern ablative thermal protection systems for atmospheric entry vehicles and thus influences both boundary layer flow fields, kinetics, and radiation, as well as it is found in many substellar objects, as e.g. the brown dwarf. Measuring with the condition of high temperature and high pressure, new absorption peaks could be found, which were not predicted by different databases. The setup above described is not limited to the detection of ethylene, since other gases such as propene, 1-butene, 2-butene, 1,3-butadiene, and methanol can be measured too. Therefore, this setup is prone to measure any sample in a wavelength regime between 4 and 12 μm with a temperature of 10 000 K and pressure of 1000 atm.[97] The detection of propane and butane is also an important issue, as these analytes are the most relevant hazardous gases when referring to gas leakage in aerosol cans. Leakage tests are important for the packaging industry, where it is necessary to nondestructively investigate both the tightness of filled aerosol cans and the purity of their contents. It is well known that leaks of these gases can pose fire and explosion hazards. Commercial tests, known as hot water bath test, typically consist of immersing the aerosol cans in a hot water bath to detect gas leaks from the cans. This test can detect leak rates of 1.2×10^{-4} standard liters per minute (slpm), however, this approach is quite bulky, energy consuming, and costly. Laser spectroscopy offers the benefits of a compact, simple, and reliable alternative method. For instance, a Fabry–Perot QCL (FP-QCL), which emits at 3 μm, provides sufficient sensitivity and speed to compete with industrial water bath testers, where the leakage is detected by the occurrence of gas bubbles in a water bath. Since propane has broad and quasi-structure absorption spectra, which do not require a high spectra resolution, FQ-QCL is a perfect candidate for fast leak-detection, without the need for detailed spectral analysis. Despite some disadvantages due to their broad emission, FP lasers have several advantages, as they have high sensitivity due to the long

Encyclopedia of Analytical Chemistry, Online © 2006–2021 John Wiley & Sons, Ltd.

This article was published in the *Encyclopedia of Analytical Chemistry* in 2021 by John Wiley & Sons, Ltd.
DOI: 10.1002/9780470027318.a9751

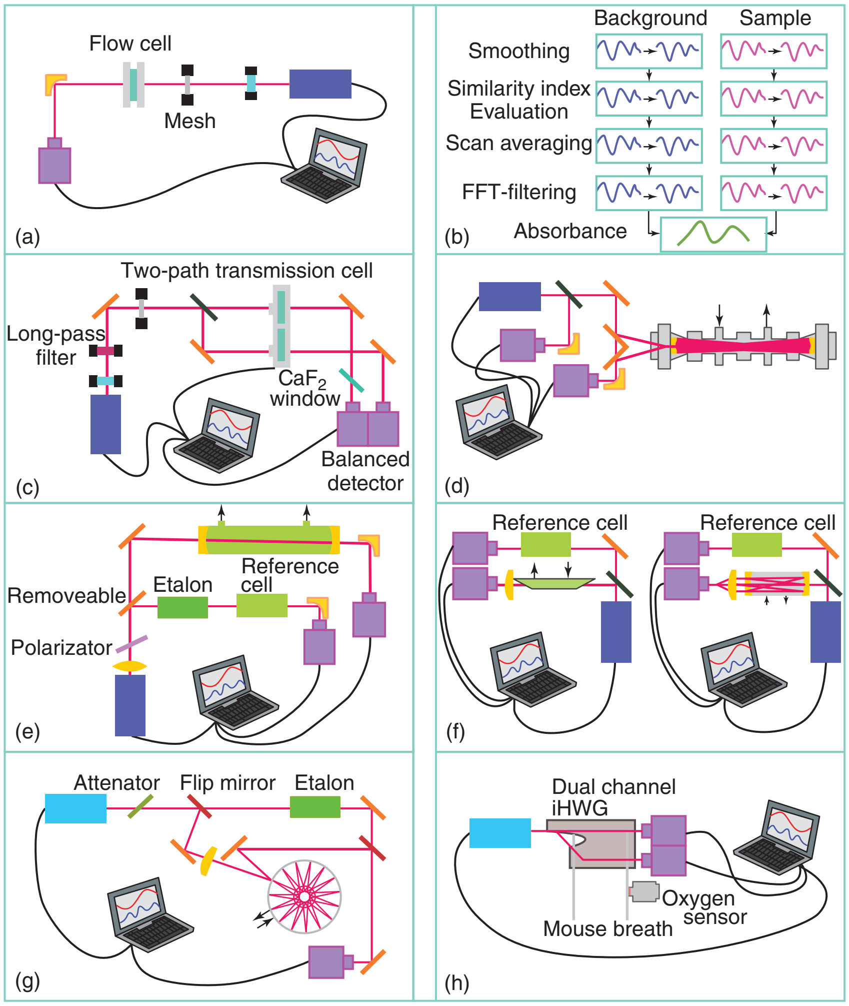

Figure 11 Setup developed for (a) BSA, Lysozyme, and β-Lacto globulin. (Adapted from Schwaighofer et al.[119]) (b) (Adapted from Schwaighofer et al.[119]) (c) Hemoglobin, γ-Globulin, and Concanavalin A. (Adapted from Akhgar et al.[120]) (d) Acetone. (Adapted from Reyes-Reyes et al.[121]) (e) Acetone. (Adapted from Ciaffoni et al.[122]) (f) CO. (Adapted from Pakmanesh et al.[123]) (g) CO. (Adapted from Ghorbani and Schmidt.[124]) (h) CO_2. (Adapted from Tütüncü et al.[125])

optical path of the cell and allow work to be performed in isolation from the surrounding environment, which is important in industry, where residual hydrocarbon gases and water vapor can interfere with the measurement. Using a pinhole after the laser radiation, a collimated beam can be obtained and reduces the laser peak power to avoid saturation effects on the detector as well as reduces the numerical aperture of the laser beam and improves the optical signal, as shown in Figure 8(c). This setup can be applied in the different nondestructive analyses such as sealed pharmaceutical and petrochemical products.[98]

Other gases, such as NO, NO_2, and NO_x, which are often measured simultaneously, can be analyzed using a dual-beam laser, with two single laser beams emitting at 1600 and 1900 cm^{-1}. DFB-CLs have an extremely narrow spectral emission with tailorable frequency between 3 and 25 μm, and a small coverage of 10 cm^{-1}, leading to a one compound one laser measurement strategy. EC lasers have a tuning range of 100 cm^{-1}, and at the same time, they have a less measurement rate. Alternatively, as mentioned before, QCLs can combine the broad tuning range with a large measurement time. Two single waveguide beams can be generated within one single waveguide, and, as shown in Figure 8(d), the emission directions are strictly identical, so no additional laser modules or optics are needed. The wavelengths are spectrally separated, with almost the same threshold current of both emitting frequencies and a limited operation temperature region to 30 °C. The linewidth of both laser beams is determined by thermal chirp and is used in short pulses of about 5 ns. Nevertheless, the output power of the front

Encyclopedia of Analytical Chemistry, Online © 2006–2021 John Wiley & Sons, Ltd.

This article was published in the *Encyclopedia of Analytical Chemistry* in 2021 by John Wiley & Sons, Ltd.
DOI: 10.1002/9780470027318.a9751

and back section differs due to the poor light extraction from the strongly over-coupled back DFB resonator. In addition, the nonreciprocal geometry of the laser affects the emission from the back section, as the light passes then through the unbiased laser front section and gets attenuated and scattered. Simultaneous threshold driving of the inactive section can compensate for this effect and increase the emitted power from the back laser part. In the optical setup, a sapphire window acts as an optical short-pass filter, cutting off at 6 μm wavelength and reducing the optical power, as shown in Figure 8(e). In the multipass gas cell, the gaseous analytes are inserted, and afterward, the beam is detected. There is a delay due to the 36 m pathway inside the gas cell, so it is possible to temporarily resolve and normalize the reference and the pulsed signal using a single detector, thus reducing the signal noise. After the system was validated, field applications could be conducted. Therefore, exhaust gas was sampled directly after the treatment system in an engine test bench for 30 min in a certification test for on-road heavy-duty engines. The same setup was also used to measure ambient NO and NO_2 at outdoor ambient air, revealing promising results for the fast detection of these gases after an exhaust treatment system of a heavy-duty diesel engine.(99) Gases such as NO, NO_2, CO, N_2O, and SO_2 are also arising from diesel. These gases are toxic and affect significantly the air quality in industrial cities. By combining several QC lasers and coupling them into a commercial multipass gas cell, these gases, arising from diesel, gasoline, or the resulting flue gas, can be simultaneously measured, since their absorption lines of are well separated. Thus, four individual lasers are employed and combined with several beam splitters and the laser beam is then guided into the multipass gas cell, as shown in Figure 8(f). Combining all optical parts in a server rack, with dimensions of $48 \times 65 \times 18$ cm, this setup is possible to be used in mobile applications. A 2f-wavelength modulation is used, whereby the laser is tuned over an absorption line and is attenuated by the presence of the analyte. Before using as infield measurement, the system was validated in the laboratory and then measurements were performed in the external environment. Correlating the spectra obtained under defined conditions in the lab with field measurements, showed that this mobile sensor concept is a promising tool for real-time real-world measurements.(100)

Carbon dioxide and methane are among other primary greenhouse gases and contribute to global warming and climate change indirect or direct. Water vapor is also a greenhouse gas, which regulates the planetary temperature through absorption and emission of radiation, and carbon dioxide is a key reactant in the oxidative chemistry of the Earth's atmosphere. The whole sensor, used to monitor these gases, is mounted on a $50 \times 50 \times 3$ cm^3 optical breadboard, which makes it capable of infield measurements. The laser can simultaneously detect CO, H_2O, and N_2O, by filling them into the multipass gas cell. An alignment laser is implemented to facilitate the alignment, as shown in Figure 8(g). The whole prototype can be placed on a moveable rack. For optimizing the parameters, an optical gas flow is used, as the pressure changes the spectra. The WMS-2f signal amplitude depends on the laser modulation index, which is defined as the ratio of the wavelength modulation amplitude and the half-width at half maximum of the absorption profile. The 2f signal amplitude is maximized to obtain the highest SNR. By increasing the signal averaging time, a three to fivefold improvement could be achieved.(101)

Besides the QCL, ICL is also used in environmental fields. For the trace gas detection, which includes environmental monitoring, industrial process control, and monitoring of gas concentrations at industrial locations or breath gas analysis, fast, accurate, and precise measurement of small concentrations of the trace gases are required. Tuneable diode laser absorption spectroscopy (TDLAS) is a versatile technique for real-time analysis of gases, by which parts per trillion (ppt)-level concentrations of these gases can be measured. TDLAS offers narrow spectral resolution, and it is dependent on the laser sources, as a single-mode DFB laser is needed. Reducing the conventional dimension of the Herriott multipass gas cell, a smaller footprint, as well as a reduced amount of gas, is required. This design consists of two concave spherical mirrors with a more complex dense spot pattern that minimizes the laser beam spot overlap with a 54.6 m path length and a 220 mL sampling volume, reaching a total size of $17 \times 6.5 \times 5.5$ cm. Two sensor concepts are here developed. Both are portable. The first one has a two-floor structure and the second one is located on one floor, as depicted in Figure 9(a). The two-stage setup consists of a CW-DFB-ICL located on the first floor and the laser beam is guided via mirrors into the second floor, where it is focused on the MPGC and then into the detector. Two floors are used to obtain a compact sensor system. The same sensor concept can be realized in a one-floor setup. Both setups have identical control units. The two-floor setup is equipped with an ICL (3.2 μm) for methane measurement and the one-floor setup with an ICL (3.3 μm) for ethane measurement. Both setups use identical control units and equipment. Infield measurements are carried out with the two-floor setup, as this sensor is located in a driving car and the power is provided via a laptop battery. Measurement was carried out while the car was driving.(102) Using almost the same one-floor setup, as seen in Figure 9(b), ethane can be measured. Ethane is the second-largest compound in natural gas and influences the atmospheric chemistry

Encyclopedia of Analytical Chemistry, Online © 2006–2021 John Wiley & Sons, Ltd.

This article was published in the *Encyclopedia of Analytical Chemistry* in 2021 by John Wiley & Sons, Ltd.
DOI: 10.1002/9780470027318.a9751

and climate. The gas is a trace gas with a concentration of levels of several parts per billion by volume (ppb_v) and is important in human breath analysis as a noninvasive method to monitor and identify diseases. The laser was modulated with a 2*f*-wavelength and 2*f*/1*f* wavelength modulation spectroscopy. The sensor system has a size of $17.0 \times 6.5 \times 5.5$ cm^3 and can measure in ppb_v levels of ethane, as the sensor can be optimized using the 2*f*/1*f* wavelength modulation spectroscopy.[103]

Methane is a relevant target molecule in various medical and environmental processes. It is continuously released resulting from anaerobic oxidation of leakage from, e.g., methane hydrate deposits, domestic animals, etc. Methane is therefore an important greenhouse gas. Despite the Herriot gas cell, the substrate integrated hollow waveguides (iHWGs) can be used to measure gas samples, as shown in Figure 9(c). These iHWGs have an extended optical path and a small sample volume is adequate. In this setup, an Al-iHWG is used, which serves simultaneously as a miniaturized gas cell and waveguide. Calibration curves with methane concentrations of 50 to 400 ppm_v were achieved.[104]

Formaldehyde (H_2CO) is a colorless, toxic, combustible, carcinogenic gas and is used in household products. The daily permissible H_2CO exposure is 750 ppb averaged for an 8-h workday and a short-term exposure limit of 2 ppm over 15 min in maximum. A cavity of 2 cm with an optical path length of 20 m was used to measure formaldehyde. The principle in this setup is the cavity-enhanced absorption spectroscopy (CEAS), in which the optical cavities are used to enhance light interaction with a gas species inside the cavity. Tuning is conducted via temperature change in steps of 0.012 °C. The selected wavelength assures the interference-free measurement of H_2CO, targeted at around 3.6 μm. The sensor is built up with an optical isolator, to prevent the reflected light from the cavity from returning to the ICL and being guided into the cavity-enhanced sensor, as shown in Figure 9(d). The LOD of 25 ppb is obtained after a measurement time of 1-s average time. By increasing the average time to 200 s, the LOD could be even decreased to 2.8 ppb.[105] Formaldehyde is also used in the manufacturing and composition of industrial products, e.g. resins for extremely strong and permanent adhesives of wood-based panels. It is classified since 2004 as carcinogenic to humans by the International Agency for Research on Cancer (IRAC). The current workspace exposure for formaldehyde in Europe is 2 ppm with a time average of 8 h. Online monitoring is needed to gain tighter control of emission levels, as well as real-time measurements with a highly sensitive formaldehyde emissions monitoring of the exposure of the workspace. Hence, a 3.6 μm ICL and a 36 m long multipass gas cell was used, as shown in Figure 9(e). DFB-ICL can be used to measure this gas, even if it is mixed with methanol and formic acid, to stabilize formaldehyde. Comparison with theoretical FTIR spectra obtained from a database shows the same behavior in the spectra. DFB-ICLs are therefore able to monitor formaldehyde in the workspace.[106] Formaldehyde is one of the most common indoor air pollutants, which can cause eye, nose, and respiratory irritation and allergies. Another approach is to use metal-organic framed (MOF) based filters, which can be used to control air pollution control due to their large surface area and rich functionalities. Therefore, an ICL sensor concept for sensitive and fast quantification of formaldehyde during the filtration process of the MOF filter can be used. This sensor is built up from an ICL, whereby the laser beam is guided to the multipass gas cell, with a volume of 0.3 L and a total length of 36 m, as shown in Figure 9(f). The sensor was calibrated by a custom-designed permeation H_2CO generator that produces H_2CO/N_2 mixtures, consisting of a semi-permeable membrane in the tube wall, so the gas flows through the membrane. For real-time monitoring, the formaldehyde sensor was applied to investigate the filtration efficiency of H_2CO membranes (the MOFs). These membranes consist out of a hybrid porous crystalline material, which can be used for gas storage and separation. The MOFs were treated with different gases and the filtration performance was in real-time controlled. Continuous monitoring over a time of 240 min, confirmed that the formaldehyde filtration of the membranes can be measured with a time resolution of 1 s.[107]

Carbon monoxide has an indirect effect on global warming. Gas analyzers are calibrated with static gas standards, whereby errors in real-world scenario measurements can occur. Therefore, there is an increasing demand for the improvement of lab calibration for the real-world samples. CO analysis can be performed using a sensor built up with an ICL at 4.6 μm and two gas cells. One cell is used for the CO amount fraction in the μmol mol^{-1} range and the other, the Harriot cell, to measure the amount fractions in the nmol mol^{-1} range, as shown in Figure 9(g). Air-broadening, collisional broadening, and line strength must be considered. The sensor device was calibrated using a mixture fraction of CO, N_2, and air. The sample flow was 1 L min^{-1} and the 76 m long path length provided a detection limit of 0.5 nmol mol^{-1}, with a total measurement time of 14 s. Measurements of the CO amount-of-substance fraction had a LOD of 0.06 and 0.01 nmol mol^{-1} with a measuring time of 10 min. As a result of this LOD, the sensor device allows the detection of CO below the 2 nmol mol^{-1} target specification required from the WMO application. The measurement range is then between 0.1 and 1000 μmol mol^{-1} and can be used also for industrial applications. However, despite showing a

This article was published in the *Encyclopedia of Analytical Chemistry* in 2021 by John Wiley & Sons, Ltd.
DOI: 10.1002/9780470027318.a9751

good comparison with a commercial cavity ring-down spectroscopy-based CO analyzer, this sensor concept is not able to use in-field measurement.[108]

4.2 Applications using Waveguides

Single-mode waveguides can be coupled with QCLs. Waveguides are active transducers, which ensures a reproducible interaction between photons and molecules and can enhance the signal.[129] Only fewer groups are using the ridge or slab waveguides, which are fabricated on top of a thick substrate medium, which can be increased and allows a single-mode propagating through the waveguide. The coupling of the light into the end facet of the waveguide is sensitive to the laser vibrations, and the thin waveguide makes it difficult to focus the light on the facet. For this reason, grating couplers could afford an efficient coupling at beam diameters above the diffraction limit. To achieve broadband coupling, different coupling angles are needed. Coupling in the waveguide with a diffractive element is a resonance phenomenon, so the beams can simply overlap with the different coupling angles and can be realized by focusing a wide beam on a small spot. Therefore, the laser beam is focused on the grating. In the setup, shown in Figure 10(a), the laser beam is focused on mirrors, guiding the light into the waveguide and reaching the detector. Solid polystyrene was, for instance, measured.[109] Waveguides, built up from GaAs, are designed to facilitate the propagation of a single-mode at a wavelength of 10.3 μm, which can be used to measure acetic anhydride. These single-mode waveguides are designed to improve the sensitivity of the evanescent field and are built up as a miniaturized platform for a liquid-phase sensing system. The waveguide consists of a 6 μm $Al_{0.2}Ga_{0.8}As$ cladding layer, which is followed by a 6 μm GaAs core layer. The waveguides were coupled into an FTIR device to obtain a transmission spectrum. Acetic anhydride was measured with a droplet volume of 0.5 μL. The laser beam was guided via lenses into the facet of the waveguide and then to the detector, as shown in Figure 10(b). This waveguide provides a well-defined evanescent field at the waveguide surface with a sharp decrease in the surrounding material. GaAs thin-film waveguides are ideal for sensitive and quantitative measurement of molecular monolayers, which are deposited on the waveguide surface.[110] Instead of using a slab waveguide, strip waveguides, with a dimension of 200 μm, can be also fabricated. Acetic acid with a volume of 2 nL can be measured via DFB-QCL, emitting at 10.3 μm. In a comparison of the planar waveguide, the LOD is here 0.8 pL (based on the volume) and the strip waveguide is 0.05 pL (based on the volume). Using narrow strip waveguides can improve the achievable LOD due to the enhancement of the local electric field.[116] The waveguide core enhances the fraction of the energy within the evanescent field and it affects the obtainable SNR and the overall sensitivity of the absorption measurement. The intensity of the evanescent field depends on the dielectric constant at the waveguide-sample interface and the dimension of the waveguide. A 6 μm thick waveguide, e.g., provides higher sensitivity in comparison to a 10 μm thick waveguide, which is about 10 ties lower. The light is focused on the side facet and benzaldehyde can be measured. The obtained spectra were compared with FTIR. While the laser reached a LOD of 35.1 mM, FTIR devised achieved a LOD of 46 mM. The setup using a GaAs thin-film waveguide is a build-up that uses two lenses, which focus the light on the facet of the waveguide and a third lens that focuses the light on the detector, as shown in Figure 10(c).[111]

In semiconductor (GaAs/AlGaAs), thin-film waveguides developed by Mizaikoff and collaborators,[112] with a spectral window of 13 μm, diamond serves as an excellent thin-film waveguide. Diamond strip waveguides (DSWGs) are prepared via chemical vapor deposition and inductively coupled plasma. The thickness of the diamond is 14 μm grown on a 200 nm Si_3N_4 and 2 μm thick SiO_2 layer and the bottom builds a 600 μm thick Si wafer substrate. The Si_3N_4 layer is used, as it provides a better adhesion on the diamond, and SiO_2 is needed due to the mismatch of the refractive index of the diamond and Si wafer. The different stripes have a width of 100, 250, and 500 μm. In this setup, collimated lenses are focused on the diamond facet, as shown in Figure 10(d). The transmission spectrum is done via an FTIR device, resulting in a broadband transducer. As the 100 μm thick waveguide has the highest transmittance, the measurements were conducted with this strip waveguide. Droplets of different concentrations of acetone in deuterated water were measured and compared with the already mentioned GaAs strip.[112] Reducing the thickness of the waveguides leads to an increased number of internal reflections until a uniform evanescent field surrounding the internal reflection element (IRE) is established, i.e. when the geometrical dimensions are closed to the supported wavelength with the IRE serving as a waveguide. Diamond has its limitation in the spectral region between 2200 and 1800 cm^{-1}, which refers to the two-phonon crystal lattice absorption feature. Diamond in comparison to GaAs has a lower refractive index and the IR radiation is more weakly confined within the diamond structure and has a triangular spreading along the propagation axis. Propagation losses are pronounced as the decoupling via side facets is more complex. To circumvent this condition, horizontal structuring increases the radiation efficiency. Using a free-standing waveguide, e.g., DMF could be

Encyclopedia of Analytical Chemistry, Online © 2006–2021 John Wiley & Sons, Ltd.

This article was published in the *Encyclopedia of Analytical Chemistry* in 2021 by John Wiley & Sons, Ltd.
DOI: 10.1002/9780470027318.a9751

measured.[113] Different diamond stripes with different thicknesses were grown on a silicon frame, providing the IRE. Here acetone and dimethylformamide (DMF) were measured on 14 and 500 μm thick waveguides. Interestingly, the different thicknesses of the diamond stripes showed that some of them broke, when the solution was added.[117] Freestanding diamonds, which are supported with a Si frame, are a tradeoff between stable growth and refracting matching. These diamonds remain brittle and they are mechanically sensitive, as already mentioned. In contrast, for bulk diamond IRE, this is not a concern. Diamond waveguides were used to measure saliva. Samples with a volume of 20 μL saliva from a healthy person were collected, and the saliva with and without the drunk sugary content drink was measured. The amide I band at 1650 cm^{-1} and the amide II band at 1550 cm^{-1} as well as the asymmetric stretching mode bands of carboxylate at 1400 cm^{-1} are investigated. The glucose vibration occurs at 1030 cm^{-1}. Comparison with glucose solution shows that a LOD of 0.02 mg mL^{-1} (0.12 mmol L^{-1}) can be obtained, which fits to biological relevant concentrations in saliva, containing concentration between 0.008 and 0.0105 mg mL^{-1} and saliva glucose levels in diabetic patients ranging from 0.04 to 0.14 mg mL^{-1}.[118] Glucose can be also measured using a microstructured Si IRE, which can be compared with commercial FTIR device. In both measurements, the same concentration ranges were measured. Hollow-core fibers were used to guide the laser beam to the Si crystal and to the detector, as shown in Figure 10(e). The overall absorbance of the OCL setup was approx. 4.5 times higher compared to FTIR. FTIR has in this specific range a lower absorbance signal and therefore higher LOQ. It could be also shown that due to the alignment, some small differences between the FTIR and QCL peaks are obtained.[115]

Proteins are also analyzed with diamond stripe waveguides. Nearly the same setup as mentioned above is used, in which lenses focus the laser beam onto the facets and then onto a detector, as shown in Figure 10(d). A 5 μL solution for the waveguides was used to measure three different proteins. For comparison, the same analytes were analyzed with a conventional FTIR device equipped with diamond IRE. Both measuring principles provided the same behavior in IR spectra. The obtained absorbance in the laser-based setup was higher compared to the conventional FTIR, whereby the concentration in the laser-based system was in total higher. A sensitivity improvement of about fourfold is observed compared to the FTIR measurements. The amine bands in the laser setup are slightly different compared to the FTIR. This slight difference might occur due to the laser and the different transducers.[114]

4.3 Medical Applications

Broadband QCLs, with a spectral coverage of 400 cm^{-1}, and a high signal-to-noise ratio (SNR), provide ideal fast, compact, real-time measurement and a rugged laser source for the protein I and II region. FTIR analysis is well-established and is the most widespread instrumentation in this spectra regime, equipped with a broadband light source, with less power radiation. The less power radiation, however, can lead to limitations of the analytes in presence of a highly absorbing matrix as water. For example, the amide I band, located at 1643 cm^{-1}, overlaps with the water HOH bending. FTIR spectroscopy is considered the gold standard, as it has a broad spectral range, covering the whole MIR range, excellent SNR, and absolute wavenumber accuracy. FTIR spectra have notoriously low noise and the final noise is determined by the detector. The optical path is restricted to <10 μm to avoid total IR absorption in FTIR transmission measurements. The short path length, however, leads to less sensitivity due to the lower band absorbance and the limited robustness due to the higher probability of cell clogging. High protein concentrations, above 10 mg mL^{-1}, are required, as the low path length limits the IR band intensity and the SNR at a given concentration.

The spectral density of QCL is, in contrast, to a factor of 10^4 higher compared to FITR devices. As QCLs have higher output power, and a longer path length in transmission measurement, they achieve a factor of 4–5 longer for both glucose and proteins compared to FTIR.[119,126] With the broadband spectral tuning of several hundred wavenumbers, the QCLs are used for studies in aqueous media. They also have a four to five times larger optical path compared to FTIR devices, which must be flushed with dry air and reach a spectral resolution of 2 cm^{-1}. The mesh in the laser setup was used to attenuate the laser intensity and the wedge sapphire window to reduce the laser intensity at the amide II band.[119] In the laser-based IR measurements, 91 scans were recorded and averaged with a measurement time of 45 s. Reference spectra were recorded and afterward sample spectra for 20 min, with a time interval of 20 s, lead to a total number of 60 scans. The samples were injected into two CaF_2 windows and an 8 μm thick spacer, as shown in Figure 11(a). The spectra were then treated with Savitzky–Golay (2nd order, window = 15 points) and if necessary, the water vapor in the atmosphere was corrected. In contrast, FITR measurements were conducted with a commercial device, where 341 spectra were averaged. Both devices have a spectral resolution of 3.6 cm^{-1}. The comparison between both measurements shows an excellent agreement between both. Even if the noise of the high-end FTIR device is a factor of 2 better compared to the laser, the SNR is by a factor

Encyclopedia of Analytical Chemistry, Online © 2006–2021 John Wiley & Sons, Ltd.
This article is © 2021 John Wiley & Sons, Ltd.
This article was published in the *Encyclopedia of Analytical Chemistry* in 2021 by John Wiley & Sons, Ltd.
DOI: 10.1002/9780470027318.a9751

of 1.5 better due to the longer path length (factor of 3 longer). A LOD by a factor of 15 compared to FTIR can be obtained with an optical path with a less noise of factor of 5.[126] With the same optical setup, but enlarging the optical path to 38 μm thick spacer between the two CaF_2 windows, the LOD was improved.[127] The data processing for the laser spectra was done, treated by Savitzky–Golay smoothing to reduce the instrumental noise. Afterward, a similarity index of each scan was conducted to sort out scans, which are shifted more than 0.1 cm^{-1}, and then, a low-pass Fourier Transform filter based on 4-term Blackman–Harris apodization (Fast Fourier Transformation, FFT) with a cutoff frequency of 150–200, was applied. To evaluate the comparability of the protein IR spectra, the degree between the spectral overlap of FTIR and QCL spectra was employed.[119] Data were also treated with correlation optimized warping (COW), whereby the scans of one measurement were aligned before they were averaged and the background and the sample single beam spectra were also aligned. COW is widely used to correct spectral or chromatographic shifts.[130] A schematics of the data treatment is depicted in Figure 11(b). Using an optical path length of 26 μm with the same EC-QCL as mentioned above, with a double-beam optical setup, robust sample handling was achieved. Therefore, the laser beam was divided into two beams, and guided into a custom-built two-path CaF_2 transmission flow cell, as shown in Figure 11(c). The spectra were treated with the same data processing above mentioned. Comparison to FTIR shows an approximately 8 times higher LOD compared to QCL.[120]

Another research field in medicine includes the breath gas diagnosis. Exhaled gas analysis is a noninvasive technique and allows a point-of-care disease, whereby the metabolic status can be recorded in (almost) real-time. Acetone in exhaled breath, for instance, is present in type I diabetes patients. Diabetes is an increasing disease in modern society. Blood-based diagnosis and monitoring are robust and reliable, but they are uncomfortable and invasive.[121] To obtain a cheap, fast, reliable, and accurate diagnosis, laser-based sensors can be the solution for breath gas analysis. For most of the biomarkers, the concentration range is between ppb_v and ppt_ν. Acetone is an easy molecule to be detected in the breath. To compare the breath gas analysis, blood glucose levels can be measured. To obtain the exact values of acetone and glucose, overnight fasting was done with all the patients. Acetone was measured with the laser-based setup shown in Figure 11(d). The obtained LOD of 0.05 ppt_ν was lower than the measured values of 0.39 until 1.09 ppt_ν of the healthy people, which is sufficient, to measure acetone in breath gas. This sensor can be used for the routine test in medical examinations to detect ketosis.[121] For comparison of measured gaseous acetone, FTIR can also be used. For the laser-based setup, the laser is focused onto the gas cell and a reference gas cell is used, as shown in Figure 11(e). Gaseous acetone, in HPLC quality, was measured with both QCL and FTIR, for comparison. Afterward, breath gas analysis with the laser-based sensor was conducted.[122]

Carbon monoxide is another marker that originates in the human body from the heme degradation. Two different setups were tested: the off-axis integrated cavity output spectroscopy (OA-ICOS) and the wavelength modulation 2f/1f spectroscopy (WMS). The used wavelength did not interfere with H_2O and CO_2, which is in a concentration of 2% and 5% present in exhaled gas.[123] The two different setups used are shown in Figure 11(f). In the first one, the laser beam was split for the WMS, whereby the laser beam was guided into an absorption gas cell with two ZnSe windows at Brewster angle to minimize the optical interferences and to maximize the transmission of the laser light. The other beam was focused on the reference cell. The second setup is the OA-ICOS, in which the laser beam was polarized and guided into the gas cell, where two optical mirrors built up the optical resonator. The LOD achieved with the WMS was 7.1 ppb_v and could be even improved until 2.1 ppb_v averaging the signal over 300 s. In contrast, the LOD reached with the OA-ICOS was 7 ppb_v and could be reduced to 0.89 ppb_v with an integration time of 128 s. Holding the breath for 10 s, the exhaled CO concentration increases by 20%, while the breath is collected in a bag.[123] CO can be also measured with IC lasers.

CO can be also a marker for being a smoker or no smoker. Exhaled breath CO (eCO) is a systematic heme metabolism, which is catalyzed by heme oxygenase enzymes in response to oxidative stress.[124] A typical mouth-eCo has a concentration of 1–3 ppm_ν in healthy persons. The concentration of eCO is different with smokers. The TDLAS setup consists of a laser, which is guided with a lens into a multipass cell with an effective absorption path length of almost 4 m and 51 reflections. Subsequently, the beam can be guided directly to the detector or through the FP interferometer and then to the detector, as shown in Figure 11(g). After the sensor was validated,[14] CO in alveolar breath of healthy nonsmokers showed no interference with water, via 2f-WMS modulation. After smoking, the CO concentration showed elevated levels, which could be measured real-time. [124]

$^{12}CO_2$ and $^{13}CO_2$ are known to be target isotopes for the detection of the *Heliobacter pyroli* infections.[125] The change in the isotopic ratio is observed by the administration of ^{13}C-enriched sugar and is related to the metabolization process. This sensor system is a portable

Encyclopedia of Analytical Chemistry, Online © 2006–2021 John Wiley & Sons, Ltd.
This article is © 2021 John Wiley & Sons, Ltd.
This article was published in the *Encyclopedia of Analytical Chemistry* in 2021 by John Wiley & Sons, Ltd.
DOI: 10.1002/9780470027318.a9751

sensor, whereby the ICL is focused on a dual-channel iHWG, serving as a sample chamber and reference cell. The implemented oxygen sensor detects oxygen in the gas through fluorescent oxygen quenching, as shown in Figure 11(h). After the sensor system was validated, real-time and in situ measurements of mouse breath gas were performed. To compare the obtained results from the laser-based system, the commercial measurement procedure of the GC/MS was used, whereby excellent agreement could be achieved. This sensor system is a compact portable device. [125]

5 SUMMARY

Infrared spectroscopy and sensing comprise well-established, nondestructive analytical techniques for the sensitive and selective determination and identification of chemical and biological compounds. Several light sources are available, whereby the family of cascade lasers provides distinct advantages including high output power and narrow bandwidth. In 1994, the QCL was experimentally demonstrated for the first time, while one year later the ICL has been introduced. Interband transitions characteristic of ICLs occur between electrons and holes in separated bands, whereas intersubband transitions are characteristic of QCLs, and occur between electrons and holes in confined states. Depending on the alignment of the energy bands, heterostructures of type I, type II, or type III/type II broken bandgap may be generated.

ICLs are generally based on a lattice structure of InAs/GaSb/AlSb III–V material, which is a typical type II broken bandgap design. By applying an electric field, the electric overlap between the conduction subband of an InAs electron quantum well (acceptor) and a valence subband of Ga(In)Sb hole quantum well (donor) can be tuned. The electron and hole injectors have to be designed to ensure population inversion, as well as a sufficient carrier transport through the structure. The GaSb valence band lies below the InAs conduction band, which ensures resonant tunneling into the InAs upper state. The blocking layer of GaInSb, AlSb, and GaSb suppresses current leakage such that a radiative transition into the lower state of InAs is needed followed by tunneling into the next junction region.

QCLs are designed as a unipolar semiconductor laser, which can operate either in pulsed or CW mode like ICLs. In contrast to ICLs, only electrons travel through the structure. QCL comprises a gain and an injection/relaxation region, which constitute the active region. As in the ICL, population inversion has to be ensured, and the structure must be electrically stable. The active area consists of a cascade structure with at least three states, and electrons are injected into the third state from the upper injector stage. Population inversion is achieved between state two and three, which is the lasing transition. The injector region can build up minibands, which prevents electrons from escaping. The injector/relaxation region in turn prevents the formation of electrical domains, i.e. the electrons are blocked from escaping and the applied electrical field is reduced. For a low threshold and high-efficiency QCL, the active region has to be optimized with possibly low waveguide losses, a narrow transition linewidth, and long upper state lifetime. Hence, the tunneling, the optical phonon scattering, the phase space, the escape time, and the injection efficiency must be optimized via the three-quantum-well active region, the two-phonon extraction, and the bound-to-continuum extraction. The optical waveguides should be designed to minimize internal losses and to maximize the required gain.

The main difference between both cascade laser concepts is that ICLs achieve population inversion due to the energy gaps of the employed material, a low current for reaching the transparency condition, and a maximum current limited by the device. QCLs achieve population inversion by the design of the active region, without transparency current, and the maximum current is obtained by doping the structure. Within ICLs, the photons are generated via optical transitions with Auger recombination, whereas in QCLs the intersubband transition is dominated by fast phonon scattering. QCLs exhibit TE polarized modes, whereas ICLs are characterized by TM polarized radiation output. To control the laser pulse time, the damped oscillator, Q-switching or mode-locking can be used in both cases. In QCLs, the emission wavelength may be chirped due to thermal heating within the laser structure during pulsed operation.

Wavelength tuning in a narrow spectral window may be achieved by either changing the temperature or the current. The cavity of the cascade lasers is usually designed as a Fabry–Perot cavity, a DFB resonator, or using an EC.

Last but not least, several examples of cascade lasers have been discussed, and a range of selected application examples are highlighted underlining the potential and utility of cascade laser-based analytical IR spectroscopic techniques.

ABBREVIATIONS AND ACRONYMS

CEAS	Cavity-enhanced Absorption Spectroscopy
COW	Correlation Optimized Warping
CW	Continuous Wave

This article was published in the *Encyclopedia of Analytical Chemistry* in 2021 by John Wiley & Sons, Ltd.
DOI: 10.1002/9780470027318.a9751

DFB	Distributed Feedback
DMF	Dimethylformamide
DSWG	Diamond Strip Waveguide
EC	External Cavity
eCO	exhaled Breath Co
FFT	Fast Fourier Transformation
FP-QCL	Fabry–Perot Qcl
FTIR	Fourier Transform Infrared
HRXRD	High-Resolution X-Ray Diffraction
iHWGs	Integrated Hollow Waveguides
IRAC	International Agency For Research On Cancer
IRE	Internal Reflection Element
LOD	Limit of Detection
MBE	Molecular Beam Epitaxy
MIR	Mid-Infrared Spectroscopy
MOF	Metal-Organic Framed
OA-ICOS	Off-Axis Integrated Cavity Output Spectroscopy
PECVD	Plasma Enhanced Vapor Deposition
ppb_v	Parts Per Billion By Volume
ppt	Parts Per Trillion
Q-factor	Quality Factor
QCLs, ICLs	Quantum Cascade And Interband Cascade Lasers
RIE	Reactive Ion Etching
SiC	Silicon Carbide
slpm	Standard Liters Per Minute
SNR	Signal-to-Noise Ratio
STM	Scanning Tunneling Microscope
TDLAS	Tuneable Diode Laser Absorption Spectroscopy
THz	Terahertz
TM	Transverse Magnetic
WMS	Wavelength Modulation 2F/1F Spectroscopy

RELATED ARTICLES

Biomedical Spectroscopy
Ultrashort Laser-pulse Medical Imaging

Environment: Trace Gas Monitoring
Cavity-Enhanced Spectroscopy: Applications, Theory and Instrumentation • Diode Laser Spectroscopic Monitoring of Trace Gases • Laser Absorption Spectroscopy, Air Monitoring by Tunable Mid-Infrared Diode • Laser-Based Combustion Diagnostics • Laser- and Optical-based Techniques for the Detection of Explosives • Laser-Induced Plasmas for Broadband Cavity-Enhanced Absorption Spectroscopy

Infrared Spectroscopy
Attenuated Total Reflection Fourier Transform Infrared Spectroscopy • Cavity Ringdown Laser Absorption Spectroscopy • Infrared Spectroscopy: Introduction• Infrared Sensors • Instrumentation and Applications of Cascade Laser Spectroscopy

REFERENCES

1. L. Hvozdara, N. Pennington, M. Kraft, M. Karlowatz, B. Mizaikoff, ‘Quantum Cascade Lasers for Mid-Infrared Spectroscopy’, *Vib. Spectrosc.*, **30**(1), 53–58 (2002). DOI: 10.1016/S0924-2031(02)00038-3
2. J. Haas, B. Mizaikoff, ‘Advances in Mid-Infrared Spectroscopy for Chemical Analysis’, *Annu. Rev. Anal. Chem.*, **9**, 45–68 (2016). DOI: 10.1146/annurev-anchem-071015-041507
3. T.G. Mayerhöfer, S. Pahlow, J. Popp, ‘Recent Technological and Scientific Developments Concerning the Use of Infrared Spectroscopy for Point-of-Care Applications’, *Spectrochim. Acta – Part A Mol. Biomol. Spectrosc. Elsevier B.V.*, **251**, 119411 (2021). DOI: 10.1016/j.saa.2020.119411
4. P.R. Griffiths, ‘Fourier Transform Infrared Spectrometry’, *Science*, **222**(4621), 297–302 (1983). DOI: 10.1126/science.6623077
5. J. Hecht, ‘Short History of Laser Development’, *SPIE Rev.*, **1**(1), 1–23 (2010). DOI: 10.1364/ao.49.000f99
6. N. Yu, F. Capasso, ‘Wavefront Engineering for Mid-Infrared and Terahertz Quantum Cascade Lasers’, *J. Opt. Soc. Am. B.*, **27**(11), B18 (2010). DOI: 10.1364/josab.27.000b18
7. C.E. Webb, *Handbook of Laser Technology and Applications*, 1st edition, CRC Press, Boca Raton, 2752, 2003.
8. E. Rosencher, B. Vinter, *Optoelectronics*, Cambridge University Press, Cambridge, 2002. DOI: 10.1017/CBO9780511754647
9. E. Rosencher, B. Vinter, *Optoelectronics* (P. Piva, Trans.), Cambridge University Press, Cambridge, 2002. DOI: 10.1017/CBO9780511754647
10. J. Faist, J. Faist, *Mode Control. Quantum Cascade Lasers*, Oxford University Press, Oxford, 168–198, 2013. DOI: 10.1093/acprof:oso/9780198528241.003.0010
11. J.H. Smet, C.G. Fonstad, Q. Hu, ‘Intrawell and Interwell Intersubband Transitions in Multiple Quantum Wells for Far-Infrared Sources’, *J. Appl. Phys.*, **79**(12), 9305–9320 (1996). DOI: 10.1063/1.362607
12. T.H. Maiman, ‘Stimulated Optical Radiation in Ruby’, *Nature*, **187**(4736), 493–494 (1960). DOI: 10.1038/187493a0
13. J. Faist, F. Capasso, D.L. Sivco, C. Sirtori, A.L. Hutchinson, A.Y. Cho, ‘Quantum Cascade

This article was published in the *Encyclopedia of Analytical Chemistry* in 2021 by John Wiley & Sons, Ltd.
DOI: 10.1002/9780470027318.a9751

Laser’, *Science*, **264**(5158), 553–556 (1994). DOI: 10.1126/science.264.5158.553

14. R.Q. Yang, ‘Infrared Laser Based on Intersubband Transitions in Quantum Wells’, *Superlattices Microstruct.*, **17**, 77–83 (1995). DOI: 10.1006/spmi.1995.1017
15. R.L. Byer, ‘Diode Laser-Pumped Solid-State Lasers’, *Science*, **239**(4841), 742–747 (1988). DOI: 10.1126/science.239.4841.742
16. A.S. Arnold, J.S. Wilson, M.G. Boshier, ‘A Simple Extended-Cavity Diode Laser’, *Rev. Sci. Instrum.*, **69**(3), 1236–1239 (1998). DOI: 10.1063/1.1148756
17. F. Capasso, ‘High-Performance Midinfrared Quantum Cascade Lasers’, *SPIE Rev.*, **1**(1), 1–9 (2010). DOI: 10.1117/1.3505844
18. I. Vurgaftman, W.W. Bewley, C.L. Canedy, C.S. Kim, M. Kim, C.D. Merritt, J. Abell, J.R. Lindle, J.R. Meyer, ‘Rebalancing of Internally Generated Carriers for Mid-Infrared Interband Cascade Lasers with Very Low Power Consumption’, *Nat. Commun.*, **2**(1), 1–7 (2011). DOI: 10.1038/ncomms1595
19. R.Q. Yang, ‘Interband Cascade Lasers Target the Mid-Infrared’, *Compound Semiconductor*, **25**(4), 48–53 (2019).
20. R.Q. Yang, *Interband Cascade (IC) Lasers. Semiconductor Lasers: Fundamentals and Applications* (eds. Alexei Baranov, Eric Tournié), Woodhead Publishing Limited, 487–513, 2013. DOI: 10.1533/9780857096401.3.487
21. J. Faist, *Quantum Devices. Quantum Cascade Lasers*, Oxford University Press, Oxford, 2013. DOI: 10.1093/acprof:oso/9780198528241.003.0001
22. J.R. Meyer, W.W. Bewley, C.L. Canedy, C.S. Kim, M. Kim, C.D. Merritt, I. Vurgaftman, ‘The Interband Cascade Laser’, *Photonics*, **7**(3), 75 (2020). DOI: 10.3390/PHOTONICS7030075
23. I. Vurgaftman, R. Weih, M. Kamp, J.R. Meyer, C.L. Canedy, C.S. Kim, M. Kim, W.W. Bewley, C.D. Merritt, J. Abell, S. Höfling, ‘Interband Cascade Lasers’, *J. Phys. D. Appl. Phys.*, **48**(12), 123001 (2015). DOI: 10.1088/0022-3727/48/12/123001
24. J. Röpcke, P.B. Davies, S. Hamann, M. Hannemann, N. Lang, J.P.H. van Helden, ‘Applying Quantum Cascade Laser Spectroscopy in Plasma Diagnostics’, *Photonics*, **3**, 45 (2016). DOI: 10.3390/photonics3030045
25. J. Faist, *Active Region Design. Quantum Cascade Lasers*, Oxford University Press, Oxford, 108–145, 2013. DOI: 10.1093/acprof:oso/9780198528241.003.0007
26. I. Vurgaftman, W.W. Bewley, C.L. Canedy, C.S. Kim, M. Kim, J.R. Lindle, C.D. Merritt, J. Abell, J.R. Meyer, ‘Mid-IR Type-II Interband Cascade Lasers’, *IEEE J. Sel. Top. Quantum Electron.*, **17**(5), 1435–1444 (2011). DOI: 10.1109/JSTQE.2011.2114331
27. I. Vurgaftman, W.W. Bewley, C.L. Canedy, C.S. Kim, M. Kim, C.D. Merritt, J. Abell, J.R. Meyer, ‘Interband Cascade Lasers with Low Threshold Powers and High Output Powers’, *IEEE J. Sel. Top. Quantum Electron.*, **19**(4), 1200210 (2013). DOI: 10.1109/JSTQE.2012.2237017
28. J.P. Van Der Ziel, W.T. Tsang, ‘Integrated Multilayer GaAs Lasers Separated by Tunnel Junctions’, *Appl. Phys. Lett.*, **41**(6), 499, 10.1063/1.93585–501 (1982).
29. R.F. Kazarinov, R.A. Suris, ‘Electric and Electromagnetic Properties of Semiconductors with a Superlattice’, *Sov. Phys. Semicond.*, **6**(1), 120–131 (1972).
30. Y. Bai, S. Slivken, S. Kuboya, S.R. Darvish, M. Razeghi, ‘Quantum Cascade Lasers that Emit More Light than Heat’, *Nat. Photonics. Nat. Publish. Group*, **4**(2), 99–102 (2010). DOI: 10.1038/nphoton.2009.263
31. W. Hu, J. Yang, ‘Two-Dimensional Van Der Waals Heterojunctions for Functional Materials and Devices’, *J. Mater. Chem. C. Royal Soc. Chem.*, **5**(47), 12289–12297 (2017). DOI: 10.1039/c7tc04697a
32. G.G. Zegrya, A.D. Andreev, ‘Mechanism of Suppression of Auger Recombination Processes in Type-II Heterostructures’, *Appl. Phys. Lett.*, **67**(June 1998), 2681 (1995). DOI: 10.1063/1.114291
33. J.C. Banthí-Barcenas, F. Sutara, and I. Hernández-Calderón, Design of a Quantum Well Based on a ZnCdSe/ZnTe Type II Heterostructure Confined Type I Within ZnSe Barriers, AIP Conference Proceedings, 2018, February 1934, 030001. 10.1063/1.5024488.
34. P.A. Alvi, ‘Transformation of Type-II InAs/AlSb Nanoscale Heterostructure into Type-I Structure and Improving Interband Optical Gain’, *Phys. Status Solidi Basic Res.*, **254**(5), 1600572 (2017). DOI: 10.1002/pssb.201600572
35. R.Q. Yang, J.M. Xu, ‘Population Inversion Through Resonant Interband Tunneling’, *Appl. Phys. Lett.*, **59**(2), 181–182 (1991). DOI: 10.1063/1.105987
36. P.M. Grant, J.P. Sage, ‘A Comparison of Neural Network and Matched Filter Processing for Detecting Lines in Images’, *J. Appl. Phys.*, **8197**(79), 194–199 (2008). DOI: 10.1063/1.36255
37. K.J. Vahala, C.E. Zah. “Effect of Doping on the Optical Gain and the Spontaneous Noise Enhancement Factor in Quantum Well Amplifiers and Lasers Studied by Simple Analytical Expressions”. *Appl. Phys. Lett.* 1988. **52**(23): 1945–1947. 10.1063/1.99584.
38. W.W. Bewley, J.R. Lindle, C.S. Kim, M. Kim, C.L. Canedy, I. Vurgaftman, J.R. Meyer, ‘Lifetimes and Auger Coefficients in Type-II W Interband Cascade Lasers’, *Appl. Phys. Lett.*, **93**(4), 1–4 (2008). DOI: 10.1063/1.2967730
39. S.G. Rykovanov, C.G.R. Geddes, C.B. Schroeder, E. Esarey, W.P. Leemans, ‘Controlling the Spectral Shape of Nonlinear Thomson Scattering with Proper Laser

This article was published in the *Encyclopedia of Analytical Chemistry* in 2021 by John Wiley & Sons, Ltd.
DOI: 10.1002/9780470027318.a9751

Chirping', *Phys. Rev. Accel. Beams*, **19**(3), 1–9 (2016). DOI: 10.1103/PhysRevAccelBeams.19.030701

40. R.Q. Yang, L. Li, W. Huang, S. Member, S.M.S. Rassel, J.A. Gupta, A. Bezinger, X. Wu, S.G. Razavipour, G.C. Aers, 'InAs-Based Interband Cascade Lasers', *IEEE J. Sel. Top. Quantum Electron.*, **25**(6), 1, 10.1109/JSTQE.2019.2916923–8 (2019).
41. J. Faist, *Optical Transitions. Quantum Cascade Lasers*, Oxford University Press, Oxford, 48–66, 2013. DOI: 10.1093/acprof:oso/9780198528241.003.0004
42. J. Faist, *Mid-Infrared Waveguides. Quantum Cascade Lasers*, Oxford University Press, Oxford, 91–107, 2013. DOI: 10.1093/acprof:oso/9780198528241.003.0006
43. J.S. Li, B. Yu, H. Fischer, W. Chen, A.P. Yalin, 'Contributed Review: Quantum Cascade Laser Based Photoacoustic Detection of Explosives', *Rev. Sci. Instrum.*, **86**(3), 031501 (2015). DOI: 10.1063/1.4916105
44. S. Schilt, L. Tombez, G. Di Domenico, D. Hofstetter, 'Frequency Noise and Linewidth of Mid-Infrared Continuous- Wave Quantum Cascade Lasers: An Overview', *Wonder Nanotechnol. Quantum Optoelectron. Devices Appl.*, **(chapter 12**, 261–287 (2013). DOI: 10.1117/3.1002245.Ch12
45. J. Faist, *Technology. Quantum Cascade Lasers*, Oxford University Press, Oxford, 2013. DOI: 10.1093/acprof:oso/9780198528241.003.0002
46. F. Wang, S. Slivken, D.H. Wu, M. Razeghi, 'Room Temperature Quantum Cascade Laser With 31% Wall-Plug Efficiency', *AIP Adv.*, **075012**(June), 10–14 (2020). DOI: 10.1063/5.0012925
47. C.L. Canedy, W.W. Bewley, J.R. Lindle, C.S. Kim, I. Vurgaftman, I.V.M. Kim, J.R. Meyer, 'High-Power and High-Efficiency Midwave- Infrared Interband Cascade Lasers', *Appl. Phys. Lett.*, **161103**(88), 161103 (2006). DOI: 10.1063/1.2195778
48. Y. Bai, N. Bandyopadhyay, S. Tsao, S. Slivken, M. Razeghi, 'Room Temperature Quantum Cascade Lasers with 27% Wall Plug Efficiency', *Appl. Phys. Lett.*, **98**(18), 181102 (2011). DOI: 10.1063/1.3586773
49. J. Faist, *Intersubband Scattering Processes. Quantum Cascade Lasers*, Oxford University Press, Oxford, 2013. DOI: 10.1093/acprof:oso/9780198528241.003.0005
50. R. Ferreira, G. Bastard, 'Evaluation of Some Scattering Times for Electrons in Unbiased and Biased Single- and Multiple-Quantum-Well Structures', *Phys. Rev. B*, **40**(2), 1074–1086 (1989). DOI: 10.1103/PhysRevB.40.1074
51. P.J. Price, 'Two-Dimensional Electron Transport in Semiconductor Layers. I. Phonon Scattering', *Ann. Phys. (N. Y.)*, **133**(2), 217–239 (1981). DOI: 10.1016/0003-4916(81)90250-5
52. J. Faist, F. Capasso, C. Sirtori, D.L. Sivco, A.L. Hutchinson, A.Y. Cho, 'Vertical Transition Quantum Cascade Laser with Bragg Confined Excited State', *Appl. Phys. Lett.*, **66**(5), 538 (1995). DOI: 10.1063/1.114005
53. M. Beck, D. Hofstetter, T. Aellen, J. Faist, U. Oesterle, M. Ilegems, E. Gini, H. Melchior, 'Continuous Wave Operation of a Mid-Infrared Semiconductor Laser at Room Temperature', *Science*, **295**(5553), 301–305 (2002). DOI: 10.1126/science.1066408
54. A. Schwaighofer, M. Brandstetter, B. Lendl, 'Quantum Cascade Lasers (QCLs) in Biomedical Spectroscopy His Work Focuses on Applying', *Chem. Soc. Rev. Royal Soc. Chem.*, **46**(5903), 5903–5924 (2017). DOI: 10.1039/c7cs00403f
55. A. Tredicucci, F. Capasso, C. Gmachl, D.L. Sivco, A.L. Hutchinson, A.Y. Cho, 'High Performance Interminiband Quantum Cascade Lasers with Graded Superlattices', *Appl. Phys. Lett.*, **73**(15), 2101–2103 (1998). DOI: 10.1063/1.122391
56. M. Troccoli, G. Scamarcio, V. Spagnolo, A. Tredicucci, C. Gmachl, F. Capasso, D.L. Sivco, A.Y. Cho, M. Striccoli, 'Electronic Distribution in Superlattice Quantum Cascade Lasers', *Appl. Phys. Lett.*, **77**(8), 1088–1090 (2000). DOI: 10.1063/1.1289798
57. P. Kruck, H. Page, C. Sirtori, S. Barbieri, M. Stellmacher, J. Nagle, 'Improved Temperature Performance of Al0.33Ga0.67As/GaAs Quantum-Cascade Lasers with Emission Wavelength at λ≈11 μm', *Appl. Phys. Lett.*, **76**(23), 3340–3342 (2000). DOI: 10.1063/1.126686
58. S.A. Goudsmit, 'Physical Review Letters: Editorial', *Phys. Rev. Lett.*, **5**(6), 233 (1960). DOI: 10.1103/PhysRevLett.5.233
59. G. Bastard, 'Theoretical Investigations of Superlattice Band Structure in the Envelope-Function Approximation', *Phys. Rev. B*, **25**(12), 219–232 (1982). DOI: 10.1680/ftcams.35423.0034
60. M.E. Flatté, C.H. Grein, H. Ehrenreich, R.H. Miles, H. Cruz, 'Theoretical Performance Limits of 2.1–4.1 μm InAs/InGaSb, HgCdTe, and InGaAsSb Lasers', *J. Appl. Phys.*, **4552**(78), 4552–4559 (1995). DOI: 10.1063/1.359798
61. N.F. Johnson, H. Ehrenreich, P.M. Hui, P.M. Young, 'Electronic and Optical Properties of III–V and II–VI Semiconductor Superlattices', *Phys. Rev. B*, **41**(6), 3655–3669 (1990). DOI: 10.1103/PhysRevB.41.3655
62. N.F. Johnson, H. Ehrenreich, G.Y. Wu, 'Superlattice k p Models for Calculating Electronic Structure', *Phys. Rev. B*, **38**(18), 13095 (1988). DOI: 10.1103/PhysRevB.38.13095
63. N. Yu, R. Blanchard, J. Fan, Q.J. Wang, C. Pflügl, L. Diehl, T. Edamura, M. Yamanishi, H. Kan, F. Capasso, 'Quantum Cascade Lasers with Integrated Plasmonic Antenna-Array Collimators', *Opt. Express*, **16**(24), 19447–19461 (2008). DOI: 10.1364/OE.16.019447

This article was published in the *Encyclopedia of Analytical Chemistry* in 2021 by John Wiley & Sons, Ltd.
DOI: 10.1002/9780470027318.a9751

64. C. Sirtori, P. Kruck, S. Barbieri, H. Page, J. Nagle, M. Beck, J. Faist, U. Oesterle, 'Low-Loss Al-Free Waveguides for Unipolar Semiconductor Lasers', *Appl. Phys. Lett.*, **75**(25), 3911–3913 (1999). DOI: 10.1063/1.125491
65. J. Devenson, D. Barate, O. Cathabard, R. Teissier, A.N. Baranov, 'Very Short Wavelength (λ = 3.1–3.3 μm) Quantum Cascade Lasers', *Appl. Phys. Lett.*, **89**(19), 191115 (2006). DOI: 10.1063/1.2387473
66. C. Gmachl, A. Tredicucci, F. Capasso, A.L. Hutchinson, D.L. Sivco, J.N. Baillargeon, A.Y. Cho, 'High-Power λ ≈ 8 μm Quantum Cascade Lasers with Near Optimum Performance', *Appl. Phys. Lett.*, **72**(24), 3130–3132 (1998). DOI: 10.1063/1.121569
67. A. Bismuto, T. Gresch, A. Bächle, J. Faist, 'Large Cavity Quantum Cascade Lasers with InP Interstacks', *Appl. Phys. Lett.*, **93**(23), 231104 (2008). DOI: 10.1063/1.3042213
68. S. Welzel, R. Engeln, J. Röpcke, 'Quantum Cascade Laser Based Chemical Sensing Using Optically Resonant Cavities', in *Cavity-Enhanced Spectroscopy and Sensing* (eds. Gianluca GagliardiHans-Peter Loock), Springer, Berlin, Heidelberg, 93–142, Vol. **179**, 2014. DOI: 10.1007/978-3-642-40003-2_3
69. J. Faist, C. Gmachl, F. Capasso, C. Sirtori, D.L. Sivco, J.N. Baillargeon, A.Y. Cho, 'Distributed Feedback Quantum Cascade Lasers', *Appl. Phys. Lett.*, **70**(20), 2670–2672 (1997). DOI: 10.1063/1.1661499
70. W. Zeller, L. Naehle, P. Fuchs, F. Gerschuetz, L. Hildebrandt, J. Koeth, 'DFB Lasers Between 760 nm and 16 μm for Sensing Applications', *Sensors*, **10**(4), 2492–2510 (2010). DOI: 10.3390/s100402492
71. A. Lambrecht, M. Pfeifer, W. Konz, J. Herbst, F. Axtmann, 'Broadband Spectroscopy with External Cavity Quantum Cascade Lasers Beyond Conventional Absorption Measurements', *Analyst*, **139**(9), 2070–2078 (2014). DOI: 10.1039/c3an01457f
72. M. Von Edlinger, R. Weih, J. Scheuermann, L. Nähle, M. Fischer, J. Koeth, M. Kamp, S. Höfling, 'Monolithic Single Mode Interband Cascade Lasers With Wide Wavelength Tunability', *Appl. Phys. Lett.*, **109**(20), 201109 (2016). DOI: 10.1063/1.4968535
73. M. Von Edlinger, J. Scheuermann, R. Weih, L. Nähle, M. Fischer, J. Koeth, M. Kamp, 'Widely-Tunable Interband Cascade Lasers for the Mid-Infrared', *Proc. SPIE*, **9370**, 1–7 (2015). DOI: 10.1117/12.2079926
74. C. Sirtori, J. Faist, F. Capasso, D.L. Sivco, A.L. Hutchinson, A.Y. Cho, 'Quantum Cascade Laser With Plasmon-Enhanced Waveguide Operating at 8.4 μm Wavelength', *Appl. Phys. Lett.*, **66**(24), 3242–3244 (1995). DOI: 10.1063/1.113391
75. M.W. Fleming, A. Mooradian, 'Spectral Characteristics of External-Cavity Controlled Semiconductor Lasers', *IEEE J. Quantum Electron.*, **17**(1), 44–59 (1981).
76. C. Young, R. Cendejas, S.S. Howard, W. Sanchez-Vaynshteyn, A.J. Hoffman, K.J. Franz, Y. Yao, B. Mizaikoff, X. Wang, J. Fan, C.F. Gmachl, 'Wavelength Selection for Quantum Cascade Lasers by Cavity Length', *Appl. Phys. Lett.*, **94**(091109), 10–13 (2009). DOI: 10.1063/1.3093422
77. S. Chin, V. Mitev, E. Giraud, R. Maulini, S. Blaser, D.L. Boiko, 'Electrically Driven Frequency Blue-Chirped Emission in Fabry-Perot Cavity Quantum Cascade Laser at Room Temperature', *Appl. Phys. Lett.*, **118**(2), 021108 (2021). DOI: 10.1063/5.0033030
78. M.G. Littman, H.J. Metcalf, 'Spectrally Narrow Pulsed Dye Laser Without Beam Expander', *Appl. Opt.*, **17**(14), 2224 (1978). DOI: 10.1364/ao.17.002224
79. K.K. Law, Monolithic QCL Design Approaches for Improved Reliability and Affordability, Naval Air Warfare Center Weapons Division (United States), 8993, 1–7, 2014. 10.1117/12.2047371.
80. M. Troccoli, C. Gmachl, F. Capasso, D.L. Sivco, A.Y. Cho, 'Mid-Infrared (λ ≈ 7.4 μm) Quantum Cascade Laser Amplifier for High Power Single-Mode Emission and Improved Beam Quality', *Appl. Phys. Lett.*, **80**(22), 4103–4105 (2002). DOI: 10.1063/1.1479453
81. C. Sirtori, S. Peter Kruck, T. Barbieri, P. Collot, J. Nagle, M. Beck, J. Faist, U. Oesterle, '$GaAs/Al_xGa_{1-x}As$ Quantum Cascade Laser', *Appl. Phys. Lett.*, **73**(24), 3486–3488 (1998). DOI: 10.1063/1.122812
82. Y. Deng, B. Zhao, X. Wang, C. Wang, 'Narrow Linewidth Characteristics of Interband Cascade Lasers', *Appl. Phys. Lett.*, **116**(20), 201101 (2020). DOI: 10.1063/5.0006823
83. L.A. Sterczewski, C.F.M. Bagheri, C.L. Canedy, I. Vurgaftman, J.R. Meyer, 'Mid-Infrared Dual-Comb Spectroscopy with Cascade Lasers and Detectors', *Appl. Phys. Lett.*, **116**(14), 141102 (2020). DOI: 10.1063/1.5143954
84. L.A. Sterczewski, J. Westberg, M. Bagheri, C. Frez, I. Vurgaftman, C.L. Canedy, W.W. Bewley, C.D. Merritt, C.S. Kim, M. Kim, J.R. Meyer, G. Wysocki, 'Mid-Infrared Dual-Comb Spectroscopy with Interband Cascade Lasers', *Opt. Lett.*, **44**(8), 2113 (2019). DOI: 10.1364/ol.44.002113
85. W.W. Bewley, C.L. Canedy, C.S. Kim, M. Kim, C.D. Merritt, J. Abell, I. Vurgaftman, J.R. Meyer, 'Continuous-Wave Interband Cascade Lasers Operating Above Room Temperature at λ = 47–56 μm', *Opt. Express*, **20**(3), 3235 (2012). DOI: 10.1364/oe.20.003235
86. H. Knötig, B. Hinkov, R. Weih, S. Höfling, J. Koeth, G. Strasser, 'Continuous-Wave Operation of Vertically Emitting Ring Interband Cascade Lasers at Room Temperature', *Appl. Phys. Lett.*, **116**(13), 131101 (2020). DOI: 10.1063/1.5139649
87. S. Höfling, R. Weih, M. Dallner, J. Scheuermann, M. von Edlinger, L. Nähle, M. Fischer, J. Koeth, M. Kamp, 'Mid-Infrared (~2.8 μm to ~7.1 μm) Interband Cascade

This article was published in the *Encyclopedia of Analytical Chemistry* in 2021 by John Wiley & Sons, Ltd.
DOI: 10.1002/9780470027318.a9751

Lasers', *Biosens. Nanomed. VIII*, **9550**, 95500F (2015). DOI: 10.1117/12.2193657

88. J. Hillbrand, M. Beiser, A.M. Andrews, H. Detz, R. Weih, A. Schade, S. Höfling, G. Strasser, B. Schwarz, 'Picosecond Pulses From a Mid-Infrared Interband Cascade Laser', *arXiv*, **6**(10), 8–11 (2019). DOI: 10.1364/optica.6.001334
89. M. Rochat, J. Faist, M. Beck, U. Oesterle, M. Ilegems, 'Far-Infrared ($\lambda = 88$ μm) Electroluminescence in a Quantum Cascade Structure', *Appl. Phys. Lett.*, **73**(25), 3724–3726 (1998). DOI: 10.1063/1.122895
90. C. Deutsch, H. Detz, T. Zederbauer, M. Krall, M. Brandstetter, A.M. Andrews, P. Klang, W. Schrenk, G. Strasser, K. Unterrainer, 'InGaAs/GaAsSb/InP Terahertz Quantum Cascade Lasers', *J. Infrared, Millimeter, Terahertz Waves*, **34**(5–6), 374–385 (2013). DOI: 10.1007/s10762-013-9991-5
91. J.B. Khurgin, 'Analytical Expression for the Width of Quantum Cascade Laser Frequency Comb Analytical Expression for the Width of Quantum Cascade Laser Frequency Comb', *Appl. Phys. Lett.*, **117**(16), 161104 (2020). DOI: 10.1063/5.0029588
92. R. Wang, P. Täschler, F. Kapsalidis, M.B. Mehran Shahmohammadi, J. Faist, 'Mid-Infrared Quantum Cascade Laser Frequency Combs Based on Multi-Section Waveguides', *Opt. Lett.*, **45**(23), 6462–6465 (2020). DOI: 10.1364/OL.411027
93. A. Hugi, G. Villares, S. Blaser, H.C. Liu, J. Faist, 'Mid-Infrared Frequency Comb Based on a Quantum Cascade Laser', *Nature*, **492**, 1–3 (2012). DOI: 10.1038/nature11620
94. S. Hakobyan, R. Maulini, S. Blaser, T. Gresch, A. Muller, 'High Performance Quantum Cascade Laser Frequency Combs at $\lambda \sim 6$ μm Based on Plasmon-Enhanced Dispersion Compensation', *Opt. Express*, **28**(14), 20714–20727 (2020). DOI: 10.1364/OE.395260
95. K. Gallacher, M. Ortolani, K. Rew, C. Ciano, L. Baldassarre, M. Virgilio, G. Scalari, J. Faist, L. Di Gaspare, M. De Seta, G. Capellini, 'Design and Simulation of Losses in Ge/SiGe Terahertz Quantum Cascade Laser Waveguides', *Opt. Express*, **28**(4), 4786–4800 (2020). DOI: 10.1364/OE.384993
96. C. Young, S.S. Kim, Y. Luzinova, M. Weida, D. Arnone, E. Takeuchi, T. Day, B. Mizaikoff, 'External Cavity Widely Tunable Quantum Cascade Laser Based Hollow Waveguide Gas Sensors for Multianalyte Detection', *Sensors Actuators, B Chem.*, **140**(1), 24–28 (2009). DOI: 10.1016/j.snb.2009.03.023
97. C.L. Strand, Y. Ding, S.E. Johnson, R.K. Hanson, 'Measurement of the Mid-Infrared Absorption Spectra of Ethylene (C_2H_4) and Other Molecules at High Temperatures and Pressures', *J. Quant. Spectrosc. Radiat. Transf.*, **222–223**, 122–129 (2019). DOI: 10.1016/j.jqsrt.2018.10.030
98. J. Jágerská, B. Tuzson, H. Looser, A. Bismuto, J. Faist, H. Prinz, L. Emmenegger, 'Highly Sensitive and Fast Detection of Propane-Butane Using a 3 μm Quantum Cascade Laser', *Appl. Opt.*, **52**(19), 4613–4619 (2013). DOI: 10.1364/AO.52.004613
99. J. Jágerská, P. Jouy, B. Tuzson, H. Looser, M. Mangold, P. Soltic, A. Hugi, R. Brönnimann, J. Faist, L. Emmenegger, 'Simultaneous Measurement of NO and NO_2 by Dual-Wavelength Quantum Cascade Laser Spectroscopy', *Opt. Express*, **23**(2), 1512 (2015). DOI: 10.1364/oe.23.001512
100. A. Genner, P. Martín-mateos, H. Moser, B. Lendl, 'A Quantum Cascade Laser-Based Multi-Gas Sensor for Ambient Air Monitoring', *Sensors (Switzerland)*, **20**(7), 528–535 (2020). DOI: 10.3390/s20071850
101. J. Li, H. Deng, J. Sun, B. Yu, H. Fischer, 'Simultaneous Atmospheric CO, N_2O and H_2O Detection Using a Single Quantum Cascade Laser Sensor Based on Dual-Spectroscopy Techniques', *Sensors Actuators, B Chem.*, **231**, 723–732 (2016). DOI: 10.1016/j.snb.2016.03.089
102. L. Dong, F.K. Tittel, C. Li, N.P. Sanchez, H. Wu, C. Zheng, Y. Yu, A. Sampaolo, R.J. Griffin, 'Compact TDLAS Based Sensor Design Using Interband Cascade Lasers for Mid-IR Trace Gas Sensing', *Opt. Express*, **24**(6), 528–535 (2016). DOI: 10.1364/OE.24.00A528
103. C. Li, L. Dong, C. Zheng, F.K. Tittel, 'Compact TDLAS Based Optical Sensor for ppb-Level Ethane Detection by Use of a 3.34 μm Room-Temperature CW Interband Cascade Laser', *Sensors Actuators, B Chem.*, **232**, 188–194 (2016). DOI: 10.1016/j.snb.2016.03.141
104. E. Tütüncü, M. Nägele, P. Fuchs, M. Fischer, B. Mizaikoff, 'IHWG-ICL: Methane Sensing with Substrate-Integrated Hollow Waveguides Directly Coupled to Interband Cascade Lasers', *ACS Sensors*, **1**(7), 847–851 (2016). DOI: 10.1021/acssensors.6b00238
105. Q. He, C. Zheng, M. Lou, W. Ye, Y. Wang, F.K. Tittel, 'Dual-Feedback Mid-Infrared Cavity-Enhanced Absorption Spectroscopy for H_2CO Detection Using a Radio-Frequency Electrically-Modulated Interband Cascade Laser', *Opt. Express*, **26**(12), 4436–4443 (2018).
106. S. Lundqvist, P. Kluczynski, R. Weih, M. Von Edlinger, L. Nähle, M. Fischer, A. Bauer, S. Höfling, J. Koeth, 'Sensing of Formaldehyde Using a Distributed Feedback Interband Cascade Laser Emitting Around 3493 nm', *Appl. Opt.*, **51**(25), 6009–6013 (2012). DOI: 10.1364/AO.51.006009
107. C. Yao, Z. Wang, Q. Wang, Y. Bian, C. Chen, L. Zhang, W. Ren, 'Interband Cascade Laser Absorption Sensor for Real-Time Monitoring of Formaldehyde Filtration by a Nanofiber Membrane', *Appl. Opt.*, **57**(27), 8005–8010 (2018). DOI: 10.1364/ao.57.008005
108. J.A. Nwaboh, Z. Qu, O. Werhahn, V. Ebert, 'Interband Cascade Laser-Based Optical Transfer Standard for Atmospheric Carbon Monoxide Measurements', *Appl. Opt.*, **56**(11), 84–93 (2017).

This article was published in the *Encyclopedia of Analytical Chemistry* in 2021 by John Wiley & Sons, Ltd.
DOI: 10.1002/9780470027318.a9751

109. G. Ramer, J. Kasberger, M. Brandstetter, A. Saeed, B. Jakoby, B. Lendl, 'A Broadband Grating-Coupled Silicon Nitride Waveguide for the Mid-IR: Characterization and Sensitive Measurements Using an External Cavity Quantum Cascade Laser', *Appl. Phys. B Lasers Opt.*, **116**(2), 325–332 (2014). DOI: 10.1007/s00340-013-5695-8

110. C. Charlton, M. Giovannini, J. Faist, B. Mizaikoff, 'Fabrication and Characterization of Molecular Beam Epitaxy Grown Thin-Film GaAs Waveguides for Mid-Infrared Evanescent Field Chemical Sensing', *Anal. Chem.*, **78**(12), 4224–4227 (2006). DOI: 10.1021/ac052214a

111. M. Sieger, J. Haas, M. Jetter, P. Michler, M. Godejohann, B. Mizaikof, 'Mid-Infrared Spectroscopy Platform Based on GaAs/AlGaAs Thin-Film Waveguides and Quantum Cascade Lasers', *Anal. Chem. Anal. Chem.*, **213**(5), 2558–2562 (2016). DOI: 10.1021/acs.analchem.5b04144

112. X. Wang, M. Karlsson, P. Forsberg, M. Sieger, F. Nikolajeff, L. Österlund, B. Mizaikoff, 'Diamonds are a Spectroscopists Best Friend: Thin-Film Diamond Mid-Infrared Waveguides for Advanced Chemical Sensors/Biosensors', *Anal. Chem.*, **86**(16), 8136–8141 (2014). DOI: 10.1021/ac5011475

113. J. Haas, E.V. Catalán, P. Piron, F. Nikolajeff, L. Österlund, M. Karlsson, B. Mizaikoff, 'Polycrystalline Diamond Thin-Film Waveguides for Mid-Infrared Evanescent Field Sensors', *ACS Omega*, **3**(6), 6190–6198 (2018). DOI: 10.1021/acsomega.8b00623

114. A.I. Lopez-Lorente, P. Wang, M. Sieger, E.V. Catalan, M. Karlsson, F. Nikolajeff, L. Österlund, B. Mizaikoff, 'Mid-Infrared Thin-Film Diamond Waveguides Combined with Tunable Quantum Cascade Lasers for Analyzing the Secondary Structure of Proteins', *Phys. Status Solidi.*, **2123**(8), 2117–2123 (2016). DOI: 10.1002/pssa.201600134

115. I.L. Jernelv, J. Høvik, D.R. Hjelme, A. Aksnes, Signal Enhancement in Microstructured Silicon Attenuated Total Reflection Elements for Quantum Cascade Laser-Based Spectroscopy, Proceedings of SPIE, Biomedical Spectroscopy, Microscopy, and Imaging, 113590A, 1–8, 2020. 10.1117/12.2554528.

116. X. Wang, S.S. Kim, R. Roßbach, M. Jetter, P. Michler, B. Mizaikoff, 'Ultra-Sensitive Mid-Infrared Evanescent Field Sensors Combining Thin-Film Strip Waveguides with Quantum Cascade Lasers', *Analyst*, **137**(10), 2322–2327 (2012). DOI: 10.1039/c1an15787f

117. P. Piron, E. Vargas Catalan, F. Nikolajeff, L. Österlund, P.O. Andersson, J. Bergström, B. Mizaikoff, M. Karlsson, 'Development of a Diamond Waveguide Sensor for Sensitive Protein Analysis Using IR Quantum Cascade Lasers', *Proc. SPIE*, **10539**, 105390F (2018). DOI: 10.1117/12.2289844

118. J. Haas, E.V. Catalán, P. Piron, M. Karlsson, B. Mizaikoff, 'Infrared Spectroscopy Based on Broadly Tunable Quantum Cascade Lasers and Polycrystalline Diamond Waveguides', *Analyst. R. Soc. Chem.*, **143**(21), 5112–5119 (2018). DOI: 10.1039/c8an00919h

119. A. Schwaighofer, M. Montemurro, S. Freitag, C. Kristament, M.J. Culzoni, B. Lendl, 'Beyond Fourier Transform Infrared Spectroscopy: External Cavity Quantum Cascade Laser-Based Mid-infrared Transmission Spectroscopy of Proteins in the Amide i and Amide II Region', *Anal. Chem.*, **90**(11), 7072–7079 (2018). DOI: 10.1021/acs.analchem.8b01632

120. C.K. Akhgar, G. Ramer, M. Żbik, A. Trajnerowicz, J. Pawluczyk, A. Schwaighofer, B. Lendl, 'The Next Generation of IR Spectroscopy: EC-QCL-Based Mid-IR Transmission Spectroscopy of Proteins with Balanced Detection', *Anal. Chem.*, **92**(14), 9901–9907 (2020). DOI: 10.1021/acs.analchem.0c01406

121. A. Reyes-Reyes, R.C. Horsten, H.P. Urbach, N. Bhattacharya, 'Study of the Exhaled Acetone in Type 1 Diabetes Using Quantum Cascade Laser Spectroscopy', *Anal. Chem.*, **87**, 507–512 (2015). DOI: 10.1021/ac504235e

122. L. Ciaffoni, G. Hancock, J.J. Harrison, J.P.H. Van Helden, C.E. Langley, R. Peverall, G.A. Ritchie, S. Wood, 'Demonstration of a Mid-Infrared Cavity Enhanced Absorption Spectrometer for Breath Acetone Detection', *Anal. Chem.*, **85**(2), 846–850 (2013). DOI: 10.1021/ac3031465

123. N. Pakmanesh, S.M. Cristescu, A. Ghorbanzadeh, F.J.M. Harren, J. Mandon, 'Quantum Cascade Laser – Based Sensors for the Detection of Exhaled Carbon Monoxide', *Appl. Phys. B*, **122**(10), 1–9 (2016). DOI: 10.1007/s00340-015-6294-7

124. R. Ghorbani, F.M. Schmidt, 'ICL-Based TDLAS Sensor for Real-Time Breath Gas Analysis of Carbon Monoxide Isotopes', *Opt. Express*, **25**(11), 12743–12752 (2017).

125. E. Tütüncü, M. Nägele, S. Becker, M. Fischer, J. Koeth, C. Wolf, Köstler S, Ribitsch V, Teuber A, Gröger M, Kress S "Advanced Photonic Sensors Based on Interband Cascade Lasers for Real-Time Mouse Breath Analysis". *ACS Sensors* 2018. **3**(9): 1743–1749. 10.1021/acssensors.8b00477.

126. A. Schwaighofer, C.K. Akhgar, B. Lendl, 'Broadband Laser-Based Mid-IR Spectroscopy for Analysis of Proteins and Monitoring of Enzyme Activity', *Spectrochim. Acta Part A Mol. Biomol. Spectrosc.*, **253**, 119563 (2021). DOI: 10.1016/j.saa.2021.119563

127. M. Montemurro, A. Schwaighofer, A. Schmidt, M.J. Culzoni, H.K. Mayer, B. Lendl, 'High-Throughput Quantitation of Bovine Milk Proteins and Discrimination of Commercial Milk Types by External Cavity-Quantum Cascade Laser Spectroscopy and Chemometrics', *Analyst. R. Soc. Chem.*, **144**(18), 5571–5579 (2019). DOI: 10.1039/c9an00746f

128. M. Kölhed, M. Haberkorn, V. Pustogov, B. Mizaikoff, J. Frank, B. Karlberg, B. Lendl, 'Assessment of Quantum Cascade Lasers as Mid Infrared Light

This article was published in the *Encyclopedia of Analytical Chemistry* in 2021 by John Wiley & Sons, Ltd.
DOI: 10.1002/9780470027318.a9751

Sources for Measurement of Aqueous Samples', *Vib. Spectrosc.*, **29**(1–2), 283–289 (2002). DOI: 10.1016/S0924-2031(01)00190-4

129. B. Mizaikoff, 'Waveguide-Enhanced Mid-Infrared Chem/Bio Sensors', *Chem. Soc. Rev.*, **42**(22), 8683–8699 (2013). DOI: 10.1039/c3cs60173k

130. M.R. Alcaráz, A. Schwaighofer, C. Kristament, G. Ramer, M. Brandstetter, H. Goicoechea, B. Lendl, 'External-Cavity Quantum Cascade Laser Spectroscopy for Mid-IR Transmission Measurements of Proteins in Aqueous Solution', *Anal. Chem.*, **87**(13), 6980–6987 (2015). DOI: 10.1021/acs.analchem.5b01738

This article was published in the *Encyclopedia of Analytical Chemistry* in 2021 by John Wiley & Sons, Ltd.
DOI: 10.1002/9780470027318.a9751